UTFPR

UNIVERSIDADE TECNOLÓGICA FEDERAL DO PARANÁ

FEDERAL UNIVERSITY OF TECHNOLOGY - PARANÁ

POSTGRADUATE PROGRAM IN MECHANICAL AND MATERIALS ENGINEERING - PPGEM

RESEARCH CENTER FOR RHEOLOGY AND NON-NEWTONIAN FLUIDS - CERNN

VANESSA GLÜCK NARDI

A NUMERICAL STUDY OF PARTICLE SETTLING IN POWER-LAW FLUIDS USING LATTICE-BOLTZMANN METHOD

MSc Dissertation

CURITIBA

2018

VANESSA GLÜCK NARDI

A NUMERICAL STUDY OF PARTICLE SETTLING IN POWER-LAW FLUIDS USING LATTICE-BOLTZMANN METHOD

MSc Dissertation

MSc Dissertation presented to the Postgraduate Program in Mechanical and Materials Engineering - PPGEM from the Federal University of Technology - Paraná, as partial fulfillment of the requirements for the Master degree in Mechanical Engineering.

Advisor: Prof. Admilson T. Franco, Dr.
Co-Advisor: Prof. Cezar O. R. Negrão, PhD.

CURITIBA

2018

TERMO DE APROVAÇÃO DE DISSERTAÇÃO Nº 325

A Dissertação de Mestrado intitulada**:** A NUMERICAL STUDY OF PARTICLE SETTLING IN POWER-LAW FLUIDS USING LATTICE-BOLTZMANN METHOD, defendida em sessão pública pela Candidata **Vanessa Glück Nardi**, no dia 29 de junho de 2018, foi julgada para a obtenção do título de Mestre em Engenharia, área de concentração: Engenharia Térmica, e aprovada em sua forma final, pelo Programa de Pós-Graduação em Engenharia Mecânica e de Materiais – PPGEM.

BANCA EXAMINADORA:

Prof. Dr. Admilson Teixeira Franco - Presidente - UTFPR
Prof. Dr. Silvio Luiz de Mello Junqueira - UTFPR
Prof. Christian Naaktgeboren, Ph.D. - UTFPR - Guarapuava
Prof. Dr. Paulo Cesar Philippi - PUC-PR

A via original deste documento encontra-se arquivada na Secretaria do Programa, contendo a assinatura da Coordenação após a entrega da versão corrigida do trabalho.

Curitiba, _____de _____de 20___.

Carimbo e assinatura do Coordenador do Programa

_____

I dedicate this work to my little siblings Alexandre and Nicole. Growing up happened so fast but the memories of our childhood stays forever. I also dedicate it to our little angel, Gabriele Glück Nardi.

Acknowledgment

Abstract

NARDI, Vanessa Glück. **A numerical study of particle settling in Power–law fluids using lattice – Boltzmann method**. 2018. 108 pp. Dissertation – Postgraduate Program in Mechanical and Materials Engineering, Federal University of Technology – Paraná. Curitiba, 2018

Sedimentation of individual particles immersed in non-Newtonian fluid is of great industrial interest. Specifically in the oil and gas industry, cuttings generated from the drilling process must be constantly removed in order to properly clean the drill bit region. Thus, cuttings sedimentation must be avoided so that additional complications such as drill blocking and an unwanted operational stop are avoided. In this way, the drilling fluid must be carefully designed so that the it can fulfill these and others specifications. Therefore, it is of great importance to understand the dynamics of particles sedimentation in drilling muds. In this work, a numerical solution for particle settling in a non-Newtonian fluid is presented. The problem consists of a 2D particle released from rest in a quiescent non-Newtonian media within a fixed container. The fluid viscous behavior is represented by a Power-low expression. The aim of the present work was to develop a program able to adequately represent particle motion immersed in Power-law fluid. Based on the literature review, the problem was solved via a direct force immersed boundary- lattice Boltzmann method and its implementation was done via FORTRAN programming language. The Power-law effect was incorporated in the code by means of the adaptive viscosity method. Through verification problems, it was shown that the developed program was able to satisfactorily represent the particle settling dynamics in Newtonian and Power-Law fluids. A parametric study was then performed varying the particle diameter, d, Power-law index, n and particle/fluid density ratio, ρ_r. In general, regardless of the d and ρ_r combination, an increase of shear-thinning behavior leads to higher settling velocities. Results were then written in dimensionless form in such a way that results for the generalized particle Reynolds number, $Re_{pl,T}$, and the drag coefficient, $C_{D,T}$, experienced by the particle at its terminal velocity, are based only on the Power-law index and on the generalized Archimedes number Ar_{pl}.

Keywords: sedimentation, Power-law fluid, drag coefficient, Archimedes number, lattice-Boltzmann method.

Resumo

Sedimentação de partículas imersas em fluidos não newtonianos é de grande interesse industrial. Especificamente na indústria de petróleo, os cascalhos oriundos do processo de perfuração da rocha devem ser constantemente removidos de forma a limpar adequadamente a região da broca. Sendo assim, a sedimentação de cascalhos deve ser evitada de forma que complicações adicionais como o bloqueio da broca e uma parada operacional não programada sejam evitadas. Dessa forma, as propriedades reológicas do fluido de perfuração devem ser cuidadosamente arranjadas para que o fluido possa cumprir essas, dentre outras, funções. Portanto, é de grande importância entender a dinâmica da sedimentação de partículas em fluidos de perfuração. Neste trabalho, uma solução numérica para investigação da sedimentação de partículas em fluidos não newtonianos foi proposta. O problema consiste em uma partícula 2D liberada a partir do repouso em um fluido não-newtoniano representado por uma expressão de lei de potência. O objetivo do presente trabalho foi desenvolver um programa capaz de representar adequadamente o movimento de partículas imersas em um fluido Power-law. Com base na revisão da literatura, o problema foi resolvido através do método *lattice*-Boltzmann acoplado ao método da fronteira imersa e sua implementação foi feita via linguagem FORTRAN. O efeito Power-law foi incorporado ao programa através do método da viscosidade adaptativa. Por meio de problemas de verificação, foi comprovado que o programa desenvolvido foi capaz de representar satisfatoriamente a dinâmica de sedimentação de partículas em fluidos Newtonianos e em fluidos Power-Law. Um estudo paramétrico foi então realizado variando o diâmetro das partículas, d, o índice de lei de potência, n e razão de densidades partícula / fluido, ρ_r. Em geral, independentemente da combinação de d e ρ_r, um aumento do comportamento pseudoplásico leva a maiores velocidades de sedimentação. Os resultados foram então escritos na forma adimensional, de tal forma que o número de Reynolds generalizado, $Re_{pl,T}$ e o coeficiente de arrasto, $C_{D,T}$, experimentados pela partícula em sua velocidade terminal , pudessem ser escritos em função de n e do número de Arquimedes generalizado, Ar_{pl}.

Palavras-chave: sedimentação, Power-law, coeficiente de arrasto, número de Arquimedes, método *lattice*-Boltzmann.

List of Figures

List of Tables

Nomenclature

$\mathbf{a}$	Acceleration vector	$[m/s^2]$
A_p	Projected area	$[m^2]$
Ar	Archimedes number	$[-]$
Ar_{pl}	Generalized Archimedes number	$[-]$
C_D	Drag coefficient	$[-]$
$C_{D,T}$	Drag coefficient at terminal settling velocity	$[-]$
c_s	Speed of sound in lattice units	$[m/s]$
d	Diameter	$[m]$
D	Distance between the centers of the particle and the imaginary particle	$[m]$
$\mathbf{e}$	local particle velocity	$[m/s]$
f	Distribution function	$[-]$
$\mathbf{f}$	force density at Eulerian nodes	$[Pa]$
$\mathbf{F_B}$	Force acting on the boundary	$[N]$
F_D	Drag force	$[N]$
$F_{g,b}$	Gravitational force	$[N]$
$F_{p,b}$	Body force acting on a particle	$[N]$
$F_{p,c}$	Contact force acting on a particle	$[N]$
$F_{p,s}$	Surface force acting on a particle	$[N]$
F_B	Buoyant force	$[N]$
f_w	Wall correction factor	$[-]$
$\mathbf{g}$	Gravity	$[m/s^2]$
G	Elastic modulus	$[Pa]$
Ga	Galileo number	$[-]$
H	Height	$[m]$
I_s	Particle moment of inertia	$[kg.m^2]$
I_f	Moment of inertia of the displaced fluid	$[kg.m^2]$
L	Width	$[m]$
m	Consistency index	$[Pa.s]$
m^*	Particle–to–fluid mass ratio	$[-]$
Ma	Mach number	$[-]$
M_f	Mass of the displaced fluid	$[kg]$
m_p, M_s	Particle mass	$[kg]$
n	Power-law index	$[-]$
n_k	Set of Boolean variables	$[-]$

NL	Number of Lagrangian nodes	[–]
p	Pressure	$[Pa]$
$R = L/d$	Aspect ratio between particle and container width	[–]
r	Radius	$[m]$
Re	Reynolds number	[–]
Re_{pl}	Generalized Reynolds number	[–]
$Re_{pl,T}$	Generalized Reynolds number at terminal settling velocity	[–]
S	Particle surface	$[m^2]$
t	Time	$[s]$
$\mathbf{u}$	velocit vector	$[m/s^2]$
$\mathbf{U_B}$	Boundary velocity vector	$[m/s]$
$\mathbf{U_c}$	Particle center velocity vector	$[m/s]$
v	Relative velocity	$[m/s]$
V_p ,V_s	Particle volume	$[m^3]$
V_T	Particle vertical terminal velocity	$[m/s]$
$\mathbf{v_p}$	Particle translational velocity	$[m/s]$
W	Weight	$[N]$
w_k	Weighting factors	[–]
x	The horizontal coordinate	$[m]$
$\mathbf{X_c}$	Particle center position vector	$[m]$
$\mathbf{x_p}$	Particle position vector	$[m]$
$\mathbf{x_w}$	Position vector of an imaginary particle	$[m]$
y	The vertical coordinate	$[m]$
Y	Power–law correction factor for Drag coefficient	[–]

Greek letters

δ	Kronecker delta	[–]
δ_t	Time step	$[s]$
Δ	Increment	[–]
η	Apparent viscosity	$[Pa.s]$
λ	Mean relaxation time	$[s]$
μ	Dynamic viscosity	$[Pa.s]$
$\dot{\boldsymbol{\gamma}}$	Shear rate tensor	$[s^{-1}]$
$\boldsymbol{\gamma}$	Strain tensor	[–]
$\boldsymbol{\tau}$	Shear stress tensor	$[Pa]$
Ω	collision operator	[–]
$\boldsymbol{\omega_c}$	Angular velocity of the particle	$[rad/s]$

ρ	Density	$[kg/m^3]$
$\boldsymbol{\sigma}$	Momentum fkux tensor	$[Pa]$
τ	Dimensionless mean relaxation time	$[-]$

Subscripts and superscripts

$(\ )_s$	Solid
$(\ )_f$	Fluid
$(\ )_x$	In the x direction
$(\ )_y$	In the y direction
$(\ )^{EQ}$	Equilibrium
$(\ )^{neq}$	Non equilibrium
$(\ )_\infty$	Reference value
$(\ )_l$	Lattice unit

Abbreviations

2D	Two–dimensional
3D	Three–dimensional
CFD	Computational Fluid Dynamics
LBM	Lattice–Boltzmann Method
IBM	Immersed Boundary Method
IB–LBM	Immersed Boundary – Lattice–Boltzmann Method
SRT	Single relaxation time
LBE	Lattice–Boltzmann Equation

Contents

1 Introduction

1.1 Context

The transport of solids by fluids is a relevant process in several areas, such as in the pharmaceutical industry, food processing, mining and oil exploration (GOYAL; DERKSEN, 2012). In general, solid−liquid suspensions are a heterogeneous mixture of solid particles in a liquid. When the particles are heavier than the liquid, they tend to settle and accumulate at the bottom of the vessel or pipe and these are called settling suspensions (SILVA et al., 2015).

Specifically in the oil industry, when a wellbore is drilled in order to reach an oil reservoir, fragments are produced while the drill bit cuts the rock, forming a heterogeneous mixture of drilling fluid and cuttings, as shown in Fig.1.1 detail. These cuttings must be constantly removed from the drill bit region by the drilling fluid in order to clean the wellbore properly, thus avoiding further complications, such as blocking the drill bit (NGUYEN, 1996).

1.2 Drilling Process

The rotary drilling method has been effectively used since the beginning of the 20th century in the oil and gas industry (NGUYEN, 1996). In this drilling technique, a downward vertical force is applied to the drill bit as it rotates around its own axis. This combined movement crushes the rock formation and the cuttings are carried by the drilling fluid, which is continuously circulated through a hollow pipe. When the drilling fluid returns to the surface, the cuttings are removed and the fluid is pumped back. The most significant operations involved in the drilling fluid circulation process are shown in Fig. 1.1 and discussed hereafter.

There are two different ways to circulate the drilling mud, the direct and reverse circulation. In the direct circulation, the mud flows down−hole through the drill pipe (1). When the fluid reaches the bottom of the hole, it passes over the drill bit (2) and then returns by the annular region (3) carrying cuttings up to surface, as shown in Fig. 1.1. In the reverse circulation, the mud flows down through the annular region and then up through the drill pipe. Either way, the mud on the surface is directed to a mud return line (4) and before re−entering the wellbore the drilled cuttings are removed from the drilling mud by filtration (5). The mud flow is therefore a continuous circulating system and to keep proper functioning of the entire system, the drilling mud has to comply operational features and must fulfill some very important functions, such as (NGUYEN, 1996):

a) Cooling the drill bit and lessening drill pipe friction;

b) Consolidating the wall of the wellbore;

c) Preventing inflows of formation fluids into the wellbore;

d) Providing geological information;

e) Transporting cuttings to the surface;

f) Suspending cuttings when drilling has stopped.
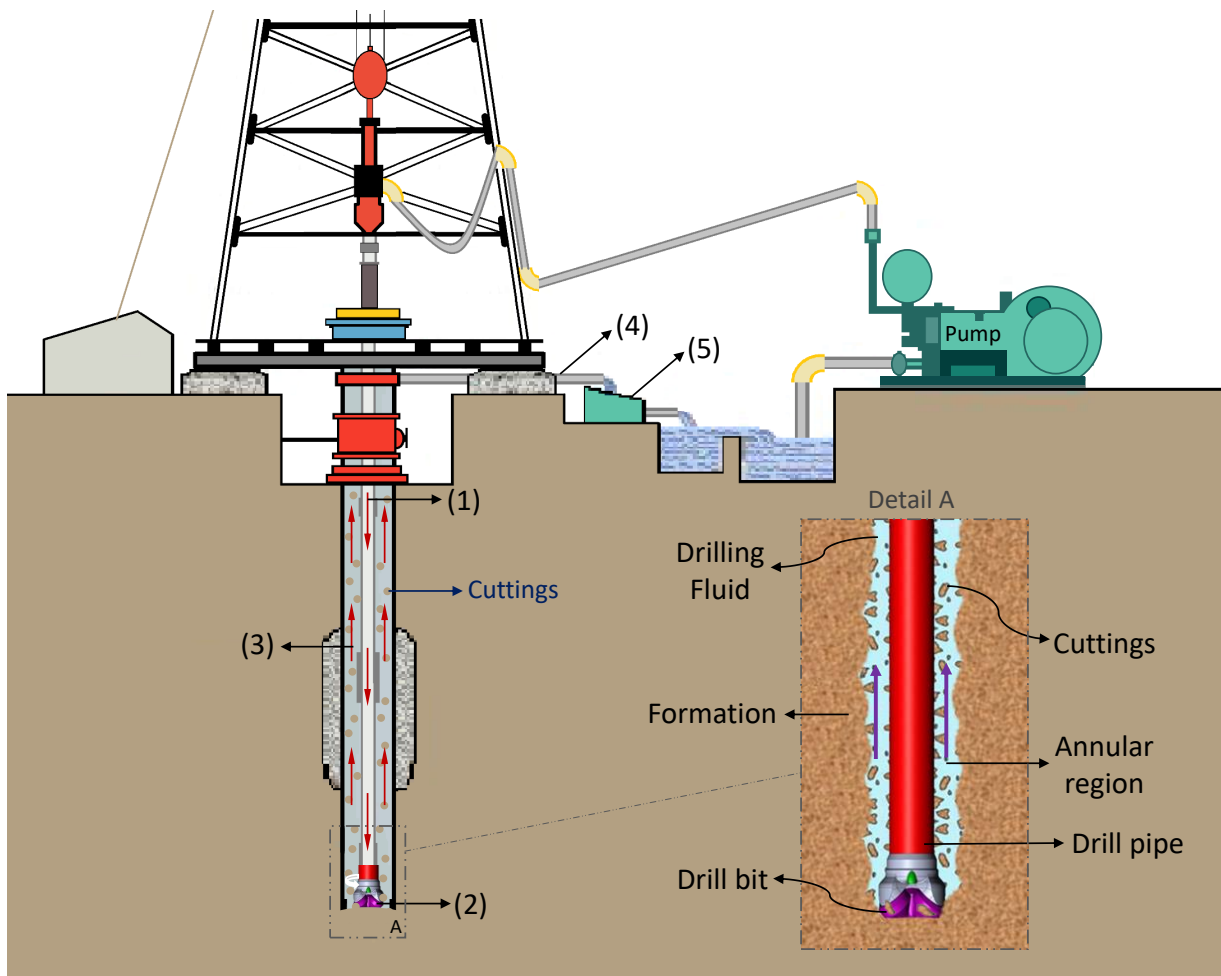
Figure 1.1 – Illustration of the drilling process. The drilling fluid is added to the wellbore by the pump trough the drill pipe (1), it passes over the drill bit (2) and returns through the annular region (3) carrying cuttings. Then, the drilling fluid is redirect to a return line (4) and the cuttings are filtered off (5) and the drilling fluid is pumped back to the wellbore. In detail is shown a heterogeneous mixture of drilling fluid and cuttings resulting from the drilling process.

The drilling fluid is usually a mixture of water, clay and weighting materials and due to its importance in the drilling process, its rheological properties must be carefully arranged to meet all the requirements listed above. Therefore, the drilling fluid is a complex material that presents thixo−elasto−viscoplastic behavior, that is, it presents elastic, viscoplastic and time dependent properties (thixotropy). Furthermore, in the range of shear rate of interest, drilling fluids are also known for exhibit shear−thinning behavior, which is represented adequately by

a Power−law model. These are fluids that present strain−dependent viscosity with decrease viscosity with increasing strain rate.

1.3   Statement of the problem

One of the most important functions of a drilling fluid is to carry cuttings out of the drill bit region as quickly as possible. Generally, due the greater density of the cuttings when compared with the drilling fluid, cuttings tend to settle and travel with a lower velocity than the drilling fluid itself. For efficient hole cleaning, much effort has been done to improve the drilling fluid ability to transport cuttings from the bottom to the surface of the wellbore. It is therefore important to be able to predict accurately the settling and transport of particles moving through a drilling fluid.

Thus, the knowledge of settling cuttings dynamics in drilling fluids is of great importance. For this reason, the fundamental problem addressed in this work is the settling of a particle immersed in a non−Newtonian fluid. Fig. 1.2 shows a schematic description of the problem. When the drilling fluid is not circulating the cuttings begin to settle. On the left side of Fig. 1.2 it is shown the cuttings, represented by circular particles, carried by fluid during drilling fluid circulation. The right side of Fig. 1.2 shows cuttings sedimentation due to gravitational force during an operational stop, which is the stop of drilling fluid circulation for operational reasons, such as wellbore cementation.

Given the complex interaction between drilling fluid and cuttings, simplifications were made so that the present study could be conducted. The main simplifications are:

a) The problem is considered to be two−dimensional;

b) The cuttings are considered to be 2D homogeneous particles of constant diameter;

c) Only sedimentation of a single particle is considered. Thus, interaction between particles such as collision and particle aggregation are not availed in the present work;

d) The drilling fluid is considered to present shear−thinning rheological behavior, which is represented by a Power−law expression;

e) The particle interaction with the drill pipe and the formation are not considered;

f) The particle is released from rest in a quiescent fluid.

The simplified problem is shown in Fig. 1.3. The particle settling problem was approached by numerical techniques conducted by Computational Fluid Dynamics (CFD) based on Lattice−Boltzmann Method (LBM) coupled with Immersed Boundary Method (IBM).
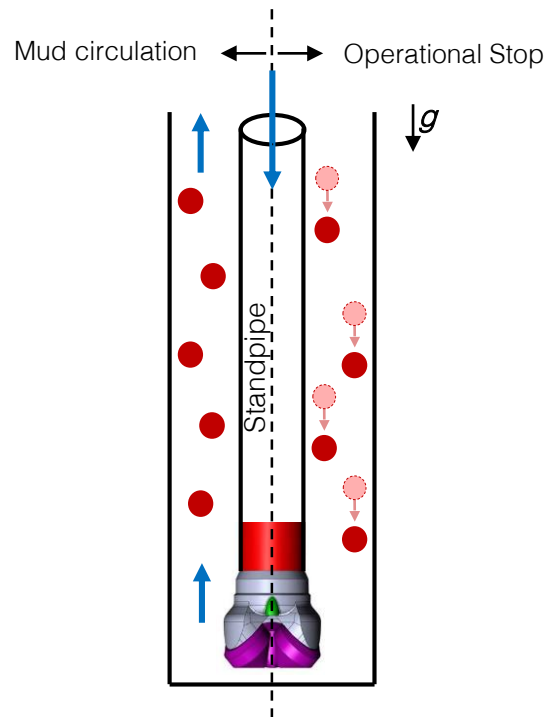
Figure 1.2 – A schematic description of the phenomenon. Cuttings settling under gravity, g, during an operational stop is shown at the left side, while the right side shows cuttings transportation from the drill bit region the the surface.
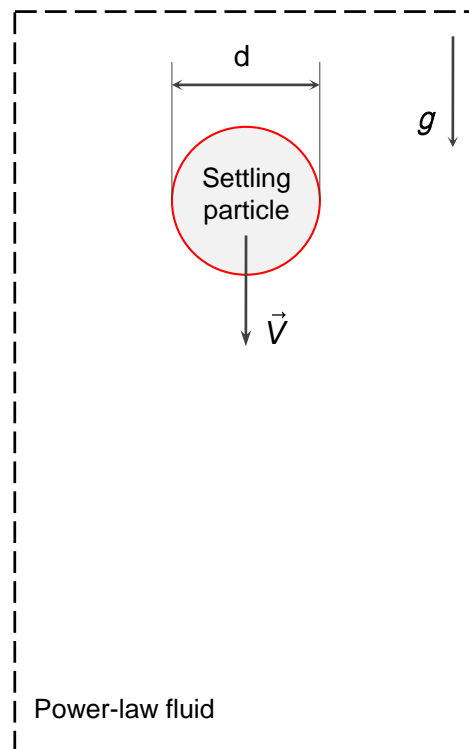
Figure 1.3 – Simplified scheme for a 2D rigid particle of diameter d, release from rest in a quiescent Power$-$law fluid with settling velocity $\vec{V}$ due gravity effect g.

1.4   Objectives

The objective of this study is to develop a program that implements a Lattice−Boltzmann method (LBM) that is capable of solving 2D problems of particle settling in Power−law fluid. This is done to improve understanding of the settling behaviour of particles in Power−law fluids and to determine the effects of fluid rheological properties on the motion of the settling particle, which is quantified by the particle terminal settling velocity and the drag coefficient experienced by the particle at its terminal velocity.

In order to achieve the main objective of this work, algorithms for applicable 2D non−Newtonian flow problems with stationary and moving boundary were developed as verification cases. The numerical code was written in FORTRAN 90 and the main points of the development were:

a) Application of LBM to solve Power−Law fluid flow. To do so, Power−law fluid flow between parallel plates were considered;

b) The coupling of Immersed Boundary Method and LBM (IB−LBM) to solve complex stationary boundary problems covering solid−fluid flows. For this, a two−dimensional Newtonian fluid flow past over a cylinder has been considered;

c) Application of IB−LBM to solve moving boundary. Here, the settling of a particle in Newtonian fluid was fulfilled;

d) Extension of IB−LBM to solve moving boundary problems with Power−law fluids. In this final topic, the settling of a particle in Power−law fluid was accomplished.

The mathematical formulation and the numerical procedure using IB−LBM are detailed in the further chapters.

1.5   Outline

This work is divided into 8 parts. In Chapter 1 the aim and objectives of this research project were presented. The framework that have been set for the achievement of these objectives is introduced.

Chapter 2 presents a theoretical background necessary for the development of this project. Basic concepts covering the issues involved in the settling of particles and basic rheology are presented and an introduction to non−Newtonian fluids is given.

A comprehensive literature review is presented in Chapter 3. The issues associated with non−newtonian fluids are discussed and an evaluation of relevant results published in the literature covering the settling behavior of particles in different fluids is presented.

Chapter 4 presents detailed characteristics of the problem formulation and the mathematical formulation applied to the problem is described. The numerical procedure is discussed in

Chapter 5, where the main concepts of the LBM are presented and the immersed boundary method is described, as well as the approach used for treat Power−law fluids in LBM.

Validations of the developed program are presented in Chapter 6, where results for lid−driven cavity, Power−law flow between parallel plates, flow past over a circular cylinder and particle settling are compared with reference literature data.

A parametric study for particle settling in Power−law fluid is conducted in Chapter 7. Results for different configurations of particle and fluid properties are discussed.

Conclusions and suggestions for future work are presented in Chapter 8.

2 Theoretical background

This chapter provides the essential theoretical information that is recurrently used in the following chapters. It includes the essential features of non-Newtonian fluid mechanics and the motion of a single particle in a fluid.

2.1 Rheology of non−Newtonian fluids

The study of rheology concerns the flow and deformation of matter while subjected to shear stress forces (MORRISON, 2001). For Newtonian fluids the relationship between stress and deformation is given by Newton's law of viscosity, expressed by:

$$\boldsymbol{\tau} = \mu\dot{\boldsymbol{\gamma}}$$

(2.1)

where $\boldsymbol{\tau}$ is the shear stress tensor, $\dot{\boldsymbol{\gamma}}$ the shear strain rate tensor and μ is the Newtonian viscosity which is a constant of proportionality between the shear stress and the shear strain rate.

For ideal solid elastic materials, the shear stress is proportional to the imposed strain as stated by the Hooke's law (MORRISON, 2001), given by:

$$\boldsymbol{\tau} = G\boldsymbol{\gamma}$$

(2.2)

where $\boldsymbol{\gamma}$ is the strain tensor and G is the elastic modulus.

Different materials present distinctive deformation behavior depending on its internal structure composition. The relationships between the stress and deformation for most part of the materials differs from Newton's law of viscosity and also do not follow Hooke's law of elasticity (MORRISON, 2001). Those are called non−Newtonian materials.

Depending on the material and the circumstances, different types of non-Newtonian characteristics may stand out as a response to the stress applied on the material (DESHPANDE et al., 2010). Each type of non−Newtonian behavior will be discussed below.

According to Deshpande et al. (2010), such materials are conveniently grouped into three categories:

1. *Systems for which the value of the shear strain rate, $\dot{\gamma}$, at a point within the fluid is determined only by the current value of the shear stress, τ, at that point, or vice versa, these substances are variously known as purely viscous, inelastic, time−independent or generalized Newtonian fluids (GNF);*

2. *Systems for which the relation between τ and $\dot{\gamma}$ shows further dependence on the duration of shearing and kinematic history; these are called time$-$dependent fluids;*

3. *Systems that exhibit a blend of viscous fluid$-$like behavior and of elastic solid$-$like behavior. For instance, this class of materials shows partial elastic recovery, recoil, creep, etc. Accordingly, these are called viscoelastic or elastic$-$viscous fluids.*

2.1.1   Generalized Newtonian fluids (GNF)

As described above, non$-$Newtonian time$-$independent fluids are those in which the shear stress is adequately described as a function only of the shear strain rate. These fluids are defined as those that cannot be described by Newtonian behavior, or by a single constant viscosity. Thus, rather than using the term viscosity, rheologists prefer to use the term apparent viscosity, denoted by η.

The relationship between stress and shear strain rate is analogous to that of Newtonian fluids, expressed in terms of an apparent viscosity:

$$\boldsymbol{\tau} = \eta(\dot{\gamma})\dot{\boldsymbol{\gamma}} \tag{2.3}$$

where $\dot{\gamma}$ is the magnitude of the shear strain rate tensor, given by:

$$\dot{\gamma} = \sqrt{\frac{1}{2}\sum_i \sum_j \dot{\gamma}_{ij}\dot{\gamma}_{ji}} \tag{2.4}$$

Depending on how viscosity changes with shear strain rate the flow behavior may be characterized in different types. The most common behavior of non$-$Newtonian time$-$independent fluids is shear$-$thinning, or pseudoplasticity, where the apparent viscosity decreases with increasing shear strain rate. The opposite effect, where the apparent viscosity increases with increasing shear strain rate is termed shear$-$thickening and is less frequently encountered (MORRISON, 2001). There are a few models available in the literature describing both phenomena. Probably, as shown in the literature review in Chapter 3, the most widely used model, and also the one used in this work, is the Power$-$law model, in which the apparent viscosity is given by:

$$\eta(\dot{\gamma}) = m\dot{\gamma}^{n-1} \quad \text{where if} \begin{cases} n > 1 \Rightarrow \text{Shear}-\text{thickening} \\ n = 1 \Rightarrow \text{Newtonian} \\ n < 1 \Rightarrow \text{Shear}-\text{thinning} \end{cases} \tag{2.5}$$

where m is the consistency index and n is the Power$-$law index, which are constants that must be fit to experimental data. Other common rheological models that describe pseudoplasticity, such as the Carreau and the Yasuda models, are listed in Tab. 2.1.

Table 2.1 – Other rheological equations for pseudoplastic fluids.

Authors	Equation	Notes
Carreau (1972) Pseudoplastic	$\eta = \eta_0 \left[1 + (k\dot{\gamma})^2 \right]^{|m-1|/2}$	η_0 = limiting zero$-$shear viscosity k, m = constants
Yasuda et.al (1981) Pseudoplastic	$\dfrac{\eta - \eta_\infty}{\eta_0 - \eta_\infty} = \dfrac{1}{1 + (k\dot{\gamma}^m)^{\frac{n-1}{m}}}$	η_∞ = limiting high$-$shear viscosity k, m, n = constants

Figure 2.1 schematically shows flow curves for Newtonian, shear–thinning and shear–thickening fluids. It is important to note, as mentioned by Fernandes (2016), that this classification of non–Newtonian time–independent fluids is an idealization of the behavior of these materials. It should be noted that most polymeric materials and solutions possess a combination of different types of rheological behaviors. As a result, they are generally classified as rheological–complex fluids. Indeed, according to Ewoldt and McKinley (2017) both Bingham and Maxwell emphasized the need for careful consideration of the relevant time scales and forces scales for distinguishing between the different rheological responses of many real−world materials. Thus, such materials are therefore best described, in the most general cases, as thixotropic elasto−visco−plastic materials (EWOLDT; MCKINLEY, 2017).
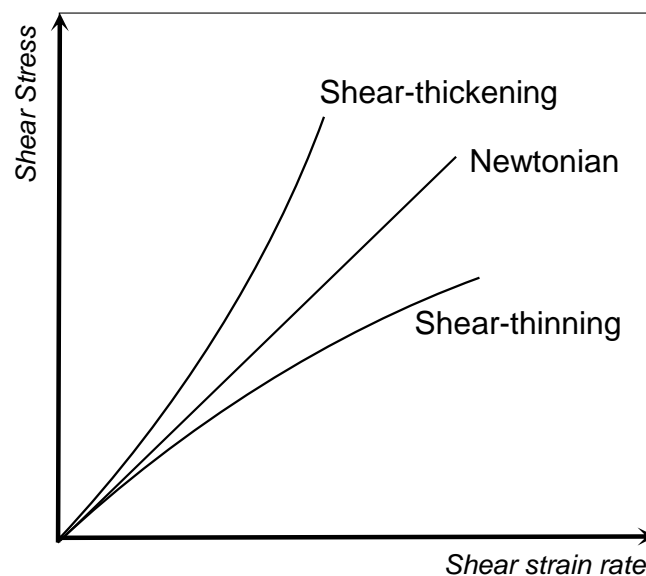
Figure 2.1 – Viscous behavior of Newtonian, shear−thinning and shear−thickening materials (adapted from Deshpande et al. (2010)).

2.2   Motion of a single particle in a fluid

When a particle is released in an infinite quiescent fluid, it is subjected to gravitational, buoyant and drag forces. If the particle is denser than the fluid, the gravitational force is initially dominant and accelerates the particle downwards. As the particle velocity increases, drag force rises and the particle acceleration decreases until it moves at a constant velocity, known as terminal velocity (CHHABRA, 2006).

The forces acting on a spherical particle immersed in an infinite medium are shown in Fig. 2.2. F_D is the drag force, F_B the buoyant force, W the particle weight and d is the particle diameter.
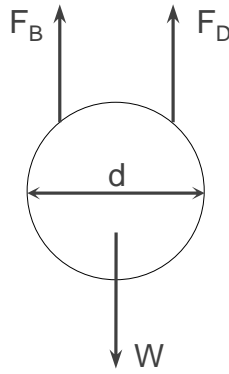
Figure 2.2 – Buoyant force, F_B, drag force, F_D, and particle weight, W, acting on a particle of diamenter d in a fluid.

In particle sedimentation problems the variable of interest is the terminal velocity of the particle, V_T. The terminal velocity is reached when the particle weight balances the buoyant and drag forces acting on the particle. The challenge in this problem is to determine the drag force to which the particle is subjected.

Stokes proposed the solution to this problem in 1851. The Stokes law is a fundamental equation derived from a simplification of the Navier$-$Stokes equations (given by Eqs. 2.6 and 2.7) that states a balance between the local viscous and pressure forces (STOKES, 1851).

$$\nabla \cdot \mathbf{u} = 0 \tag{2.6}$$

$$\rho_f \frac{D\mathbf{u}}{Dt} = -\nabla p + \mu \nabla^2 \mathbf{u} + \rho_f \mathbf{g} \tag{2.7}$$

where ρ_f is the density of the fluid, $\boldsymbol{\tau}$ is the stress tensor, $\mathbf{u}$ is the velocity vector, $\mathbf{g}$ is the gravity vector and p is the pressure.

To solve the problem, Stokes neglected the inertial forces. This condition is only possible at very low Reynolds numbers (defined in Eq. 2.11) ($Re << 1$), a typical condition where the

fluid viscosity is very high and/or the particle settling velocity is very low. Solving the velocity and pressure fields under these conditions, Stokes found that the drag force, which is the summation of the drag experienced by the particle caused by pressure and viscous effects, is given by (CHHABRA, 2006):

$$F_D = 6\pi\mu r v \tag{2.8}$$

where μ is the dynamic viscosity, r is the radius of the spherical particle and v is the flow velocity relative to the particle.

The dimensionless form of the drag force is known as the drag coefficient C_D, given by:

$$C_D = \frac{2F_D}{A_p \left(\rho_f v^2\right)} \tag{2.9}$$

where A_p is the projected area. The projected area in the case of the settling of a spherical particle is the sphere cross section, $A_p = \pi R^2$. ρ_f is the fluid density and v is the particle velocity.

Thus, if the inertial effects are negligible in comparison to the viscous effects, the drag coefficient becomes:

$$C_D = \frac{24}{Re} \tag{2.10}$$

where Re is the Reynolds number:

$$Re = \frac{\rho_f v d}{\mu} \tag{2.11}$$

where d is the sphere diameter.

The Stokes law was solved by making some assumptions and neglecting some terms, then integrating viscous and pressure forces over the entire surface of a sphere. So, the Stokes law is an equation of creeping motion for low Reynolds number flows past a sphere. Although the Stokes law is highly limited, it has been the basis of many numerical analyses in the prediction of the settling behavior of spheres, as shown in the literature review presented in Chapter 3. However, for most applicable situations, inertial effects can not be neglected and for this reason F_D can not be simplified as it is in Eq. 2.8. The literature review reveals that until the present days, experimental and numerical simulations are performed to help with the development of new correlations for the drag coefficient, mostly, as a function of the particle Reynolds number.

2.3   Introduction to the Numerical approach

In computational fluid dynamics (CFD) is very important to develop effective treatments of boundary conditions in complex boundaries, whether these are or not moving. During the past years several researchers have developed numerical methods to accurately treat this type of boundary condition. This section gives an introduction to one of such methods named the immersed boundary method, which is used in the present work.

Further, a quick explanation about the lattice−Boltzmann method and an introduction of its coupling to the immersed boundary method are given. The detailed numerical approach used in this work is given in Chapter 5.

2.3.1   Immersed Boundary Method (IBM)

The IBM was first proposed by Peskin (1977) and consists of a non−body−conformal grid method where the flow field is discretized in a fixed Cartesian/Eulerian mesh whereas the boundaries are represented by a set of Lagrangian points as shown in Fig. 2.3. There are different ways to impose the boundary condition on IBM. In general the flow governing equations such as Navier−Stokes equation or Lattice Boltzmann equation, are modified by adding a boundary force density term to satsisfy the no−slip boundary condition.
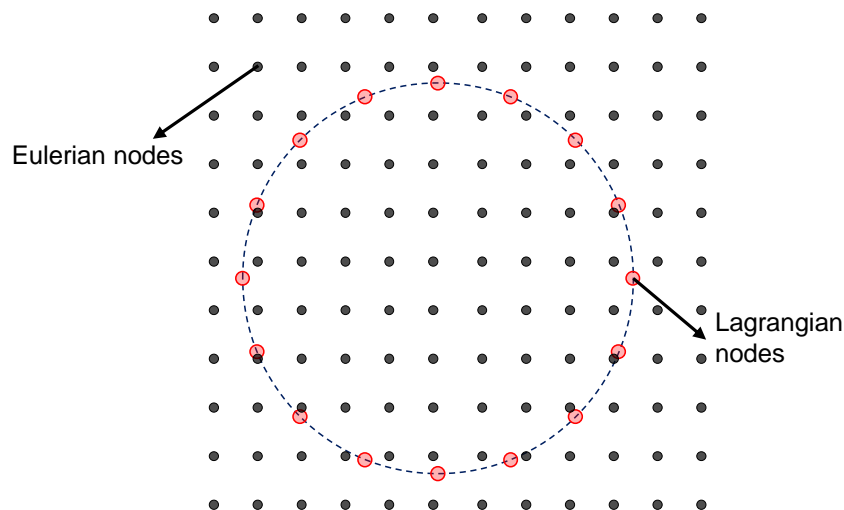
Figure 2.3 – Eulerian and Lagrangian nodes in IBM.

Since the pioneering work of Peskin (1977), numerous modifications have been proposed to the method and now a number of variants of this approach exists which make it hard to find an unified definition of the method. In the preset work the classification approach by Kang (2010) is used. According to Kang (2010) there are two main ways to evaluate the boundary force density term, namely feedback−forcing method and direct−forcing method. Peskin (1977) used a feedback−forcing IBM for simulating of blood flow in an elastic heart valve. In this forcing method the boundary force density is computed by Hooke's law, where

the force is a function of the surface boundary deformation with the spring constant (DASH, 2014). In the direct−forcing method the forcing term is determined from the error between the calculated velocity and the desired IB velocity (KANG, 2010).

Further, as reported by Kang (2010), IBMs require interface schemes since the Lagrangian points, in general, do not necessarily match the Eulerian nodes. There are some options that can be used to treat the interface and they are grouped in two different categories: diffuse and sharp interface schemes. In the sharp scheme the governing equations are solved only for the nodes in the fluid domain. For moving immersed boundaries, this leads to the generation of fresh nodes (nodes that switch from solid to fluid domain) and dead nodes (nodes that switch from fluid to solid domain) (SEO; MITTAL, 2011). The velocity on the forcing node is determined by interpolation so that the corresponding boundary node (in the Lagrangian mesh) may satisfy the no−slip condition.

In the diffuse interface scheme, the boundary force (that is calculated in the Lagrangian nodes) is distributed into neighboring Eulerian nodes since the forcing points are not on the Eulerian mesh. To do so, discrete Dirac's delta functions are used for the force distributions, which makes the boundary diffuse.

In this work an implicit direct forcing method with diffuse interface scheme is applied and the detailed explanation and mathematical modeling of the method are given in Chapter 5.

2.3.2   Lattice Boltzmann Method (LBM)

LBM is a discrete computational method based on the kinetic Boltzmann equation (GUO; SHU, 2013). It considers a typical volume element of fluid to be composed of a collection of particles that are represented by a particle velocity distribution function for each fluid component at each lattice point. In this way, LBM solves the evolution of particle density distribution function with streaming and collision processes where time is counted in discrete time steps. Thus, it can be said that LBM describes the dynamics of a fluid on a mesoscopic scale, since it does not describe the behavior of each particle individually as it is done in microscale simulations, such as in molecular dynamics methods. To better show where LBM is, consider Fig. 2.4 which shows the hierarchy of scales associated with typical fluid problems.

At first there is the scale of a fluid atom in a microscopic system governed by Newton's equations of motion. Then there is the mesoscopic scale in which individual molecules or atoms are not tracked but collections of fluid molecules are described by a kinetic theory on which LBM is based. Finally, there is the macroscale which is a continuum medium where fluids can be described by conservations laws of mass, momentum and energy (KRÜGER et al., 2017). In LBM, the macroscopic fluid variables are derived from integration of the distribution function at the lattice nodes.

Microscale simulations
Molecular Dynamics

Mesoscale simulations
Lattice Boltzmann Method

Macroscale simulations
Conventional CFD

Atom or molecule

Particle distribution
function

Discretized
continuous medium
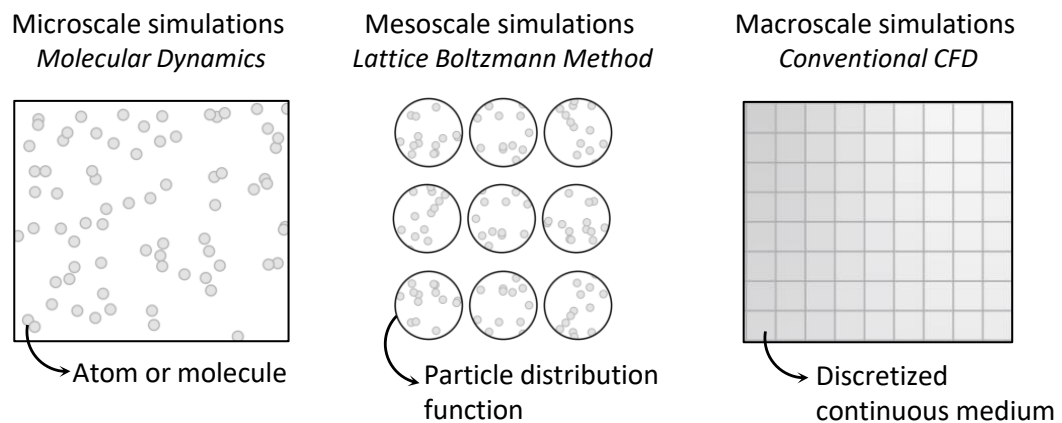
Figure 2.4 – Hierarchy of scales associated with typical fluid problems.

Although LBM has proved to be a powerful tool for solving problems in fluid dynamics, its spatial discretization is limited to regular lattices, thus representing complex boundaries in LBM requires special treatment.

2.3.3   Immersed Boundary − Lattice Boltzmann Method (IB−LBM)

The common feature of using the Cartesian grids motivates the coupling of LBM and IBM, which is called immersed boundary − lattice−Boltzmann method (IB−LBM). The first coupled IB−LBM was proposed by Feng and Michaelides (2004) to simulate the motion of rigid particles. Their approach is similar to the feedback forcing method of Peskin (1977) but instead of solving the Navier−Stokes equations they used the lattice−Boltzmann equation. In the same way that it happened after the work published by Peskin (1977), many studies involving IB−LBM arose just after Feng and Michaelides' work. The exploration of this new branch in the LBM has brought out several new different ways of approaching the particle−fluid coupling by the immersed boundary method in the LBM framework. Some detail of the different approaches of IB−LBM available are given in Chapter 3

The present work focus in the IB−LBM with an implicit direct forcing method with diffuse interface, following the work of Kang (2010), Dash (2014) and Delouei et. al. (2016).

3 Literature Review

Because particle motion and particle collisions play an important role in the performance of many industrial processes involving suspension flows, several studies regarding the settling mechanisms of particles have been performed in the last decades. Over the years, analytical solutions, empirical and numerical correlations for particles terminal velocity and drag force have been developed.

Therefore, this section is dedicated to provide information, on discrete settling of particles in various types of fluid, with emphasis on the effects that may contribute to the numerical procedures involved in the present study.

3.1   Settling particles in Newtonian fluids

Particle motion in incompressible Newtonian fluids is not only the simplest case of the complex phenomena of discrete sedimentation, but also lays out the foundation for non-Newtonian fluids.

Several researchers have been working on the study of the drag coefficient, which is usually expressed as a function of the Reynolds number, Re. The relationship between C_D and Re is complex and has only been theoretically evaluated in the Stokes region ($Re << 1$), as mentioned in Chapter 2. The manner in which C_D varies with Re from laminar or transitional to the turbulent flow region has been studied by several authors along the years. Clift, Grace and Weber (2005) $apud$ Chhabra (2006) presented a review and their recommendations for calculating the drag coefficient for a given Reynolds number as shown in Tab. 3.1. As can be seen in Tab. 3.1, different drag coefficient correlation may be more suitable to predict the particle drag coefficient depending on the particle Re.

Depending on the particle and fluid properties the particle settling dynamics may undergo different regimes. There are regime maps available in the literature that describe the settling or rising of particles immersed in a fluid. In Doychev (2015) an extensive review of particle settling dynamics in Newtonian fluid is presented, where three main different regimes are generally observed: a steady axi-symmetric settling, an oblique path settling and a chaotic settling. The settling or rising regime changes from axi-symmetric to chaotic as the settling velocity increases. A map of regimes that relates the particle-to-fluid mass ratio (m^*), in which $m^* > 1$ represents a settling particle while $m^* < 1$ a rising particle, and the particle Reynolds number is proposed by Horowitz and Williamson (2010) and is presented in Fig. 3.1. As can be seen, regarding of Re the particle may settle vertically when $Re < 210$ and then it tends to settle following a oblique pattern for $210 < Re < 600$. The settling pattern

Table 3.1 – Recommended drag coefficient correlations; Standard Drag Curve, $w = \log Re$

Range of Re	Drag coefficient correlation
$Re < 0.01$	$C_D = \dfrac{24}{Re}\left(1 + \dfrac{3}{16}Re\right)$
$0.01 < Re \leq 20$	$C_D = \dfrac{24}{Re}\left(1 + 0.1315Re^{(0.82-0.05w)}\right)$
$20 \leq Re \leq 260$	$C_D = \dfrac{24}{Re}\left(1 + 0.1935Re^{(-0.6305)}\right)$
$260 \leq Re \leq 1500$	$\log C_D = 1.6435 - 1.1242w + 0.1558w^2$
$1.5 \times 10^3 \leq Re \leq 1.2 \times 10^4$	$\log C_D = -2.4571 + 2.558w - 0.9295w^2 + 0.1049w^3$
$1.2 \times 10^4 < Re < 4.4 \times 10^4$	$\log C_D = -1.9181 + 0.637w - 0.063w^2$
$4.4 \times 10^4 < Re \leq 3.38 \times 10^5$	$\log C_D = -4.339 + 1.5809w - 0.1546w^2$
$3.38 \times 10^5 < Re \leq 4 \times 10^5$	$C_D = 29.78 - 5.3w$
$4 \times 10^5 < Re \leq 10^6$	$C_D = 0.1w - 0.49$
$4 \times 10^6 < Re$	$C_D = 0.19 - \left(\dfrac{8 \times 10^4}{Re}\right)$

becomes intermittent for $600 < Re < 1550$ and for $Re > 1550$ the particle tends to settle vertically but the wake fallows a zigzag pattern.

A different diagram for the regime of settling or rising spherical particle was proposed by Braza, Chassaing and Minh (1986) and is shown in Fig. 3.2. The difference is that this map relates the particle settling regime for a given particle-to-fluid density ratio (ρ_0/ρ) and Galileo number (Ga) combination. Ga is the non-dimensional number characterized by the ratio of buoyant and viscous effects, given by Eq. 3.1 and is more commonly used for bubbly flows.

$$Ga = \frac{\sqrt{|\rho_0/\rho - 1|\, g d^3}}{\nu} \tag{3.1}$$
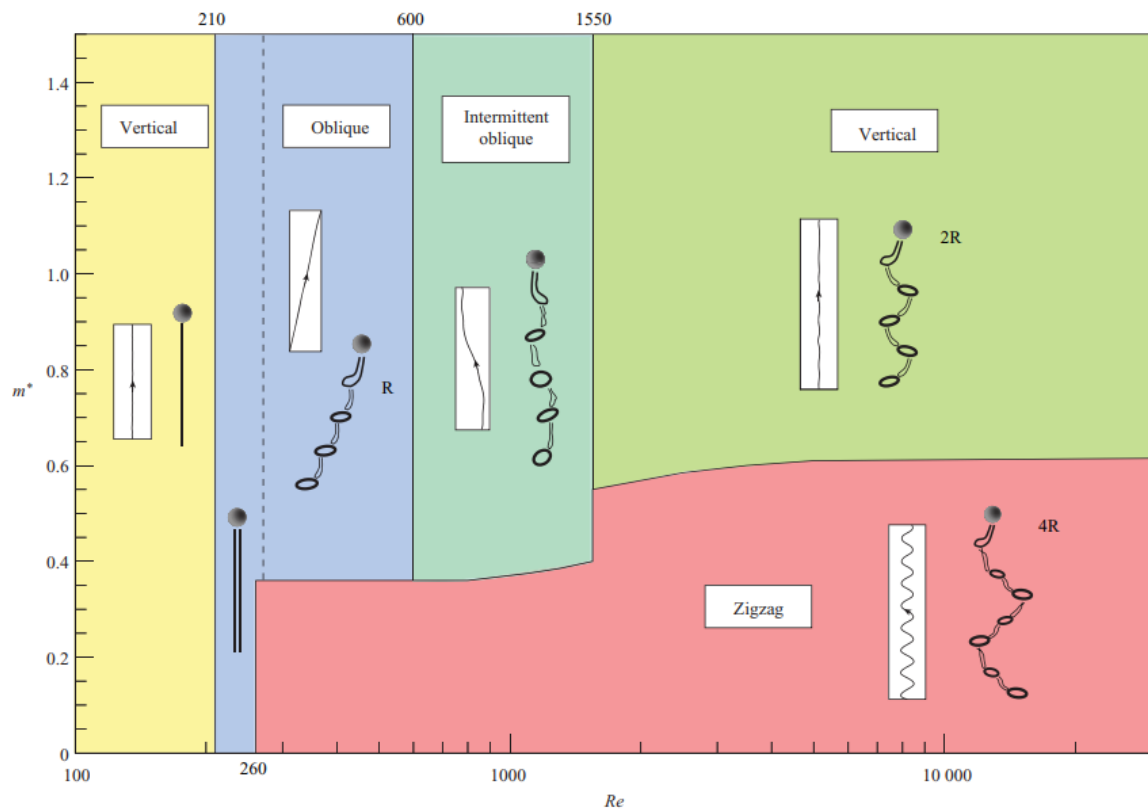
Figure 3.1 – Map of regimes reprinted from Horowitz and Williamson (2010). The diagram depicts the motion of the sphere and its associated wake patterns regarding of the mass ratio (defined as the relative density of the particles compared to the fluid) and the particle Reynolds number (m^*,Re).

3.2 Settling suspensions in non-Newtonian fluids

Despite of solid particles settling in a Newtonian liquid under the influence of gravity have been widely studied, the industrial practice also requires research of solid particles in fluids with more complex rheological behavior. The particle terminal velocity and consequently the drag force, depend on a large set of variables. This includes not only the size, the shape and the density of particles, but also the particle-particle interaction and wall effects. Additionally, the terminal velocity is also strictly related to the fluid rheological behavior (CHHABRA, 2006).

3.2.1 Non-yield stress fluids

In non-Newtonian fluids, the viscosity varies as a function of the shear strain rate. When a particle falls in a quiescent fluid, it will generate a local shear field and the viscosity will vary around the sphere (REYNOLDS; JONES, 1989). Similarly to the case with Newtonian fluids, the theoretical analysis in the creeping flow regime involves the solution of the momentum equation, neglecting the inertial terms. However, according to Chhabra (2006), the extension of the Stokes solution to shear-thinning fluids is nontrivial and various types of approximations
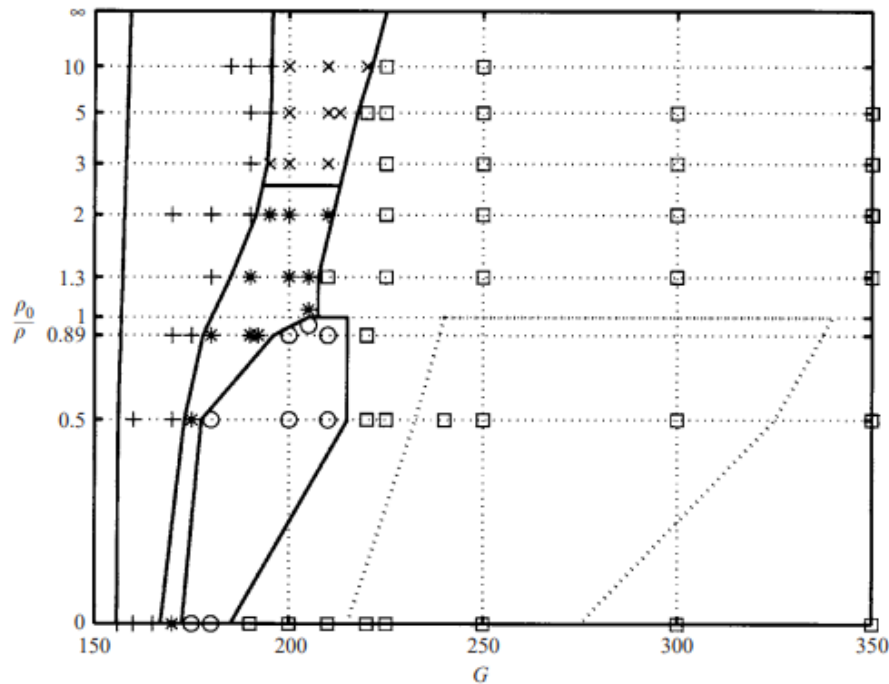
Figure 3.2 – Different particle settling regimes with respect the Galileo number and particle-to-fluid density ratio (G,ρ_0/ρ). To the leftmost line, the wake is axi-symmetric and consequently the particle settles or rises in a vertical line. A steady and oblique regime is denoted by $+$. An oblique and oscillating at low frequency regime is represented by $*$; while for high frequency $\times$ is used; $\circ$ indicates zigzagging periodic regime and the square symbol represents three-dimensional chaotic regime. The domain of coexistence of a chaotic and a periodic state is approximately delimited by the dotted line. Reprinted from Braza, Chassaing and Minh (1986).

must be done to obtain the solutions of the governing equations. The shear-rate dependent viscosity generates additional difficulties and several authors have extensively investigated the problems related to it.

The steady creeping motion of a sphere has been studied in a wide variety of generalized Newtonian fluid models. Indeed, it should be recognized that drag coefficients for non-Newtonian fluids are fluid model-dependent. Chhabra (2006) reviewed representative results obtained with some of the more widely used fluid models such as Power-law, Carreau and Ellis models for shear-thinning fluids.

Among all the models presented in literature, the Power-law model has been widely used in several studies, because it is simpler than other models. The theoretical analysis of these studies uses a drag correction factor, Y, which is a function of the Power-law index. Along the years, researchers have conducted dimensional analyses on Y and some efforts have been deposited in expanding the available correlations to the non-creeping flow regime. Most of the results reported by different investigators differ widely from one another as pointed out

in Chhabra (2006).

Analyses of a sphere's motion in a Power-law fluid have also been conducted by computational fluid dynamics (CFD). Details about the velocity field around a settling sphere in a Power-law fluid was presented by Keunings and Crochet (1984), who solved the continuity and momentum balance equations for the creeping motion of a spherical particle. As the value of the Power-law index decreases, the disturbance in the flow field due to the sphere movement is observed over shorter distances. This theory was found to be in agreement with experimental observations of Coutanceau and Bouard (1977) and with the experimental study of Whitney and Rodin (2001).

More than just measured values for drag force and terminal velocity, several qualitative results are of great interest in the literature. One interesting effect includes the aggregation of particles, commonly reported on the literature, especially for shear-thinning fluids. According to Daugan et al. (2002) the settling behavior of two particles released one after another in an infinity reservoir (disregarding wall effects) filled with shear-thinning fluid depends mainly of the initial distance between the two spheres. There is a critical distance in which the settling of the first particle do not interfere on the settling of the second one. If the initial distance is higher than a critical distance, both particles show the same instantaneous velocity. When the initial distance is smaller than the critical, the passage of the first particle produces a "corridor" of reduced viscosity and the second particle settles at higher velocities.

Recently, Goyal and Derksen (2012) applied a numerical procedure to solve the problem of particles sedimenting in viscoelastic fluids, based on lattice-Boltzmann method coupled to a finite volume method with the latter solving the elastic stress tensor. At first the transport equation was solved trough the application of an explicit finite volume scheme, allowing the elastic stress tensor to be determined. Then a lattice-Boltzmann time step was performed in the same manner, as it would be done for a Newtonian fluid (only with the additional elastic stress). The numerical settling experiments were performed in closed container with squared cross section (three-dimensional) with the particles moving relatively to a fixed grid. Goyal and Derksen (2012) observed that elasticity is responsible for an initial overshoot of the settling velocity. This overshoot is followed by a strongly damped oscillation: the oscillatory response is caused by the elastic-like behavior, whereas the damping is due to the viscous-like behavior of the fluid. Goyal and Derksen (2012) also analyzed the interaction of two spheres settling end-to-end and side-by-side in viscoelastic fluids. For the vertical configuration, the distance between the spheres decreases as they settle when released within a critical distance, similarly to the results reported by Daugan et al. (2002) for pseudoplastic fluids. In the horizontal side-by-side configuration the two spheres repel each other. Furthermore, according to the authors, wall effects significantly influence the settling velocities.

3.3 The Lattice-Boltzmann method (LBM)

Recently, LBM has been a promising alternative over the conventional CFD schemes that solve macroscopic variables such as velocity and pressure fields using the discretized Navier-Stokes equations. A review over LBM applied to solve particle−fluid interaction and to solve non−Newtonian fluids will be presented in this section.

3.3.1 LBM technique for fluid-solid interface

On their review paper, Liu et al. (2016) describe a number of different multiphase and multicomponent models, and also introduce how particle−fluid coupling can be simulated using the LBM. According to Liu et al. (2016), the term "multiphase" flow might not only describe mixtures of different fluids, but is also used to classify fluid flows with immersed objects such as in the case of particle settling. Thus, this sub-section is dedicated to present how particle-fluid coupling have been recently approached in the LBM framework.

A review of LBM for simulating particle-fluid interactions is also given by Behrend (1995), Yu and Fan (2010) and Silva et al. (2015). In general, the fluid-solid interface is usually subjected to the no-slip condition, which requires the local fluid velocity at the boundary to be equal to the solid velocity. However, the LBM is solved for particles distribution functions, and therefore it is required to translate the fluid velocity into the boundary condition for the particle distribution. This gives rise to a very efficient technique to impose the boundary condition, by simply reflecting the particle distributions moving into the solid region back into the fluid domain. This is the so called the "bounce back" condition, which is the most widely used scheme for both stationary and moving boundaries in the LBM (LADD; VERBERG, 2001). For moving boundaries, a generalization of the bounce back rule has been developed by Ladd and Frenkel (1990) *apud* Behrend (1995).

To simulate the hydrodynamic interactions between the fluid and the solid particle, the lattice-Boltzmann method has to be modified to incorporate the boundary conditions imposed on the fluid by the solid particles. Since most LBM simulations are performed on regular lattices, simulating a curved solid boundary becomes a complicate task. Figure 3.3 shows the location of the boundary nodes for a circular object of radius 2.5 lattice spacing, where the velocities along links crossing the boundary surface are indicated by arrows. The locations of the boundary nodes are shown by solid squares and the lattice nodes by solid circles.

The curved boundary may impose several issues to the problem. Yu et al. (2010) say that not only the accuracy of the bounce back degrades, but also the exact location of the boundary becomes ambiguous.

According to Yu et al. (2010) three different approaches to improve the fluid-solid boundary treatment are commonly used. The first one keeps the concept of bounce back of the distribution function but employs interpolation of the distribution depending on the distance
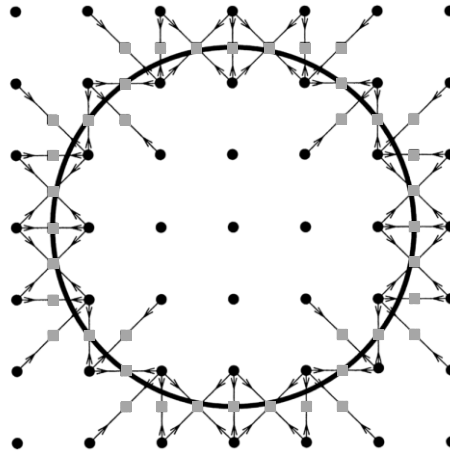
Figure 3.3 – Location of the boundary nodes for a spherical particle based on a D2Q9 lattice. The velocities along links crossing the boundary surface are indicated by arrows. The locations of the boundary nodes are shown by solid squares and the lattice nodes by solid circles. (reprinted from Ladd and Verberg (2001))

to the exact boundary. This approach was introduced by Lallemand and Luo (2003).

The second one is the immersed boundary approach, which uses a set of Lagrangian nodes to represent the solid particle surface immersed in the fixed Eulerian lattice. In this method, the velocity field is solved by adding a force density term into the lattice-Boltzmann equation and the immersed particle might be treated either as slightly deformable or as a rigid object. This approach is well described in Feng and Michaelides (2004).

The third approach maintains the efficient bounce back scheme, and simply takes advantage of a refined grid resolution near the solid surface by using adaptive mesh refinement (AMR) and the multi-block approach (for fixed solid boundaries). For moving boundaries, Yu and Fan (2010) applied a block-structured AMR algorithm similar to the one showed in Fig. 3.4.
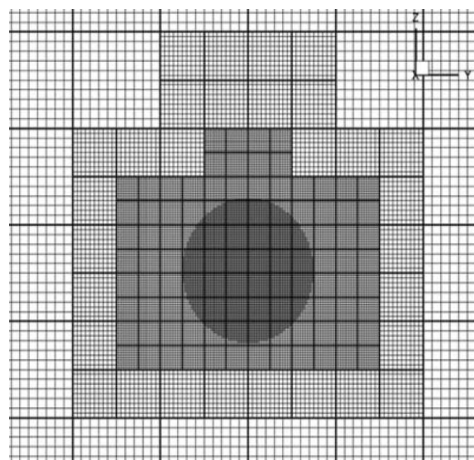
Figure 3.4 – Mesh resolution for particle settlement using uniform adaptive mesh for a 2D particle in a fluid. (adapted from Yu and Fan (2010))

3.3.2   LBM approach for non-Newtonian effects

Many efforts have been made to account for non-Newtonian effects in lattice-Boltzmann simulations. Most of the papers consider Power-law fluids, however contributions on multi-phase flow combined with non-Newtonian fluids in LBM are still rare.

Simulations of flow of purely viscous thixotropic fluids with no elasticity effects in mixing tanks were performed with a lattice-Boltzmann scheme Derksen and Prashant (2009). A simple thixotropic model was applied, the same one described by Mujumdar et al. (2002), and the numerical approach was verified with benchmark cases: simple shear flow, plane Poiseuille flow. The transient numerical results were compared with semi-analytical solutions and the flow in a lid-driven cavity compared the Bingham-like fluids with literature data. Since it is an expensive approach, in terms of computer memory usage, to solve the transport equation for the structural parameter in a LBM context, the authors solved it with an explicit finite volume discretization on the same uniform and cubic grid as the lattices in LBM. This approach also allows for suppression of numerical diffusion.

In the same year, Derksen (2009) published a numerical study of the drag on random assemblies of spheres in shear-thinning thixotropic fluids using LBM. The same thixotropic model of Derksen and Prashant (2009) was applied. The transport equation for the network parameter was solved by means of a finite volume scheme. The no-slip condition at the sphere surface was imposed by an adaptive force field approach (which is a type of immersed boundary method). This method was validated in the work published by Cate et al. (2002) by comparing simulation results of a single sphere sedimenting in a Newtonian fluid in a closed container with image velocimetry experiments of the same system. Good agreement in terms of the sphere trajectory, as well as the flow field induced by the motion of the falling sphere were observed as shown in Fig. 3.5. The figure shows the flow field of the sphere near to the bottom at four considered Re. $|u|$ is the fluid velocity and u_∞ is the theoretical steady-state velocity of a freely moving sphere in an infinite medium. The ratio $|u|/u_\infty$ indicates the normalized velocity magnitude.

2D simulations of a particle settling in Power-law fluids were conducted by Delouei et al. (2016). The authors applied an immersed boundary method coupled with lattice-Boltzmann method to solve this problem. The Power-law index n was then changed and the particle settling velocity and trajectory were presented. They observed that the particle settling dynamics is highly affected by n. In general, the particle settling velocity decreases as n increases.

3.4   Contribution of the present work

The settling of spherical particles have been the subject of several research studies. Since the pioneering work of Stokes (1851), much effort has been made to extend the
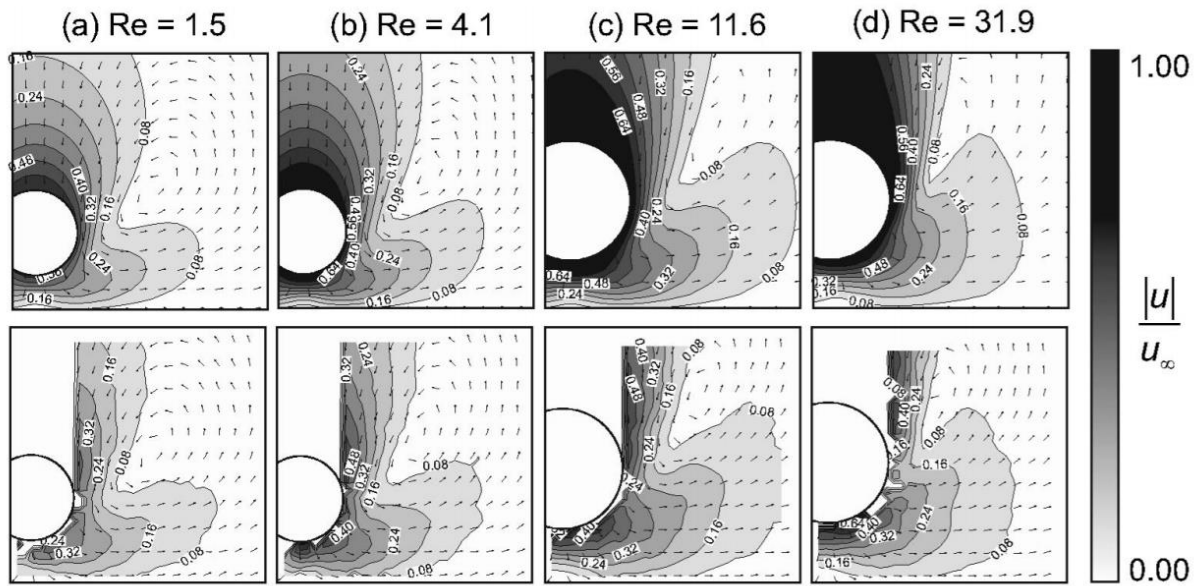
Figure 3.5 – Comparison of the simulated (top) and measured (bottom) flow field of the sphere. Contours indicate the normalized velocity magnitude; the vectors indicate the direction of the fluid flow only. (Reprinted from Cate et al. (2002))

analysis of the particle settling dynamics to out of the creeping flow region and to include effects of fluids with more complex behaviors. The Power-law model has been widely used to describe shear-thinning and shear-thickening behavior. The literature review showed that lattice-Boltzmann method is a recurrent tool when it comes to multiphase flow studies. The focus given during the literature review was for studies that presented a solid phase immersed in a fluid phase of high rheological complexity. A number of recent developments in the application of the lattice-Boltzmann method clearly demonstrates its versatility.

Based on the literature review, it was perceived a lack of information available on the behavior of particle sedimentation in non-Newtonian fluids. Given the applicability of this problem, as briefly described in Chapter 1, the contribution of the present work is the development of a numerical code based on LBM capable to simulate particle settling in Power-law fluids.

Next chapter presents a mathematical description of the problem investigated in this work.

4 Problem Formulation

In this chapter the necessary equations to describe the physics of the problem and also the mathematical considerations adopted to adequately simplify the problem are presented.

4.1 Geometry and boundary conditions

The schematic of the problem is shown in Fig. 4.1. The geometry resembles to the one investigated by Kang (2010), Dash (2014) and Delouei et. al. (2016). It considers an initially stationary particle in a rectangular container of height H and length L filled with a Power-law fluid. The particle of diameter d exerts a downward shear force on the fluid due to gravitational effects. The 2D particle is a rigid circumference with geometrical dimensions and density (ρ_p) considered to be constant. The problem is treated as two-dimensional in a Cartesian coordinate system (x, y), where x and y are the horizontal and vertical coordinates, respectively, and gravity $\mathbf{g}$ is pointing to the $-y$ direction.
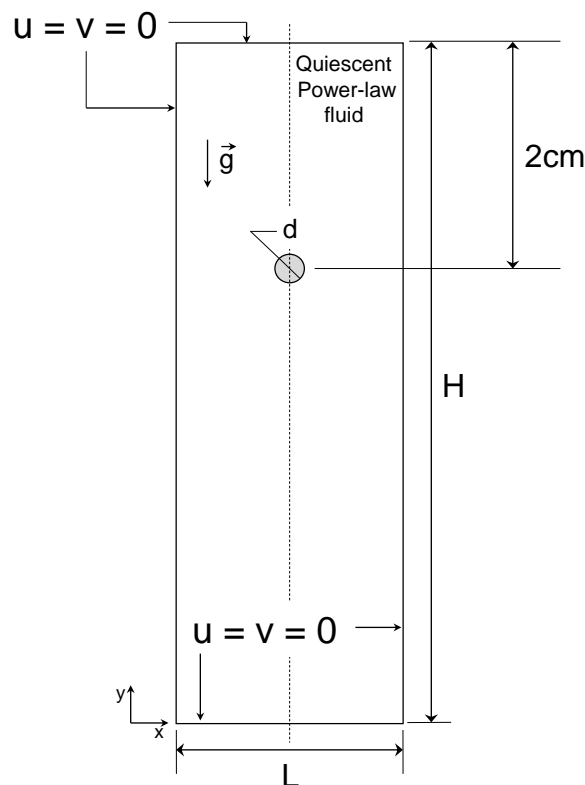
Figure 4.1 – Geometry and boundary conditions for particle settling in Power-law fluid problem addressed in this work.

As shown in Fig. 4.1 the boundary condition imposed on all solid walls, including the particle surface, is the no-slip condition, which states that the fluid velocity must be the same

as the solid boundary velocity. For the container stationary boundaries the no-slip condition gives:

$$u = v = 0 \qquad (4.1)$$

where u and v are the fluid velocity components.

For the particle moving boundary the no-slip condition gives:

$$\begin{aligned} u &= U_{p,s} \\ v &= V_{p,s} \end{aligned} \qquad (4.2)$$

where $U_{p,s}$ and $V_{p,s}$ are respectively the x and y velocity components at the particle surface.

Based on the problem description it is possible to obtain a mathematical formulation by dividing the system into two sets of equations: one for the fluid phase and another for the particle motion.

4.2 Fluid phase balance equations

Fluid motion is governed by the usual conservation equations for mass and momentum flow given by (BIRD et al., 1977):

$$\frac{\partial \rho_f}{\partial t} + \nabla \cdot \rho \mathbf{u} = 0 \qquad (4.3)$$

$$\frac{\partial (\rho_f \mathbf{u})}{\partial t} + \nabla \cdot \rho \mathbf{u}\mathbf{u} = \rho_f \mathbf{g} - \nabla \cdot \boldsymbol{\sigma} \qquad (4.4)$$

where $\boldsymbol{\sigma}$ is the momentum flux tensor and can be written as:

$$\boldsymbol{\sigma} = -p\boldsymbol{\delta} + \boldsymbol{\tau} \qquad (4.5)$$

where $\boldsymbol{\tau}$ is the viscous stress tensor and $\boldsymbol{\delta}$ is the Kronecker delta tensor.

The relationship between the viscous stress tensor ($\boldsymbol{\tau}$) and shear strain rate ($\dot{\gamma}$) is presented in section 2.1.1 along with the Power-law model used to represent the apparent viscosity change with changing the shear strain rate.

For an incompressible fluid undergoing a laminar two-dimensional flow, under isothermal conditions, the governing equations in Cartesian coordinates are:

$$\frac{\partial u_x}{\partial x} + \frac{\partial u_y}{\partial y} = 0 \qquad (4.6)$$

$$\rho_f \left(\frac{\partial u_x}{\partial t} + u_x \frac{\partial u_x}{\partial x} + u_y \frac{\partial u_x}{\partial y} \right) = -\frac{\partial p}{\partial x} + \frac{\partial \tau_{xx}}{\partial x} + \frac{\partial \tau_{yx}}{\partial y} \tag{4.7}$$

$$\rho_f \left(\frac{\partial u_y}{\partial t} + u_x \frac{\partial u_y}{\partial x} + u_y \frac{\partial u_y}{\partial y} \right) = -\frac{\partial p}{\partial y} + \frac{\partial \tau_{xy}}{\partial x} + \frac{\partial \tau_{yy}}{\partial y} + \rho_f g_y \tag{4.8}$$

4.3   Particle motion equations

Based on Newton's second law of motion it is possible to represent the motion of an individual particle, expressed by (DERKSEN, 2016):

$$m_p \frac{d\mathbf{v_p}}{dt} = m_p \frac{d^2\mathbf{x_p}}{dt^2} = \sum \mathbf{F_p} = \mathbf{F_{p,b}} + \mathbf{F_{p,s}} + \mathbf{F_{p,c}} \tag{4.9}$$

where $\mathbf{x_p}$ is the position vector of the particle, m_p is the particle mass, $\mathbf{v_p}$ is the translational particle velocity. The forces $\mathbf{F_p}$ may be divided into the body force $\mathbf{F_{p,b}}$, the surface forces $\mathbf{F_{p,s}}$ and the contact forces $\mathbf{F_{p,c}}$. $\mathbf{v_p}$ and $\mathbf{x_p}$ are respectively:

$$\mathbf{v_p} = v_{p,x}\mathbf{e_i} + v_{p,y}\mathbf{e_j} \tag{4.10}$$

$$\mathbf{x_p} = x_p\mathbf{e_i} + y_p\mathbf{e_j} \tag{4.11}$$

The particle trajectory over time is obtained by determining the forces acting on the particle at each time instant. The velocity and position of the particle are then updated through the expression:

$$\frac{d\mathbf{x_p}}{dt} = \mathbf{v_p} \tag{4.12}$$

The gravitational force $\mathbf{F_{g,b}}$, is the main and only body force considered in this work, expressed by:

$$\mathbf{F_{p,b}} = \mathbf{F_{g,b}} = \rho_p V_p \mathbf{g} \tag{4.13}$$

where V_p is the particle volume.

The surface forces $\mathbf{F_{p,s}}$, are due the fluid-particle interaction, which may generate pressure forces and viscous stresses. Different types of surface forces can be considered for the trajectory of the particle in the mathematical model. The main surface forces considered in this work are the drag and buoyant forces.

The drag force is by definition a resistance force caused by the motion of a body through a fluid medium. The drag force acts opposite to the body motion. Generically, the drag force can be expressed in terms of drag coefficient, C_D (CROWE et al., 2011):

$$\mathbf{F_{d,s}} = \frac{1}{2} C_D \rho_f A_p \left| \mathbf{v_p} \right| \mathbf{v_p} \tag{4.14}$$

where A_p is the projected area of the particle.

The buoyant force $\mathbf{F_{by,s}}$, is defined as a force proportional to the weight of displaced fluid and acts in the opposite direction of gravity acceleration. The displaced fluid is the volume of the object. The buoyant force is expressed by:

$$\mathbf{F_{by,s}} = -\rho_f V_p \mathbf{g} \tag{4.15}$$

The contact forces $\mathbf{F_{p,c}}$ are due to the collision between particle and bounding walls. Contact forces were neglected in this present study, since the variables of interest are terminal velocity and drag coefficient.

The Newton's equation of angular particle motion states that the net external torque about the particle center is equal to the rate of change of angular momentum about its center.

$$I_s \frac{d\mathbf{\Omega_s}}{dt} = \sum \mathbf{r} \times \mathbf{F_p} \tag{4.16}$$

where I_s is the particle momentum of inertia, $\mathbf{\Omega_s}$ is the particle angular velocity and $\mathbf{r}$ is the position vector of a force applied at the particle surface relative to the particle center.

Since the particle is release from rest in the quiescent fluid, the initial conditions for this problem are:

$$\text{At} \quad t = 0 \rightarrow U_{p,s} = V_{p,s} = \mathbf{\Omega_s} = 0 \tag{4.17}$$

4.4 Particle-fluid coupling

The particle-fluid coupling is done through a direct force immersed boundary method. This is done by adding a force term ($\mathbf{f}$) in the equation of momentum. The term $\mathbf{f}$ is a volume force and is formulated to represent the action of the immersed solid boundaries upon the fluid. Thus, Eq. 4.4 is written as:

$$\frac{\partial(\rho_f \mathbf{v})}{\partial t} = \rho_f \mathbf{g} - \nabla \cdot \rho \mathbf{v}\mathbf{v} - \nabla \cdot \boldsymbol{\sigma} + \mathbf{f} \tag{4.18}$$

4.5 Flow defnition and dimensionless numbers

The generalized Reynolds number defined in Eq. 4.19 is the most representative dimensionless number in Non-Newtonian fluid flow over stationary objects. Most of the studies regarding flow past an obstacle report results for drag coefficient as a function of generalized Reynolds number (BIRD et al., 1977), which is given as:

$$Re_{pl} = \frac{V_p^{2-n}d^n}{\nu} \tag{4.19}$$

However, for the cases of free falling particles in a fluid, correlate Reynolds number with the drag coefficient experienced by the particle may not be convenient since the settling velocity is not previously known. To overcome this issue, a new dimensionless group is introduced, known as the modified Archimedes number (CHHABRA, 2006):

$$Ar = C_{D,T}Re_{pl}^{2/(2-n)} \tag{4.20}$$

where $C_{D,T}$ is the drag coefficient experienced by the particle at its terminal settling velocity, obtained by a force balanced applied on the particle, yielding:

$$C_{D,T} = \frac{\pi}{2}\frac{gd(\rho_r - 1)}{V_T^2} \tag{4.21}$$

where ρ_r is the solid to fluid density ration and V_T is the terminal settling velocity.

Replacing $C_{D,T}$ and Re_{pl} in Eq. 4.20, the modified Archimedes number is then defined as:

$$Ar_{pl} = \frac{\pi}{2}\frac{gd^{\frac{2+n}{2-n}}}{m^{\frac{2}{2-n}}}(\rho_r - 1) \tag{4.22}$$

As shown by Eq. 4.22, the Archimedes number is a function only of fluid and particle properties, thus, regardless of the particle/Power-law fluid combination, the right-hand side of Eq. 4.22 is known. This dimensionless number relates the gravitational and viscous forces.

This approach makes it easier to conduct studies for settling particles where the results are now a function of a dimensionless number that does not depend on the particle settling velocity.

4.6 Chapter enclosure

The mathematical basis needed to solve the problem addressed in this work was introduced in this chapter. Initially, the geometry and boundary conditions were presented.

Then, mass and momentum balance equations for the fluid phase were presented together with the Newton's law of movement equations for the particle. In the following Chapter, the numerical approach used to solve the mathematical problem formulated in this chapter will be presented.

5 Numerical Method

In this chapter the numerical method used to solve the proposed problem is presented. Since the lattice Boltzmann method has its roots in the lattice gas automata (LGA) it is interesting to explain how LGA works before move on with LBM. LGA is a kinetic model with discrete lattice and discrete time (MELE, 2013). The model idea consists of particles that can move around lattice nodes in specific directions, as shown in Fig. 5.2. A set of boolean (true or false) variables, n_k is then introduced to represent the presence of a particle within a lattice node:

$$n_k(\mathbf{x}, t) \quad i = 0, ...M \tag{5.1}$$

where M is the number of directions k of particle velocities at each lattice node and n can be either 0 or 1, that is:

$$\begin{aligned} n_k(\mathbf{x}, t) = 0 & \quad \text{no particles at site } x \text{ and time } t \\ n_k(\mathbf{x}, t) = 1 & \quad \text{particle located at site } x \text{ and time } t \end{aligned} \tag{5.2}$$
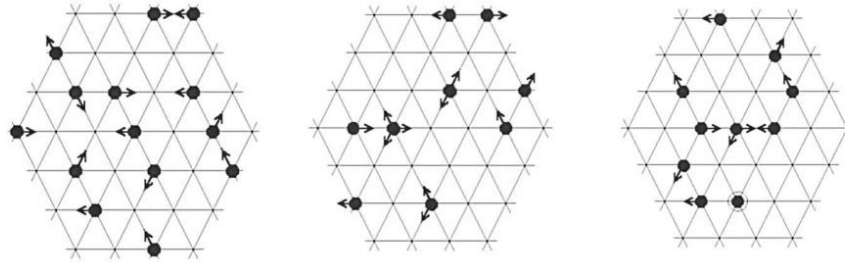
Figure 5.1 – Fluid particles travel on the lattice nodes. (from Benedetto and Umiliaco (2013))

The evolution equation of the LGA can be written as:

$$n_k(\mathbf{x} + \mathbf{e_k}\delta t, t + 1) = n_k(\mathbf{x}, t) + \Omega_k(n(\mathbf{x}, t)), \quad k = 0, ...M \tag{5.3}$$

where $\mathbf{e_k}$ are local particle velocities, Ω_k is the collision operator and δt is time step. In this equation the collision operator Ω_k changes the occupation number n due to collision at site k and can have values -1, 0, 1. -1 means that the particle was *destroyed*, 0 leaves things unchanged and 1 means new particle is *created* (MELE, 2013). Therefore, boolean nature is preserved. It is important to stress out that interaction is local, that is, neighboring sites do

not interact and there is also an exclusion rule, forbidding two particles sitting on the same node. The configuration of particles at each time step involves two sequential sub-steps:

Streaming (advection), in which each particle moves to the next (nearest) node in the direction of its velocity, and

Collision, which happens when particles arrive at a node and interact with each other due to the previously defined collision rules.

If the operator Ω is set to zero, then an equation for streaming alone is obtained.

5.1   From LGA to LBM - the lattice-Boltzmann equation

The major issue with lattice gases was the statistical noise (KRÜGER et al., 2017). The greatest motivation for the transition from LGA to LBM was the desire to remove this statistical noise by replacing particle occupation variables (boolean variables) with single particle distribution functions:

$$f = \langle n \rangle \tag{5.4}$$

where n can be 0 or 1 whereas f is an average of n and can be any real number between 0 and 1 (CHEN; DOOLEN, 1998). To obtain the macroscopic behavior of a system in LGA it is necessary to average consecutive time steps (CHOPARD; DROZ, 1998).

The distribution function $f(\mathbf{x}, \mathbf{e}, t)$ depends on the position vector $\mathbf{x}$, the velocity vector $\mathbf{e}$ and time t. This function represents the number of particles with mass m positioned between $\mathbf{x}$ and $\mathbf{x} + d\mathbf{x}$ with velocities between $\mathbf{e}$ and $\mathbf{e} + d\mathbf{e}$ at time t. Applying a force $\mathbf{F}$ on these particles, after a time dt, position and velocity have new values (MOHAMAD, 2011):

$$
\begin{aligned}
\text{position} \quad & \mathbf{x} \to \mathbf{x} + \mathbf{e}dt \\
\text{velocity} \quad & \mathbf{e} \to \mathbf{e} + \frac{\mathbf{F}}{m}dt
\end{aligned}
\tag{5.5}
$$

The particle position and velocity vectors changes due an external force are schematically shown in Fig. X.

If there is no collision, the particle distribution function before and after applying force remains the same:

$$f(\mathbf{x} + \mathbf{e}dt, \mathbf{e} + \frac{\mathbf{F}}{m}dt, t + dt)d\mathbf{x}d\mathbf{e} = f(\mathbf{x}, \mathbf{e}, t)d\mathbf{x}d\mathbf{e} \tag{5.6}$$
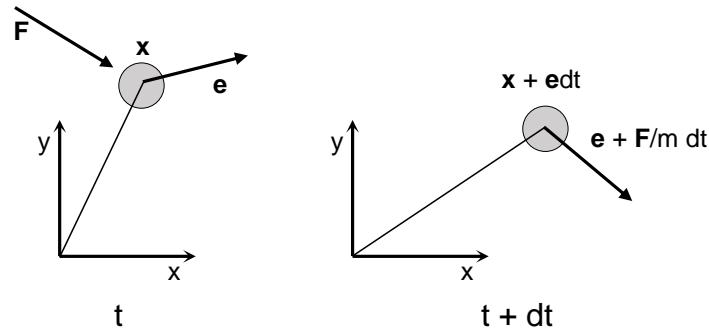
Figure 5.2 – Position and velocity vector for a particle after and before applying a force.

On the other hand, if collision happens, then:

$$f(\mathbf{x} + \mathbf{e}dt, \mathbf{e} + \frac{\mathbf{F}}{m}dt, t + dt)d\mathbf{x}d\mathbf{e} - f(\mathbf{x}, \mathbf{e}, t)d\mathbf{x}d\mathbf{e} = \Omega(f)\,d\mathbf{x}d\mathbf{e}dt \qquad (5.7)$$

where Ω is the collision operator that models the rate of change of the particle distribution function f due to molecular collisions.

Dividing Equation 5.7 by $d\mathbf{x}d\mathbf{e}dt$ and in the limit $dt \to 0$ leads to:

$$\frac{Df}{Dt} = \Omega(f) \qquad (5.8)$$

where D/Dt is the material derivative.

Equation 5.8 states that the total rate of change of the distribution function is equal to the rate of the collisions (MOHAMAD, 2011). Expanding the material derivative on the left side of Eq. 5.8 and dividing by dt results in:

$$\frac{Df}{dt} = \frac{\partial f}{\partial \mathbf{x}}\frac{d\mathbf{x}}{dt} + \frac{\partial f}{\partial \mathbf{e}}\frac{d\mathbf{e}}{dt} + \frac{\partial f}{\partial t} \qquad (5.9)$$

where the Fraction $d\mathbf{x}/dt$ represents the velocity $\mathbf{e}$, the fraction $d\mathbf{e}/dt$ represents the acceleration $\mathbf{a}$, which can be related to force $\mathbf{F}$ by Newton's second law such that $\mathbf{a} = \mathbf{F}/m$. Combining Eqs. 5.8 and 5.9 results in the Boltzmann Transport Equation (MOHAMAD, 2011):

$$\frac{\partial f}{\partial t} + \mathbf{e}\frac{\partial f}{\partial \mathbf{x}} + \frac{\mathbf{F}}{m}\frac{\partial f}{\partial \mathbf{e}} = \Omega(f) \qquad (5.10)$$

where the second right hand side term represents the advection of the distribution function. The third term represents forces acting on the system.

5.2 Collision Operator

The collision operator Ω is in general a complex non-linear integral (MOHAMAD, 2011), which means that Boltzmann Equation is a nonlinear integro-differential equation. To simplify this equation, Bhatnagar, Gross and Krook (1954) introduced a model where Ω is replaced by the so-called BGK collision operator, given by:

$$\Omega_{BGK} = -\frac{1}{\lambda}\left(f - f^{EQ}\right) \tag{5.11}$$

where λ is the mean relaxation time and f^{EQ} is the Maxwellian equilibrium distribution function (see section 5.3.1). In general, the mean relaxation time λ is a single constant.Thus the BGK operator is often called single-relaxation-time (SRT) (SUCCI, 2001). Equation 5.11 shows that at each collision the distribution function f changes by an amount proportional to the difference $f - f^{EQ}$. The equilibrium function is discussed in section 5.3.1.

The central idea of this simplification is to linearize the collision term around its local equilibrium solution. In general, the collision operator may have different forms all of which locally conserve momentum and, thus, yielding the correct macroscopic behavior of the system (KRÜGER et al., 2017). The most important properties of collision operators are mass and momentum conservation (KRÜGER et al., 2017), both fulfilled by the BGK-operator.

After introducing the BGK operator, the simplified Boltzmann equation can be written as:

$$\frac{\partial f}{\partial t} + \mathbf{e}\frac{\partial f}{\partial \mathbf{x}} + \frac{\mathbf{F}}{m}\frac{\partial f}{\partial \mathbf{e}} = -\frac{1}{\lambda}\left(f - f^{EQ}\right) \tag{5.12}$$

Equation 5.12 is the BGK-Boltzmann Equation, it is the most popular kinetic model and replaces Navier-Stokes equation in CFD simulations.

5.3 Discretized Boltzmann Equation - the lattice-Boltzmann method

The lattice-Boltzmann Equation is derived from the continuous Boltzmann Equation by the discretization of the velocity space. Based on the concepts of the kinetic theory of gases, the lattice-Boltzmann Method (LBM) considers the fluid as a system of particles, represented by a distribution function f, which obey streaming and collision processes. The temporal evolution of the system state occurs in time intervals, with streaming and collisions between sets of particles occurring in a discrete spatial domain, the lattices. At each time step, these set of particles interact with each other under collision rules defined by Ω at a lattice node

and move to neighboring nodes according to a finite and predefined set of orientations and velocities, determined according to the lattice structure.

The common terminology for a velocity set makes reference to the dimension of the problem and the number of microscopic velocities – DnQm (MOHAMAD, 2011); n represents the dimension of a problem and m represents the velocity model (number of velocity values by which the continues velocity space is discretized). Since relative spacing between a node and the central node is not always the same, nodes in different positions regarding the central node must have appropriate weighting factors, w_k. These factors depend on the distance from the central node.

Exemplary velocity sets for 2D simulations of hydrodynamics problems are show in Fig.5.3. The most popular for 2D cases is the D2Q9 arrangement. However, there are higher order models such as the D2V17 shown in Fig.5.4.
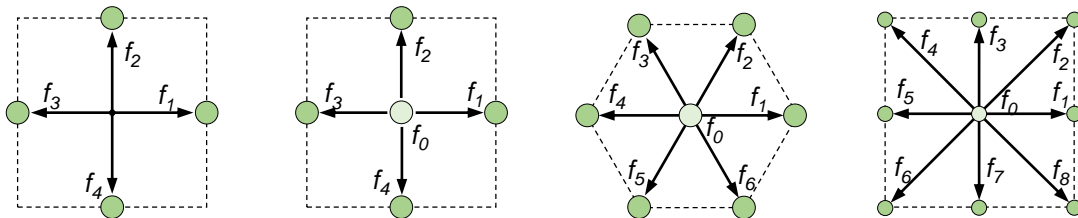
Figure 5.3 – some widely known 2D set pf lattice vectors. From left to right: D2Q4, D2Q5, D2Q7 and D2Q9
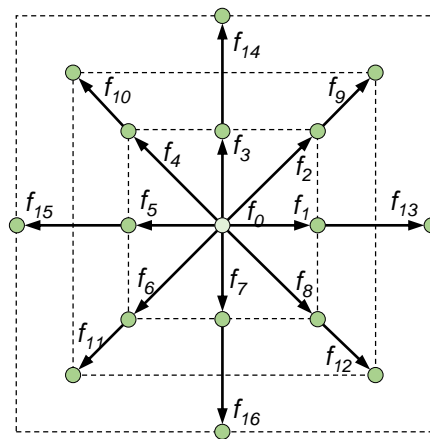
Figure 5.4 – Third order D2V17 set of lattice vectors.

D2Q9 has been widely and successfully used for simulations of two-dimensional flows. It is described as nine-velocity square lattice model. It is a bit more demanding from a computational aspect than the hexagonal D2Q7 model, although, more accurate. It has to be stressed out that for fluid flow problems where non-linear terms in Navier-Stokes (NS) equation are important, the D2Q4 or D2Q5 model are not appropriate because of insufficient lattice symmetry. It fails to achieve basic symmetry of NS equation – rotational invariance.

Consequently, the lattice-Boltzmann equation cannot recover the correct NS equation on inappropriate lattices (Chen and Doolen (1998) and Mohamad (2011)). For this reason, the D2Q9 model is used in the present work.

The discrete Boltzmann equation is directly derived by integrating the general evolution equation (BGK-Boltzmann Equation), given by Eq. 5.12. At first, Eq. 5.12 can be rewritten as:

$$\frac{\partial f}{\partial t} + \mathbf{e}\frac{\partial f}{\partial \mathbf{x}} + F_t = -\frac{1}{\lambda}\left(f - f^{EQ}\right) \tag{5.13}$$

where F_t is the force term that will be discussed later. Integrating Eq. 5.13 along the characteristic lines of the velocity set, as done by He, Chen and Doolen (1998) and then performing Taylor series expansion up to the first-order in time, it gives the following discrete evolution equation:

$$f(\mathbf{x} + \mathbf{e}\Delta t, \mathbf{e}, t + \Delta t) = f(\mathbf{x}, \mathbf{e}, t) - \frac{1}{\tau}\left(f - f^{EQ}\right) + F_t(\mathbf{x}, t)\Delta t \tag{5.14}$$

where $\tau = \lambda/\Delta t$ is the dimensionless mean relaxation time and Δt is the time step. Discretizing Eq. 5.14 in the velocity space gives the following discrete BGK - lattice-Boltzmann equation:

$$f_k(\mathbf{x} + \mathbf{e_k}\Delta t, t + \Delta t) = f_k(\mathbf{x}, t) - \frac{1}{\tau}\left[f_k(\mathbf{x}, t) - f_k^{EQ}(\mathbf{x}, t)\right] + F_{t,k}(\mathbf{x}, t)\Delta t \tag{5.15}$$

where $\mathbf{e_k}$ is the discrete velocity and k ranges from 0 to $m - 1$ and represents the available directions in the lattice space, $f_k(\mathbf{x}, t) \equiv f(\mathbf{x}, \mathbf{e_k}, t)$ is the discrete particle distribution function, $f_k^{EQ}(\mathbf{x}, t)$ is the discrete equilibrium particle distribution function and F_k is the discrete force distribution function.

5.3.1 The equilibrium function f^{EQ}

The equilibrium distribution function f^{EQ}, which appears in the BGK collision operator, is basically an expansion of the Maxwell-Boltzmann distribution function for low Mach number Ma. According to Mohamad (2011) the normalized Maxwell's distribution function is given by:

$$f = \frac{\rho}{2\pi/3}e^{-\frac{3}{2}(\mathbf{e}-\mathbf{u})^2} = \frac{\rho}{2\pi/3}e^{-\frac{3}{2}(\mathbf{e}\cdot\mathbf{e})}e^{\frac{3}{2}(\mathbf{e}\cdot\mathbf{u}-\mathbf{u}\cdot\mathbf{u})} \tag{5.16}$$

where $\mathbf{u}$ is the macroscopic velocity of particles in a medium, $\mathbf{e}$ are the velocity vectors in a specific lattice model and ρ is the macroscopic density. Equation 5.16 can be expanded in Taylor series with velocity $\mathbf{u}$ up to second order. This is valid for small velocities $Ma = u/c_s << 1$, where c_s represents the speed of sound. Thus, Eq. 5.16 results in:

$$f = \frac{\rho}{2\pi/3} e^{-\frac{3}{2}(\mathbf{e} \cdot \mathbf{e})} \left[1 + 3 \left(\mathbf{e} \cdot \mathbf{u} \right) - \frac{3}{2} \left(\mathbf{u} \cdot \mathbf{u} \right) + \frac{9}{2} \left(\mathbf{e} \cdot \mathbf{u} \right)^2 \right] \tag{5.17}$$

The non-linearity of the collision operator is then hidden and the discrete equilibrium distribution function is given by:

$$f_k^{EQ} = \rho w_k \left[1 + 3 \left(\mathbf{e_k} \cdot \mathbf{u} \right) - \frac{3}{2} \left(\mathbf{u} \cdot \mathbf{u} \right) + \frac{9}{2} (\mathbf{e_K} \cdot \mathbf{u})^2 \right] \tag{5.18}$$

where $w_k = e^{-\frac{3}{2}e^2}/(2\pi/3)$ are weighting factors (SUCCI, 2001).

In D2Q9 model, discrete velocity vectors, $\mathbf{e_k}$, and the corresponding weighting coefficients, w_k, are respectively given by Eqs. 5.19 and 5.20.

$$\mathbf{e_k} = c \begin{cases} (0,0) & k = 0 \\ (\pm 1, 0), (0, \pm 1) & k = 1, 2, 3, 4 \\ (\pm 1, \pm 1) & k = 5, 6, 7, 8 \end{cases} \tag{5.19}$$

$$w_k = \begin{cases} 4/9, & k = 0 \\ 1/9, & k = 1, 2, 3, 4 \\ 1/36, & k = 5, 6, 7, 8 \end{cases} \tag{5.20}$$

where c is the lattice speed $c = \Delta x / \Delta t$ and the direction k is positioned in lattice space as shown in Fig. 5.5:

5.4   Macroscopic quantities

Macroscopic fluid/flow quantities (e.g. density and velocity) are directly obtained by solving the Navier-Stokes equation. In the LBM, macroscopic quantities are obtained by the distribution function moments. These moments are integrals of f, weighted with some function of $\mathbf{e}$ over the entire velocity space.
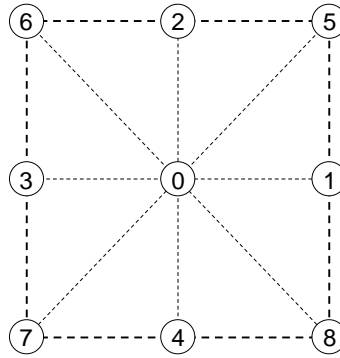
Figure 5.5 – The k position in the lattice space.

The Boltzmann equation describes multiple macroscopic physics, e.g, from mass conservation to momentum and energy transport. However, discretized velocity space sets of lower order cause the numerical method to loose the higher-order physics being therefore necessary to use discretized velocity sets of higher order as the D2V17. In the present work only mass and momentum conservation are of interest and D2Q9 velocity space is enough to solve this problem. Connections of the distribution function to macroscopic quantities for the fluid density, ρ, fluid velocity, $\mathbf{u}$, and internal energy, $\mathbf{E}$ are defined as follows:

$$\rho\left(\mathbf{x}, t\right) = m \int f\left(\mathbf{x}, \mathbf{e}, t\right) d\mathbf{e} \tag{5.21}$$

$$\rho\left(\mathbf{x}, t\right) \mathbf{u}\left(\mathbf{x}, t\right) = m \int f\left(\mathbf{x}, \mathbf{e}, t\right) \mathbf{e} d\mathbf{e} \tag{5.22}$$

$$\rho\left(\mathbf{x}, t\right) \mathbf{E}\left(\mathbf{x}, t\right) = m \frac{1}{2} \int u_a^2 f\left(\mathbf{x}, \mathbf{e}, t\right) d\mathbf{e} \tag{5.23}$$

where m is the molecular mass and u_a is the particle velocity relative to the fluid velocity.

The discretized macroscopic moments (density and momentum) can be computed from finite sums as:

$$\rho = \sum_i f_i = \sum_i f_i^{EQ} \tag{5.24}$$

$$\rho\mathbf{u} = \sum_i f_i \mathbf{e_i} = \sum_i f_i^{EQ} \mathbf{e_i} \tag{5.25}$$

5.4.1 The recovering of Navier-Stokes equation

The Navier-Stokes equation (NSe) can be recovered from a Chapman-Ensokg analysis, which gives the kinematic viscosity ν in terms of the single relaxation time λ (KRÜGER et al., 2017):

$$\nu = \left(\lambda - \frac{\Delta t}{2} \right) c_s^2 \tag{5.26}$$

where c_s is the sound speed in the lattice given by:

$$c_s = \frac{1}{\sqrt{3}} \frac{h}{\Delta t} \tag{5.27}$$

where $h = \Delta x = \Delta y$ is the Eulerian mesh space.

5.5 The forcing term $F_{t,k}$ and the Immersed Boundary Method

The force term $F_{t,k}$ in the discrete Lattice-Boltzmann equation (Eq. 5.15) is important in the immersed boundary method (IBM) because it is through this term that the system is able to recognize the existence of a boundary. According to Zheng, Zheng and Zhai (2017), in order to keep the consistence of the simplified lattice-Boltzmann equation (Eq. 5.13) the general formulation of $F_{t,k}$ should be carefully chosen in order to allow the recovery of NSe when multi-scale Chapman-Enskog expansion is performed. For this reason, as done by Kang (2010) and Dash (2014), the present work follows the split-forcing method proposed by (GUO; ZHENG; SHI, 2002), which enables the LBE to recover NSe with second-order accuracy.

Guo, Zheng and Shi (2002) inserted the external force to the momentum by redefining the macroscopic momentum, given by Eq. 5.25, as:

$$\rho \mathbf{u} = \sum_i f_i \mathbf{e_i} + \frac{\Delta t}{2} \mathbf{f} \tag{5.28}$$

where $\mathbf{f}$ is the force density at Eulerian fluid nodes, which is distributed from the force density of Lagrangian boundary points. This procedure will be discussed further on.

Then, the discrete force distribution function, F_k, is given by:

$$F_k(\mathbf{x}, t) = \left(1 - \frac{1}{2\tau} \right) w_k \left[3 \frac{\mathbf{e_k} - \mathbf{u}(\mathbf{x}, t)}{c_s^2} + 9 \frac{\mathbf{e_k} \cdot \mathbf{u}(\mathbf{x}, t)}{c_s^4} \mathbf{e_k} \right] \cdot \mathbf{f}(\mathbf{x}, t) \tag{5.29}$$

which satisfies the following relations of the 0th and 1st moments (LUO, 2000):

$$\sum_k F_k(\mathbf{x}, t) = 0 \tag{5.30}$$

$$\sum_k \mathbf{e}_k F_k(\mathbf{x}, t) = \left(1 - \frac{1}{2\tau}\right) \mathbf{f}(\mathbf{x}, t) \tag{5.31}$$

5.5.1 Calculating the force density, f

Analyzing Eq. 5.28 it can be seen that the fluid velocity is affected by two parts. The first one, in the right-hand side of Eq. 5.28, is computed from the density distribution function and is referred here as an unforced Eulerian velocity, given by Eq. 5.32, and is evaluated using Eq. 5.15 without a forcing term.

$$\mathbf{u^{noF}} = \sum_i f_i \mathbf{e_i} / \rho \tag{5.32}$$

The second term is the Eulerian velocity correction given by Eq. 5.33.

$$\Delta \mathbf{u} = \frac{\Delta t}{2\rho} \mathbf{f}(\mathbf{x}, t) \tag{5.33}$$

The force density $\mathbf{f}(\mathbf{x}, t)$ is not known and the Eulerian velocity correction $\Delta \mathbf{u}$ is implicitly calculated such that the exact no-slip boundary condition is satisfied. From a mathematical perspective, it implies that the fluid velocity at the boundary must be equal to the boundary velocity $\mathbf{U_B}^l$ at the same location. As mentioned before, in the IBM there are two coordinate systems, an Eulerian mesh for the fluid, which is a stationary and regular mesh; and a Lagrangian mesh for the boundary. The information between both coordinate systems is communicated via interpolation techniques and is based on two principles: the no-slip condition and the third Newton's law (action = reaction). The discretized IBM equations are then:

$$\mathbf{U_B}^l(\mathbf{X_B}^l, t) = \sum_{x,y} \mathbf{u^{noF}}(\mathbf{x}, t) D(\mathbf{x} - \mathbf{X_B}^l) h^2 \tag{5.34}$$

$$\mathbf{f}(\mathbf{x}, t) = \sum_l \mathbf{F_B}^l(\mathbf{X_B}^l, t) D(\mathbf{x} - \mathbf{X_B}^l) h \Delta s \tag{5.35}$$

where the positions of the Lagrangian coordinates are $\mathbf{X_B}^l$ ($l = 1, 2, 3...m$). Δs is the arc length of the Lagrangian boundary element and $\mathbf{U_B}^l$ and $\mathbf{F_B}^l$ are, respectively, the boundary velocity and the forces acting on the boundary. $D(\mathbf{x} - \mathbf{X_B}^l)$ is a discretized version of the

Dirac delta distribution interpolation function which is also called interpolation kernel. In the present work a 2 point Dirac delta function proposed by Peskin (1977) is used, which gives:

$$D(\mathbf{x} - \mathbf{X_B}^l) = \frac{1}{h^2}\delta\left(\frac{x - X_B^l}{h}\right)\delta\left(\frac{y - Y_B^l}{h}\right) \tag{5.36}$$

where $\delta(r)$ is given by:

$$\delta(r) = \begin{cases} 1 - |r| & |r| \geq 1 \\ 0 & |r| > 1 \end{cases} \tag{5.37}$$

Equation 5.34 means that the boundary velocity matches the ambient fluid velocity and, since the fluid velocity is only known at Eulerian grid nodes $(\mathbf{x})$, it has to be interpolated to arbitrary Lagrangian points $(\mathbf{X_B})$. Equation 5.35 reflects Newton's third law and states that all forces acting on the boundary also have to act on the ambient fluid in order to ensure total momentum conservation. Figure 5.6 schematically shows the range of velocity interpolation used for a 2 point Dirac delta function.
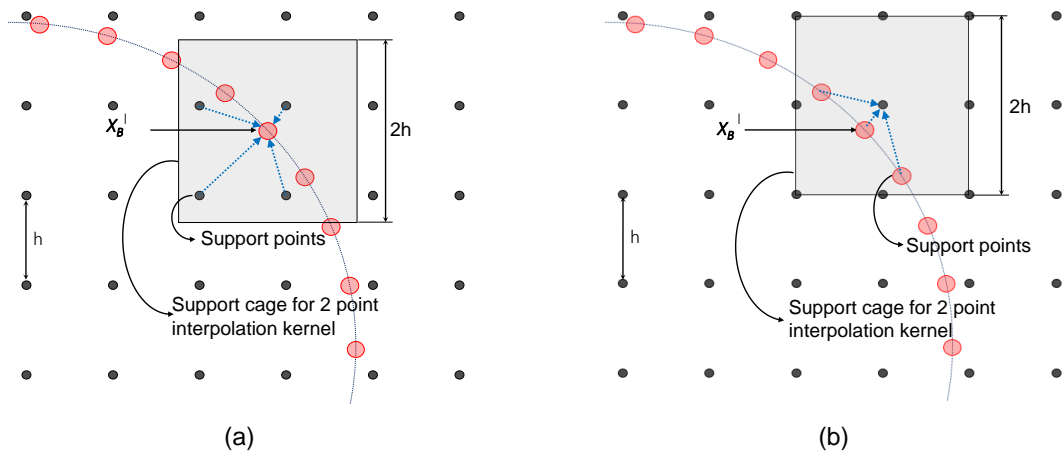
Figure 5.6 – Velocity interpolation scheme. (a) The velocity of Eulerian nodes within the support cage (the Eulerian support points) are interpolated to the central Lagrangean node. (b) The velocity of Lagrangian nodes $\mathbf{X_B}$ within the support cage are interpolated to the lattice node.

In most cases the desired boundary velocity $\mathbf{U_B}^l$ in Eq. 5.34 is known. It can be equal to zero for stationary boundaries or equal a value calculated using Newton's law of motion for a moving boundary (see section 5.6). Furthermore, in order to satisfy the exact no-slip boundary condition, the interpolated Eulerian velocity field, which is the right-hand side of Eq. 5.34, must match $\mathbf{U_B}^l$. However, due to the nature of IBM, this condition may not be achieved since the immersed boundary is defined on a moving Lagrangian mesh whereas the flow field is defined on a stationary Eulerian mesh, and, as already stressed out, the

node points do not necessarily match. This may create a difference between the left-hand side and right-hand sides of Eq. 5.34 and the amount of deviation must be accounted for in order to satisfy the no-slip boundary condition.

Following Dash (2014), a single Lagrangian velocity correction term $\Delta \mathbf{U_B}^l(\mathbf{X_B}^l, t)$ is added to Eq. 5.34 and the required correction is given by:

$$\Delta \mathbf{U_B}^l(\mathbf{X_B}^l, t) = \mathbf{U_B}^l(\mathbf{X_B}^l, t) - \sum_{x,y}^{N_{sE}} \mathbf{u}(\mathbf{x}, t) D(\mathbf{x} - \mathbf{X_B}^l) h^2 \qquad (5.38)$$

where N_{sE} represents the number of Eulerian nodes within the support cage shown in Fig.5.6.

To ensure the no-slip boundary correction at all boundary nodes a sub-interaction scheme is necessary. This is done by interpolating Eulerian velocities back to Lagrangian boundary nodes, and then a new boundary correction $\Delta \mathbf{U_B}^l(\mathbf{X_B}^l, t)$ is calculated. The process is continued until the calculated boundary correction achieves a convergence criteria, which means that $\Delta \mathbf{U_B}^l(\mathbf{X_B}^l, t)$ is insignificant and the no-slip boundary condition was satisfied. In the present work, the convergence criteria for no-slip boundary condition to be considered satisfactory was 10^{-6} as used by Dash (2014).

After calculating the velocity corrections, the force density at Lagrangian and Eulerian nodes are respectively given by:

$$\mathbf{F_B}^l(\mathbf{X_B}^l, t) = \frac{\sum_i 2\rho \Delta \mathbf{U_B}^l(\mathbf{X_B}^l, t)^i}{\Delta t} \qquad (5.39)$$

$$\mathbf{f}(\mathbf{x}, t) = \frac{\sum_i 2\rho \Delta \mathbf{u}(\mathbf{x}, t)^i}{\Delta t} \qquad (5.40)$$

where i is the sub-interaction number.

5.6 Extension of IB-LBM to moving boundary problems

To compute the movement of a particle, the motion equations have to be considered. The Newton's translational Equation of motion is given by:

$$M_s \frac{d\mathbf{U_c}}{dt} = -\int_s \boldsymbol{\sigma} \cdot d\mathbf{S} + (\rho_p - \rho_f) V_s \mathbf{g} \qquad (5.41)$$

where $\boldsymbol{\sigma}$ is the viscous stress tensor, M_s the particle mass, S the particle surface, V the particle volume, $\mathbf{U_c}$ the particle velocity evaluated at its centroid, ρ is the density. The subscript s and f indicate the solid and fluid, respectively.

The angular Equation of motion is given by:

$$I_s \frac{d\boldsymbol{\omega}_c}{dt} = -\int_s (\mathbf{X_B} - \mathbf{X}_c) \times \boldsymbol{\sigma} \cdot d\mathbf{S} \tag{5.42}$$

where I_s is the particle moment of inertia, $\boldsymbol{\omega}_c$ is the angular velocity of the particle, $\mathbf{X_B}$ and $\mathbf{X}_c$ are respectively the position vectors of particle surface (boundary nodes positions) and the particle center.

The second term in the right-hand side of Eq. 5.41 is the buoyancy force acting on the particle whereas the first term is the fluid force acting on the particle, here given by the boundary force (Eq. 5.39) and an added mass force due to particle acceleration, which gives:

$$-\int_s \boldsymbol{\sigma} \cdot d\mathbf{S} = -\int_V \mathbf{F_B} dV + \frac{\partial}{\partial t} \int_V \rho_f \mathbf{u} dV = -\int_V \mathbf{F_B} dV + M_f \frac{d\mathbf{U_c}}{dt} \tag{5.43}$$

where ρ_f and M_f are respectively the fluid density and mass of the displaced fluid.

The right-hand side of Eq. 5.42 is the total torque applied on the particle by the fluid which is computed from the boundary force $\mathbf{F_B}$ and an added mass torque due to angular acceleration, which results in:

$$
\begin{aligned}
-\int_s (\mathbf{X_B} - \mathbf{X}_c) \times \boldsymbol{\sigma} \cdot d\mathbf{S} &= -\int_V (\mathbf{X_B} - \mathbf{X}_c) \times \mathbf{F_B} dV + \frac{\partial}{\partial t} \int_V (\mathbf{X_B} - \mathbf{X}_c) \times \rho_f \mathbf{u} dV \\
&= -\int_V (\mathbf{X_B} - \mathbf{X}_c) \times \mathbf{F_B} dV + I_f \frac{\partial \boldsymbol{\omega}_c}{\partial t}
\end{aligned}
\tag{5.44}
$$

where I_f is moment of inertia of the displaced fluid.

Thus, Eqs. 5.41 and 5.42 can be rewritten as:

$$M_s \frac{d\mathbf{U_c}}{dt} = -\int_V \mathbf{F_B} dV + M_f \frac{d\mathbf{U_c}}{dt} + (\rho_p - \rho_f)V_s \mathbf{g} \tag{5.45}$$

$$I_s \frac{d\boldsymbol{\omega}_c}{dt} = -\int_V (\mathbf{X_B} - \mathbf{X}_c) \times \mathbf{F_B} dV + I_f \frac{\partial \boldsymbol{\omega}_c}{dt} \tag{5.46}$$

Hence, the discretized Newton's equations of motion are given by (KANG, 2010):

$$\mathbf{U_c}^{t+1} = \mathbf{U_c}^t + \frac{1}{M_s}\left[-\sum_l \mathbf{F_B}^l h\Delta s + (M_s - M_f)\mathbf{g}\right]\Delta t + \frac{M_f}{M_s}(\mathbf{U_c}^t - \mathbf{U_c}^{t-1}) \tag{5.47}$$

$$\boldsymbol{\omega}_c^{t+1} = \boldsymbol{\omega}_c^t + \frac{1}{I_s}\left[-\sum_l (\mathbf{X_B} - \mathbf{X}_c) \times \mathbf{F_B}^l h\Delta s\right]\Delta t + \frac{I_f}{I_s}(\boldsymbol{\omega}_c^t - \boldsymbol{\omega}_c^{i-t}) \tag{5.48}$$

The particle center position at $t + \Delta t$ time step can be expressed as (KANG, 2010):

$$\mathbf{X}_c^{t+1} = \mathbf{X}_c^t + 0.5\left(\mathbf{U_c}^{t+1} + \mathbf{U_c}^t\right)\Delta t \tag{5.49}$$

and the particle orientation is updated using the 2D rotation matrix, where the boundary nodes $\mathbf{X_B}^l$ at time step $t + \Delta t$ change according to (ESHGHINEJADFARD et al., 2016):

$$\mathbf{X_B}^{l(t+1)} = \mathbf{X}_c^{t+1} + \mathbf{R}(\theta(t+1))\left(\mathbf{X_B}^{l(t)} - \mathbf{X}_c^t\right) \tag{5.50}$$

where $\mathbf{R}$ is the rotation matrix given by:

$$\mathbf{R}(\theta) = \begin{pmatrix} \cos\theta & -\sin\theta \\ \sin\theta & \cos\theta \end{pmatrix} \tag{5.51}$$

Thus, the boundary velocity at node $\mathbf{X_B}^l$ at the next time step can be evaluated as:

$$\mathbf{U_B}^{l(t+1)} = \mathbf{U}_c^{t+1} + \boldsymbol{\omega}_c^{t+1} \times (\mathbf{X_B}^{l(t+1)} - \mathbf{X}_c^{t+1}) \tag{5.52}$$

The complete numerical algorithm is summarized in the flowchart showed in Fig. 5.7.

5.7 Non-Newtonian approach

Unlike the Newtonian behavior, the viscosity of a non-Newtonian fluid varies with the local strain rate. To implement the shear-rate-dependent effect of non-Newtonian fluids into the LBM, an adaptive viscosity method is applied. The macroscopic fluid viscosity and
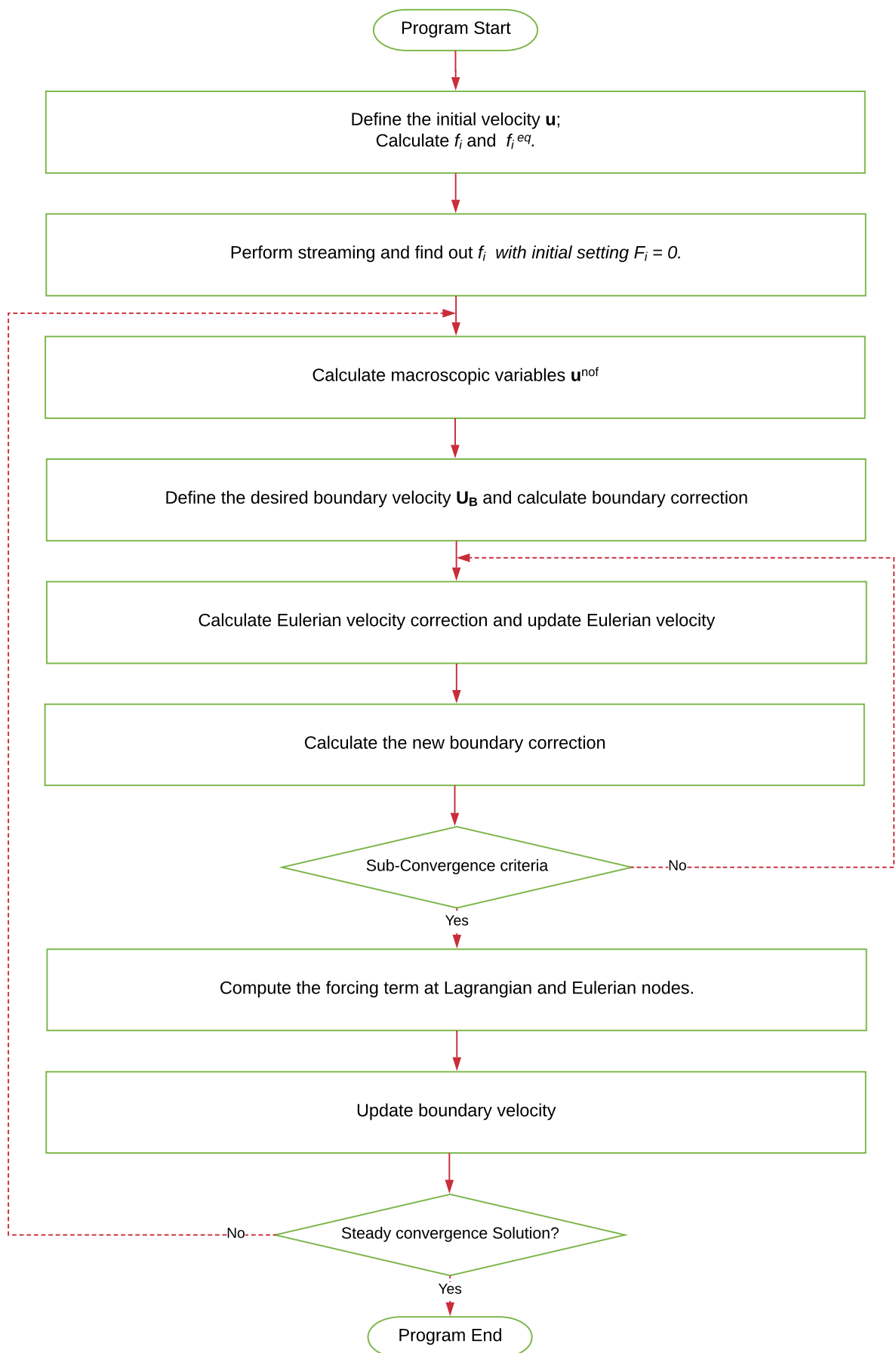
Figure 5.7 – Immersed Boundary - Lattice Boltzmann Method algorithm.

microscopic relaxation time are related in Eq. 5.26. This equation can be rewritten in lattice units as:

$$\tau(\mathbf{x}, t) = 3\nu_l(\mathbf{x}, t) + 0.5 \tag{5.53}$$

where ν_l is the apparent viscosity in lattice units ($\nu_l = \nu \Delta t^{2-n}/\Delta x^2$) and $\tau = \lambda/\Delta t$. The complete translation from physical to lattice Boltzmann units is shown in Appendix B.

Since the apparent viscosity is determined, the instantaneous and local relaxation times (τ) for all lattices can be also determined. The apparent viscosity depends on the shear rate, which in turn can be obtained from the second invariant of the rate-of-strain tensor through the expression (BIRD et al., 1977):

$$\dot{\gamma} = \sqrt{2D_{II}} \tag{5.54}$$

where D_{II} is defined as:

$$D_{II} = \sum_{\alpha, \beta = 1}^{l} S_{\alpha\beta} S_{\alpha\beta} \tag{5.55}$$

and $S_{\alpha\beta}$ is the rate-of-strain defined as:

$$S_{\alpha\beta} = \frac{1}{2} \left(\frac{\partial u_\beta}{\partial x_\alpha} + \frac{\partial u_\alpha}{\partial x_\beta} \right) \tag{5.56}$$

at the incompressible limit the above equation can be expressed as (WANG; HO, 2011):

$$S_{\alpha\beta} = -\frac{1}{2\lambda c_s^2} \sum_{i=0}^{8} c_{i\alpha} c_{i\beta} f_i^{neq} \tag{5.57}$$

where f_i^{neq} is the non-equilibrium distribution function ($f_i^{neq} = f_i - f_i^{eq}$).

This approach is straightforward and of easy numerical implementation, for this reason it is used in the present work.

5.8 Boundary conditions

The incorporation of boundary conditions in LBM consists in translate macroscopic information into the microscopic distribution functions. Different ways of doing this translation

can be found in the literature and the ones used in this work are discussed in this section. The boundary conditions applied for verefication cases are also presented here.

5.8.1   Bounce-back

The Bounce-back condition is widely used to implement no-slip condition. This is done, as its name suggests, by reflecting back, along with its incoming direction, the fluid particles (velocity distribution functions) that reached the boundary. In literature a few variants of this approach can be found and the most broadly used are presented here. They are the on-grid and the mid-grid bounce-back conditions (SUCCI, 2001).

In the on-grid method, the solid boundary is placed over the lattice node, as shown in Fig. 5.8a. In this configuration the incoming particle distribution function that streamed from inside to outside the domain are simply bounced back into the flow domain after the streaming processes, replacing the unknown distribution functions (MOHAMAD, 2011). This reflection process is exemplified below in Fig. 5.9.
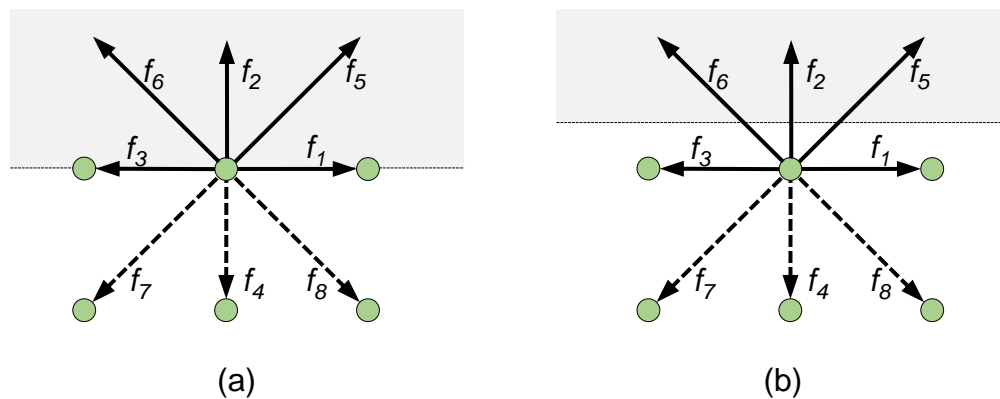
Figure 5.8 – Schemtic representation of (a) on-grid bounce back method and (b) mid-grid method applied at the north boundary. Unknown velocity distribution are represented by dashed lines.
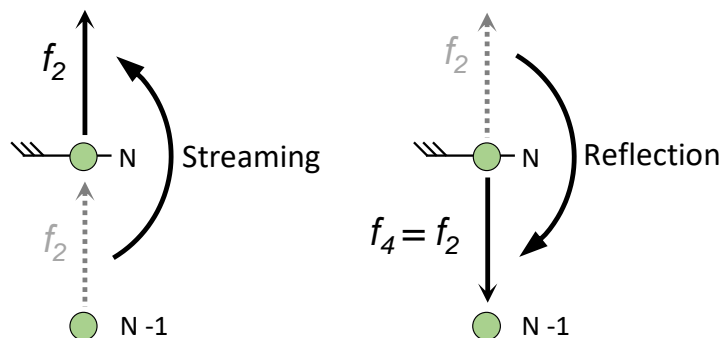
Figure 5.9 – Bounce-back procedure for on-grid implementation.

In the mid-grid approach the solid boundary is placed in the mid-way between solid and fluid domain, as exemplified in Fig. 5.8b. In this specific configuration, particles are

considered to travel only half of the distance (see Fig. 5.10), thus, the particle reflection process takes place during the streaming step as shown in Fig. 5.10. This approach is also known as half-way bounce-back.
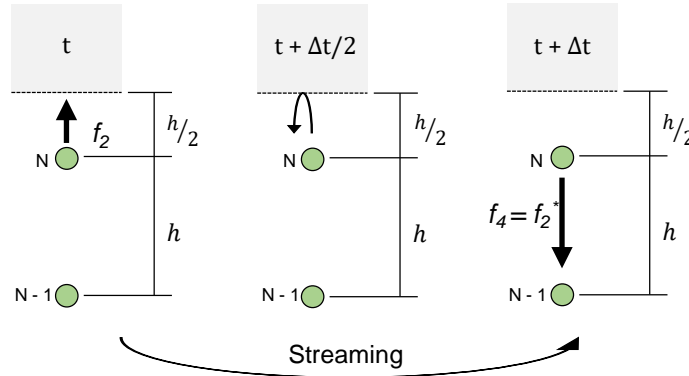
Figure 5.10 – Bounce-back procedure for mid-grid implementation.

Although the on-grid bounce-back is of very simple numerical implementation, it has been verified that it is only first-order accurate (KRÜGER et al., 2017). For this reason the mid-grid is used in the present work.

5.8.2 Zou-He Velocity and Pressure

To perform verification tests in this work, it is necessary to impose velocity and pressure boundary conditions for some cases. These conditions were originally developed by Zou and He (1997). Their idea was to formulate a linear system composed by the unknown velocity distribution functions and the unknown macroscopic quantity (which is pressure when a velocity profile is prescribed at the boundary and it is the velocity when pressure is prescribed) using Eqs. 5.24 and 5.25 . In order to solve this linear system, composed by four unknown quantities and only three equations, Zou and He (1997) assumed, based on the symmetrical nature of the pressure tensor, that the bounce-back rule still holds for the non-equilibrium part of the particle distribution normal to the boundary. Thus, the fourth equation is:

$$f_{-i}^{neq} = f_{-i} - f_{-i}^{eq} = f_i - f_i^{eq} = f_i^{neq} \tag{5.58}$$

For illustration, consider that a general velocity profile $\mathbf{u} = (u, v)$ is given on the left boundary, as shown in Fig. 5.11.

After streaming f_1, f_5, f_8 and ρ are left unknown. Applying Eqs. 5.24, 5.25 and 5.58 gives:

$$f_1 + f_5 + f_8 = \rho - (f_0 + f_2 + f_4 + f_3 + f_6 + f_7) \tag{5.59}$$
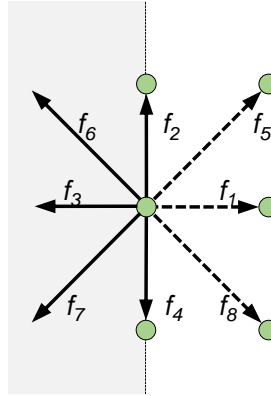
Figure 5.11 – West boundary. Unknown velocity distribution represented by dashed lines.

$$f_1 + f_5 + f_8 = \rho u + (f_3 + f_6 + f_7) \tag{5.60}$$

$$f_5 - f_8 = \rho v - f_2 + f_4 - f_6 + f_7 \tag{5.61}$$

$$f_1 - f_1^{eq} = f_3 - f_3^{eq} \tag{5.62}$$

Equations 5.59 and 5.60 are combined to give a solution for ρ. Then, with f_1 solved by Eqs. 5.18 and 5.62, f_5, f_8 are subsequently determined. Thus, the solution of the linear system composed by Eqs. 5.59 - 5.62 is given by:

$$\rho = \frac{1}{1-u} \left[(f_0 + f_2 + f_4 + 2(f_3 + f_6 + f_7)) \right] \tag{5.63}$$

$$f_1 = f_3 + \frac{2}{3}\rho u \tag{5.64}$$

$$f_5 = f_7 - \frac{1}{2}(f_2 - f_4) + \frac{1}{6}\rho u + \frac{1}{2}\rho v \tag{5.65}$$

$$f_8 = f_6 + \frac{1}{2}(f_2 - f_4) + \frac{1}{6}\rho u - \frac{1}{2}\rho v \tag{5.66}$$

The velocity boundary condition applied on other boundaries and also the pressure boundary condition can be derived similarly.

5.9 Mesh sensitivity test approach

The mesh sensitivity test adopted in this work was proposed by Meira (2016). The discretization of Boltzmann equation gives rise to three main sources of errors. Spatial and

temporal truncation terms generate errors E_{dx} and E_{dt} that scales with $O.\Delta x^2$ and $O.\Delta t^2$, respectively. There are also simulation errors due compressibility, E_{Ma}, that scales with $O.Ma^2$. A global error is defined as the summation of these three errors:

$$E_g = E_{dx} + E_{dt} + E_{Ma} \tag{5.67}$$

Since $Ma = u/cs$ and $cs = 1/\sqrt{3}\Delta x/\Delta t$ (see sections 5.3.1 and 5.4.1), the relationship between Ma, Δx and Δt is given by:

$$Ma = u\sqrt{3}\frac{\Delta t}{\Delta x} \tag{5.68}$$

Moreover, E_{Ma} scales with $O.Ma^2$, so that $E_{Ma} \propto \Delta t^2/\Delta x^2$ and then:

$$E_{Ma} \propto \frac{E_{\Delta t}}{E_{\Delta x}} \tag{5.69}$$

Equation 5.69 clarifies that a reduction of E_g depends not only on the individual reduction of $E_{\Delta t}$ and $E_{\Delta x}$, but also on the relation between them.

The proposal of Meira (2016) was to first perform a sensitivity test for the temporal mesh, which is done by fixing a value of Δx for which Δt is progressively reduced until the chosen analyzed flow parameter (e.g., velocity profile, drag coefficient, particle velocity) shows small changes with Δt reduction. Since both E_{Ma} and $E_{\Delta t}$ are directly proportional to Δt^2 it can be said that this procedure diminishes compressible and temporal errors so that E_g becomes dependent only on $E_{\Delta x}$, such that $E_g \propto \Delta x^2$.

After that, a sensitivity test for the spatial mesh is performed. This is done by reducing Δx, by increasing the number of lattices, and reducing Δt in the same proportion in order to keep the relation $\Delta t/\Delta x$ constant. This procedure ensures that incompressible effects are still irrelevant and that E_g remains dependent only on $E_{\Delta x}$.

Care must be taken regarding the use of relatively low values of $\Delta t/\Delta x$, since this relation affects the relaxation time τ, which when very close to 0.5 makes the method unstable. The relationship between τ, Δx and Δt is given by equation Eq. 5.53.

5.10   Chapter enclosure

In this chapter, the immersed boundary method coupled with the lattice boltzmann method were presented. The non-Newtonian approach in LBM was introduced and the necessary boundary conditions to solve the verification problems were presented. In addition, the methodology used for the mesh sensitivity test and the algorithm structure used to solve the particle sedimentation problem were presented.

6 Verification problems

Before proceeding to the solution of particle settling in non-Newtonian fluid, it is necessary to ensure that the developed algorithm is capable of solving the proposed problem. Simulations of lid-driven cavity flow were performed to verify the ability of the code to solve problems of fluid dynamics. Flow between parallel plates with Power-law fluid was solved in order to guarantee that the non-Newtonian behavior is correctly reproduced. The numerical accuracy of the proposed IB-LBM algorithm was then evaluated by performing simulations on stationary (laminar flow past cylinder) and moving boundary (freely falling particle) flow problem with Newtonian fluid. All results were compared with those reported in the literature.

6.1 Lid-driven cavity

The lid-driven cavity is a well-known benchmark problem extensively used as validation case for new codes or new solution methods (MARCHI; SUERO; ARAKI, 2009). The problem consists of fluid confined in a two-dimensional square domain of height H with no-slip boundary conditions applied to its sides, with three stationary sides and a moving one, as shown in Fig. 6.1.
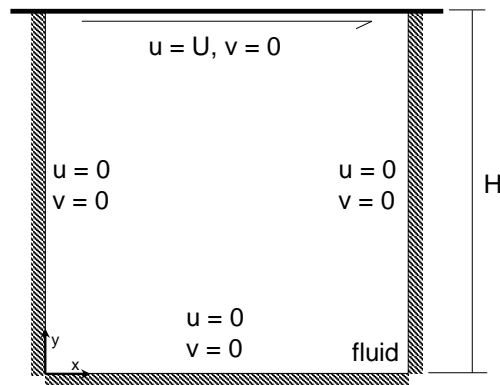
Figure 6.1 – Geometry and boundary conditions for the lid-driven cavity flow problem.

The fluid is Newtonian and the cavity lid moves to the right with a constant velocity U. The only parameter to this problem is the Reynolds number:

$$Re = \frac{UH}{\nu} \tag{6.1}$$

The investigated Reynolds number are $Re = 100, 400$ and 1000. A sensitivity temporal and spacial mesh test were performed considering $Re = 1000$. Following Meira (2016) methodology, it was found that $\tau = 0.547$ and 200 lattices nodes along x and y directions were sufficient to properly solve this problem. The detailed mesh sensitivity test is given in Appendix A.

Figure 6.2 present results in terms of streamlines. It can be easily seen that, the lid movement is responsible for the circular motion of the fluid, furthermore, for $Re = 100$ a main vortex is formed near the top of the cavity and as Re increases the vortex is moved towards the cavity center.

(a)   (b)   (c)
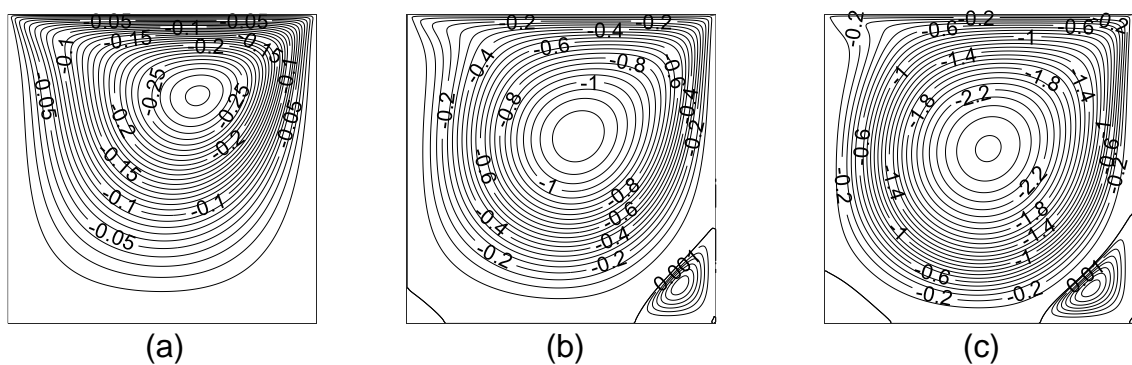
Figure 6.2 – Streamlines for (a) $Re = 100$, (b) $Re = 400$ and (c) $Re = 1000$.

The velocity profiles $u(y)$ and $v(x)$ obtained at the cavity mid-plane for all investigated Re were normalized by the lid velocity U and are presented in Fig. 6.3 and 6.4, respectively. The profiles are in good agreement with those reported by MARCHI et. al. (2009).

The values of U_{min} and V_{min} are shown in Tab. 6.1. The differences between present results and those of Marchi et. al. (2009) are calculated as:

$$Error = \left| \frac{\theta_{ref} - \theta_{calc}}{\theta_{ref}} \right| \times 100 \qquad (6.2)$$

in which θ_{ref} is the reference value and θ_{calc} represents the numerical value obtained in the present work. The greatest $Error$ obtained was 0.89%, which shows a great agreement of the results obtained with those available in the literature.

Table 6.1 – Results for U_{min} and V_{min}

Re	U_{min}			V_{min}		
	Marchi et al (2009)	Present (2018)	Error %	Marchi et al (2009)	Present (2018)	Error %
100	-0.21404	-0.21348	0.262 %	-0.253804	0.251545	0.890 %
400	-0.32872	-0.32880	0.024 %	-0.454058	-0.45323	0.182 %
1000	-0.38857	-0.38903	0.119 %	-0.527056	-0.52706	0.110%
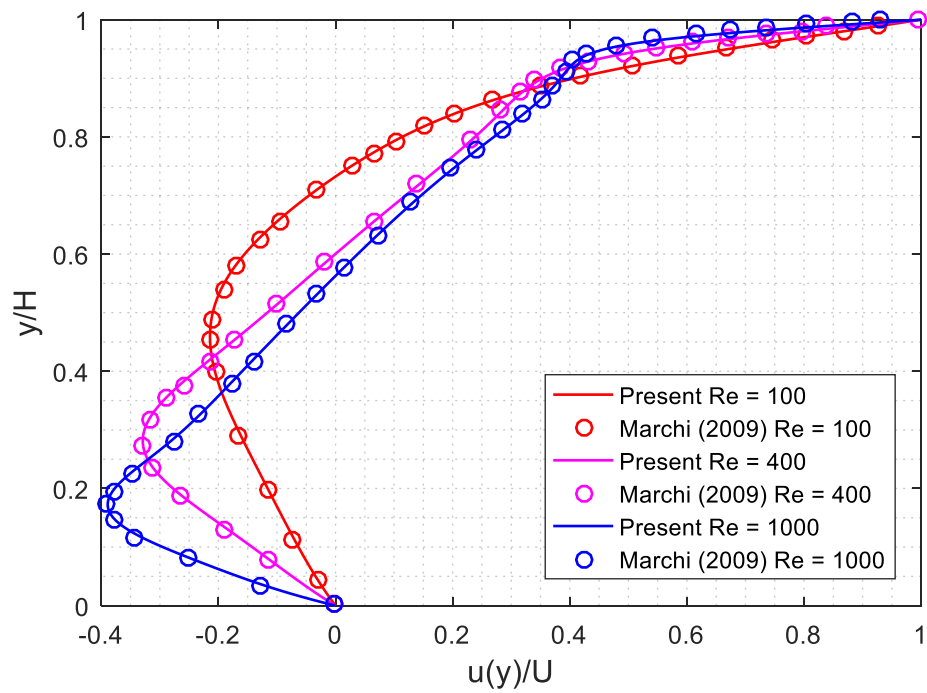
Figure 6.3 – U dimensionless velocity profile at $x = H/2$.
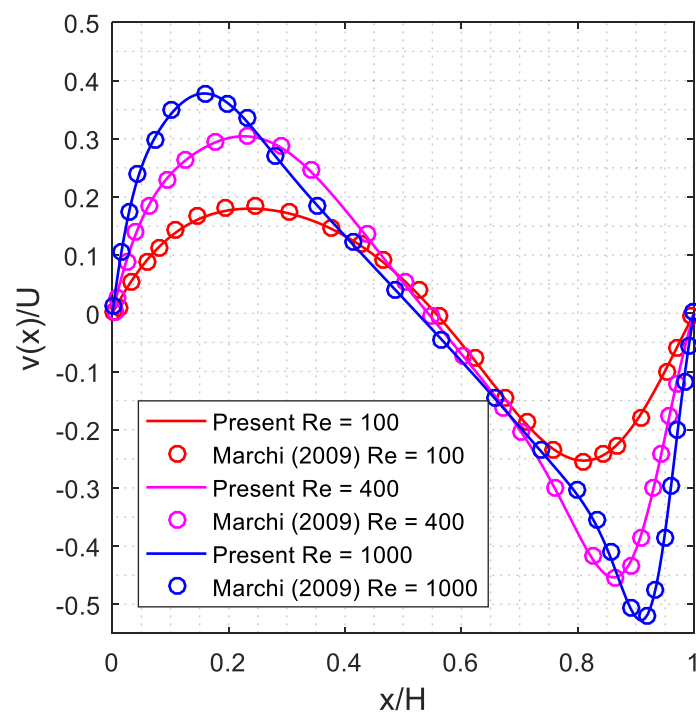
Figure 6.4 – V dimensionless velocity profile at $y = H/2$.

The lid-driven cavity simulations show that the main algorithm feature, which consists of the collision and streaming processes, is implemented correctly which prove the ability of the developed LBM code to solve the present problem of fluid dynamics.

6.2   Power-Law fluid flow between parallel plane plates

In this section the algorithm developed for treatment of non-Newtonian fluids using LBM is verified. For this purpose Power-law flow between parallel plates is considered. This geometry was chosen due the similarity of boundary conditions applied to solve the flow past over a circular particle.Thus, the simulations in this section is also used to verify the boundary conditions imposed at the channel inlet and outlet.

The geometry and boundary conditions used to study this problem are shown in Fig. 6.5.
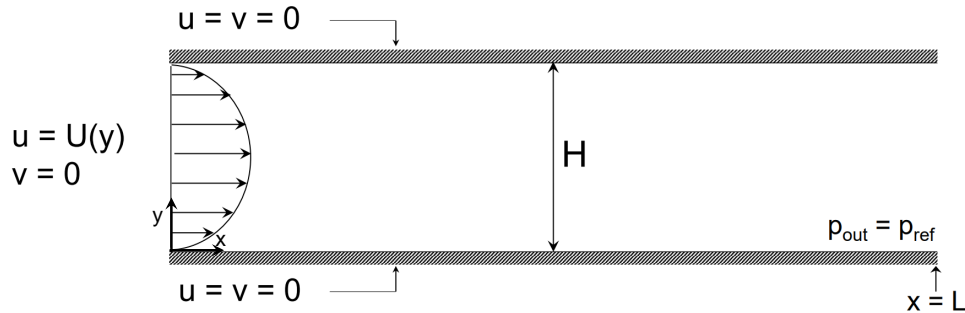
Figure 6.5 – Geometry and boundary conditions of Power-law fluid flow between flat and parallel plates.

Results obtained in this section are compared with the fully developed velocity profile for laminar flow of Power-law fluids in a channel of height H (BHARTI; CHHABRA; ESWARAN, 2007):

$$U_{ana}(y) = U_{max}\left[1 - \left(\left|1 - \frac{2y}{H}\right|\right)^{\frac{(n+1)}{n}}\right] \tag{6.3}$$

where U_{max} is the maximum velocity, which is related to the average velocity, U_{avg}, as:

$$U_{max} = \left(\frac{2n+1}{n+1}\right)U_{avg} \tag{6.4}$$

and the average velocity U_{avg} is determined from a desired modified Reynolds number, Re_{pl} is defined as (BHARTI; CHHABRA; ESWARAN, 2007):

$$Re_{pl} = \frac{U_{avg}^{2-n}H^n}{m} \tag{6.5}$$

In this study two parallel plates were kept apart at a distance H forming a channel. A completely developed velocity profile is imposed on the channel inlet, then disregarding the development length, while on the walls the no-slip condition is considered. The channel length was chosen to be $L = 5 \times H$. The fluid has density $\rho = 1000 kg/m^3$ and a consistency index, $m = 0.1$. Numerical simulations were performed for $Re_{pl} = 1$ and $n = 0.25$, 0.6, 1.0 and 1.4. A sensitivity temporal and spacial mesh test was performed for $n = 0.25$, which results are presented and discussed in Appendix A. The number of lattice nodes used across the channel height in simulations was $N = 160$.

Figure 6.6 shows the numerical and analytical velocity profiles at the channel outlet, and it can be observed that the agreement between results is satisfactory. The maximum percentage error, Ep, between the analytical and numerical solutions is less than 0.4% and occurs for $n = 0.25$, where Ep is defined as:

$$Ep = \frac{\sum_y \frac{U(y) - U_{ana}(y)}{U_{ana}(y)} 100}{H} \qquad (6.6)$$
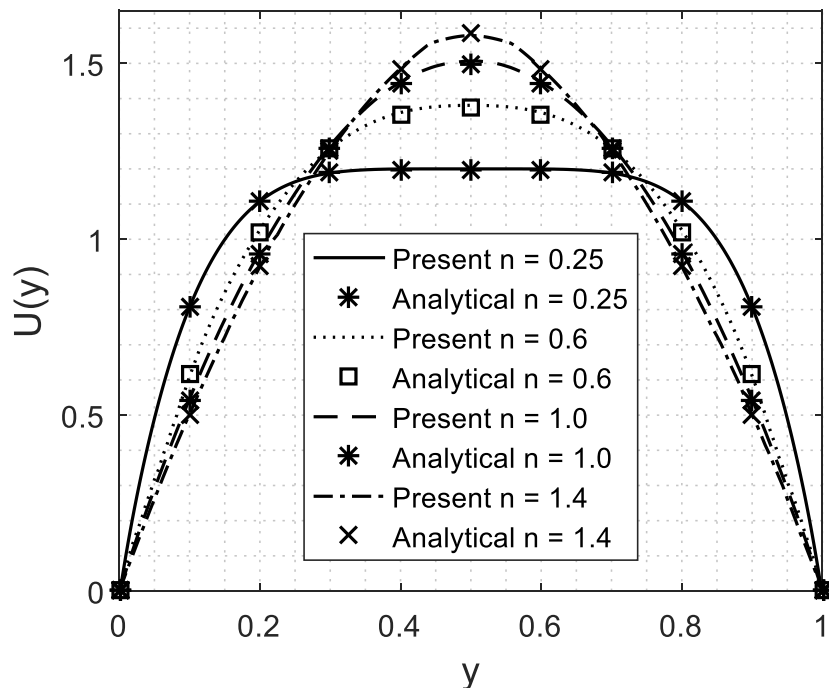
Figure 6.6 – Results for numerical velocity profile at the channel outlet represented by the solid lines compared with analytical solutions for different values of n.

6.3   Newtonian flow past over a circular cylinder

To verify the Immersed boundary method implementation, the laminar flow of a free-stream past over a stationary circular cylinder is simulated. In this case, a 2D cylinder of diameter d is positioned at the centre of a domain of $40d \times 40d$, which is the same geometry used by Kang (2010) and Dash (2014) and is shown in Fig. 6.7.
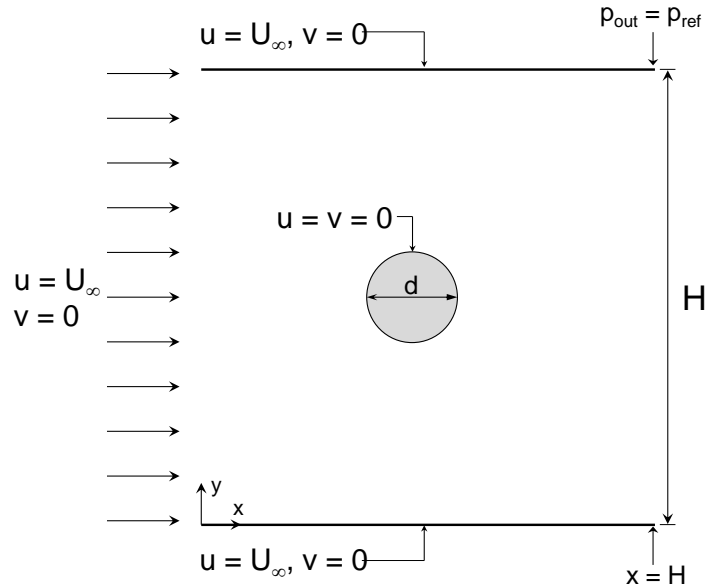
Figure 6.7 – Geometry and boundary conditions for flow past over a circular cylinder.

In this problem, the flow pattern changes according to the Reynolds number (BRAZA; CHASSAING; MINH, 1986), which is defined as:

$$Re = \frac{U_\infty d}{\nu} \tag{6.7}$$

where U_∞ is the free-stream velocity and d is the diameter of the cylinder.

According to the literature, at a low Reynolds number, the flow around the cylinder is steady and a pair of vortices are symmetrically generated about the centerline of the cylinder (KANG, 2010). As Re increases the flow pattern changes, the vortices at the cylinder rear increase and at a critical Re ($Re > 40$ (BRAZA; CHASSAING; MINH, 1986)) the flow changes to a unsteady state in which vortex shedding are observed. Both states are considered in this section. For the steady state $Re = 20$ and 40 are investigated while for unsteady state $Re = 100$ is considered. For results, a quantitative comparison of the simulations is done by comparing the drag (C_D) and lift (C_L) coefficients experienced on the cylinder with results

presented in the literature. C_D and C_L are respectively calculated according to Eq. 6.8 and 6.9 (CHHABRA, 2006).

$$C_D = \frac{F_{drag}}{1/2\rho_f U_\infty^2 A_p} \tag{6.8}$$

$$C_L = \frac{F_{lift}}{1/2\rho_f U_\infty^2 A_p} \tag{6.9}$$

where A_p is the projected area and F_{drag} is determined from the x component of the force density at Lagrangian nodes (see section 5.5.1):

$$F_{drag} = -\sum_l^{NL} F_{Bx}^l \Delta s \tag{6.10}$$

where NL is the number of Lagrangian nodes and F_{lift} is determined from the y component:

$$F_{lift} = -\sum_l^{NL} F_{By}^l \Delta s \tag{6.11}$$

6.3.1   Steady flow

At first, a steady state flow around the cylinder is investigated. In order to do that, a sensitivity mesh test was performed for $Re = 40$. The Eulerian and temporal sensitivity mesh tests are again performed according to Meira (2016) and are described in Appendix A. Results were obtained for 20 Eulerian grid points across the cylinder ($d_l = 20h$) and $\tau = 0.575$. The Lagrangian points are uniformly distributed on the cylinder surface with a spacing of $\Delta s = h/1.5$ as recommended by Kang (2010) and it was kept the same for other simulations in which the immersed boundary was applied.

Figure 6.8 shows the streamlines near the cylinder for $Re = 20$ and 40. The symmetric vortices are clearly observed in the wake region and, as expected, the wake length increases with increasing Re. As it can be seen in Figure 6.9 the vorticity, defined as $\vec{\omega} = \nabla \times \vec{v}$, spreads further out laterally as Re increases from 20 to 40.

The drag coefficient and the wake length, which is the length of recirculation region formed behind the cylinder measured from the rearmost point of the cylinder to the end of the wake and divided by d, obtained from the numerical solution are compared with the literature as shown in Tab. 6.2. Results are found in good agreement. The maximal deviation on C_D occurred between the obtained results and those reported by Park, Kwon and Choi (1998). The deviations found are 6.0% for $Re = 20$ and 5.6% for $Re = 40$.
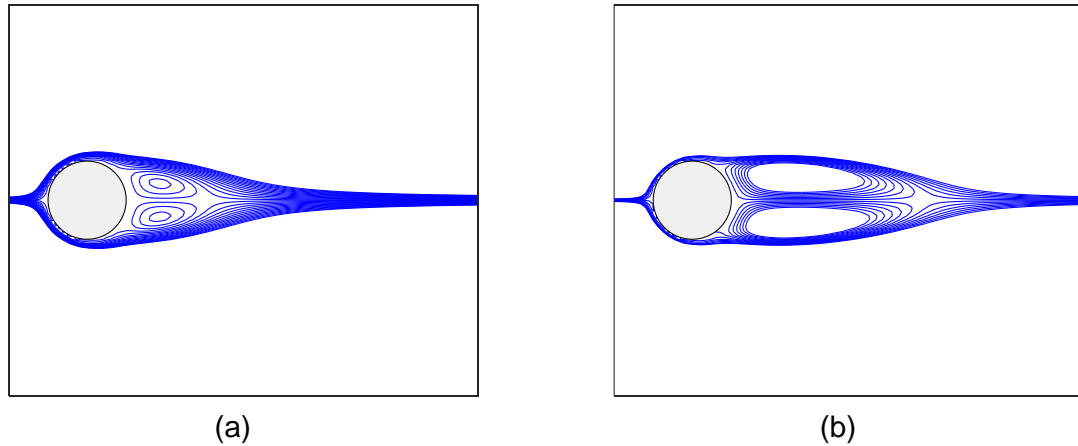
Figure 6.8 – Streamlines near the cylinder for (a) $Re = 20$, $\Delta\Psi = 0.0008$ and (b) $Re = 40$, $\Delta\Psi = 0.0016$.
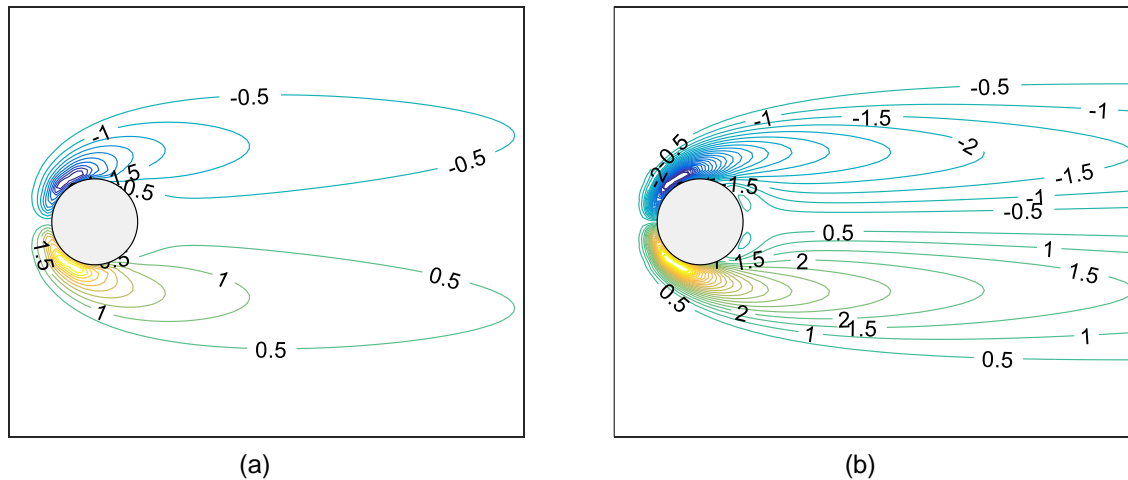
Figure 6.9 – Vorticity contours near the cylinder for (a) $Re = 20$ and (b) $Re = 40$.

6.3.2 Unsteady flow

As Reynolds number becomes higher than 40 the flow becomes unsteady and a loss of symmetry in the wake is observed. Vortices are released from the wake, which are advected and diffused away from the cylinder, forming what is called of Karman vortex streets (BRAZA; CHASSAING; MINH, 1986). The dimensionless frequency of vortex release is given by the

Table 6.2 – Comparison of C_D and recirculation length at steady flow.

Reference	Method	Re 20 C_D	$L = l/d$	Re 40 C_D	$L = l/d$
Park, Kwon and Choi (1998)	Body-fitted grid, NSE	2.010	-	1.510	-
Wu and Shu (2009)	Implicit direct-forcing, LBE	2.091	0.930	1.565	2.31
Kang (2010)	Implicit direct-forcing, LBE	2.075	0.950	1.555	2.34
Dash (2014)	Flexible direct-forcing, LBE	2.119	0.937	1.589	2.32
Present	Flexible direct-forcing, LBE	2.131	0.950	1.594	2.35

Strouhal number (S_t), given by (BRAZA; CHASSAING; MINH, 1986):

$$S_t = \frac{f_q d}{U_\infty} \tag{6.12}$$

where f_q is the vortex shedding frequency, that is obtained from the time evolution of the lift coefficient, shown in Fig. 6.11.
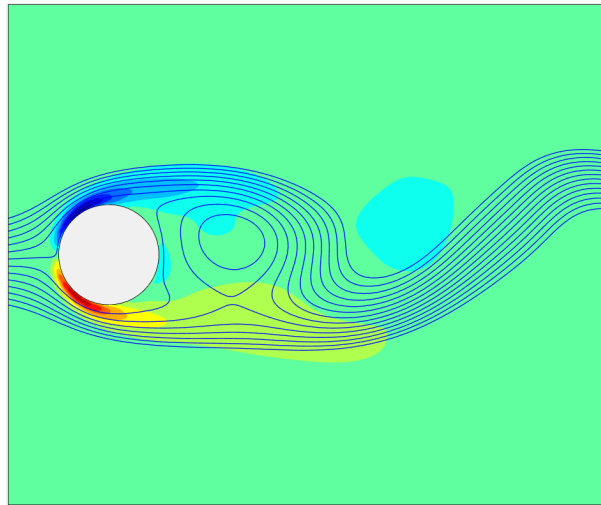
Figure 6.10 – Instantaneous streamlines and vorticity contour near the cylinder at $Re = 100$, $t = 48.75\ s$ and $\Delta\Psi = 0.2$.

Numerical results are presented here for $d_l = 40h$ and $\tau = 0.62$. Details on the mesh sensitivity test are given in Appendix A. The time evolution of lift and drag coefficients are shown in Figs. 6.11 and 6.12, respectively. As can be seen in Fig. 6.11 the flow pattern is severely changed. It can be observed that the flow has vortex shedding in its wake. The lift coefficient oscillates between ± 0.344 while the drag coefficient oscillates around an average value of 1.421. To compare, Tab. 6.3 shows results for C_D, C_L and S_t of different authors.
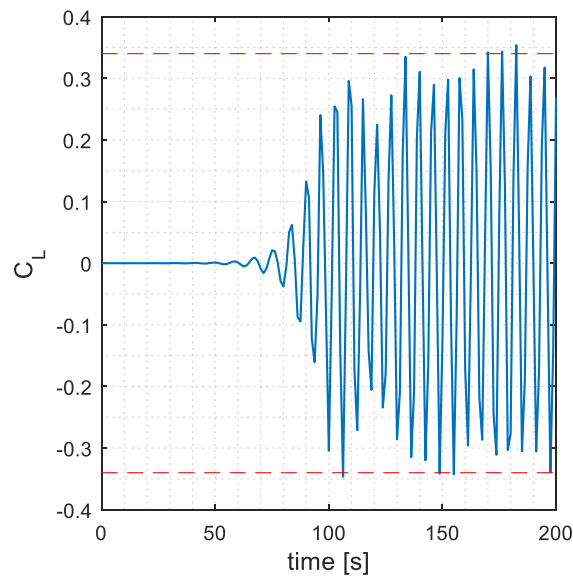
Figure 6.11 – Time evolution of the lift coefficient for $Re = 100$.
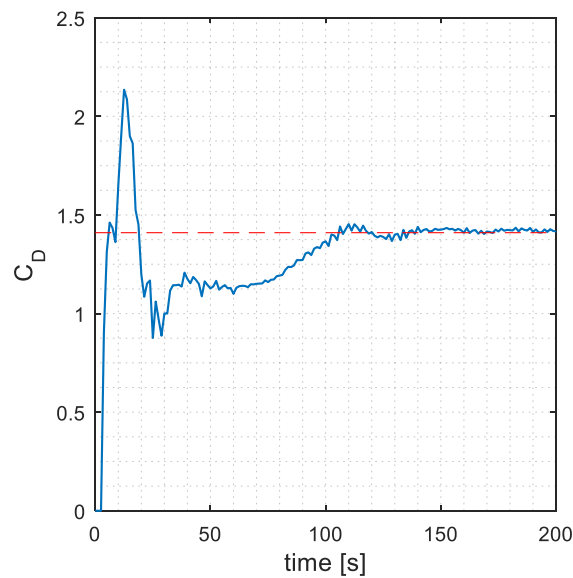
Figure 6.12 – Time evolution of the drag coefficient for $Re = 100$.

These results obtained with the proposed numerical scheme are satisfactory compared with those observed in the literature. The accuracy of the presented results, both steady and unsteady, can be improved by applying a zone of refinement around the cylinder as has been done by (KANG, 2010) and (DASH, 2014) However, such extensive studies are not the main focus of this work, where the capability of the immersed boundary - lattice Boltzmann method for moving boundaries using Power-law fluids is investigated.

At this point the immersed boundary method seems to be a good option when dealing with particles with curved boundary subject to a fluid flow.

Table 6.3 – Comparison of drag and lift coefficients and Strouhal number at Re=100.

Reference	Method	C_D	C_L	S_t
Park, Kwon and Choi (1998)	Body-fitted grid, NSE	1.33	0.33	0.165
Sui et al. (2007)	Explicit direct-forcing, LBE	1.438	0.344	0.166
Wu and Shu (2009)	Implicit direct-forcing, LBE	1.364	0.344	0.163
Kang (2010)	Implicit direct-forcing, LBE	1.368	0.346	0.163
Dash (2014)	Flexible direct-forcing, LBE	1.362	0.341	0.162
Present	Flexible direct-forcing, LBE	1.421	0.344	0.160

6.4   Particle settling in Newtonian fluid

In this section the immersed boundary method is tested for moving boundaries. The same geometry and properties used by Kang (2010) are investigated here. Results for particle settling velocity and trajectory are compared with those available in the literature. The container has $2\ cm$ of lenght and height of $6\ cm$. A circular 2D particle with diameter $d = 0.25\ cm$ has its centre initially located at $(1\ cm, 4\ cm)$, as shown in Fig. 6.13. The fluid density and dynamic viscosity are $\rho_f = 1\ g/cm^3$ and $\mu = 0.1\ g/cm - s$, respectively, and the particle density is $\rho_p = 1.25\ g/cm^3$.
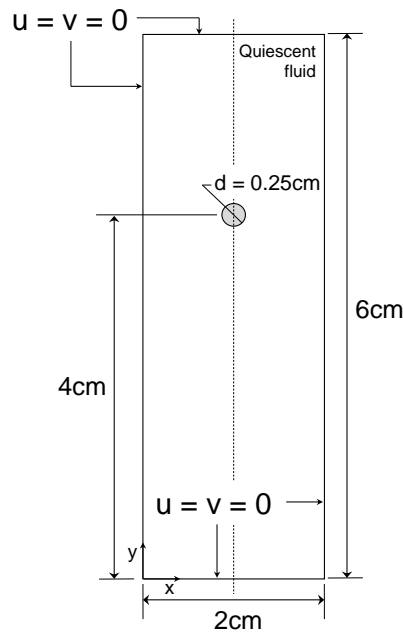
Figure 6.13 – Geometry and boundary conditions for particle settling study.

The fluid and the particle are initially at rest. Once the particle is released from its initial position it starts falling under gravity effect and keeps accelerating until it reaches a steady velocity. The steady velocity is called terminal settling velocity, V_T and happens when the net upward force, comprised of drag and the buoyant forces, is balanced with the weight force.

For this verification problem, the Eulerian, Lagrangian and temporal meshes are the

same as the one applied by Kang (2010), Dash (2014) and Delouei et al. (2016), who studied settling motion using lattice Boltzmann method. The Lagrangian mesh space of $\Delta s = h/1.5$ is applied here. 25 lattices were used across the cylinder diameter, which implies a mesh size of 200×600 lattices. The relaxation time (τ) was equal to 0.65, corresponding to $5 \times 10^{-4}s$ for each time step.

The time evolution of particle settling velocity and position are presented in Figs. 6.14 and 6.15, respectively. Results are in good agreement with those of literature. Vorticity contours are shown in 6.16 at different settling times. The vorticity pattern is in accordance with the vorticity contours presented by Dash (2014), which are reprinted here in Fig. 6.17.
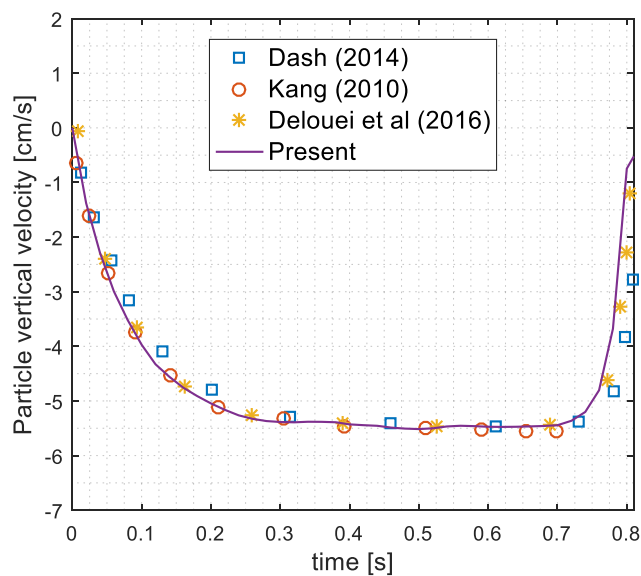
Figure 6.14 – Comparison of temporal evolution of particle settling velocity with literature.
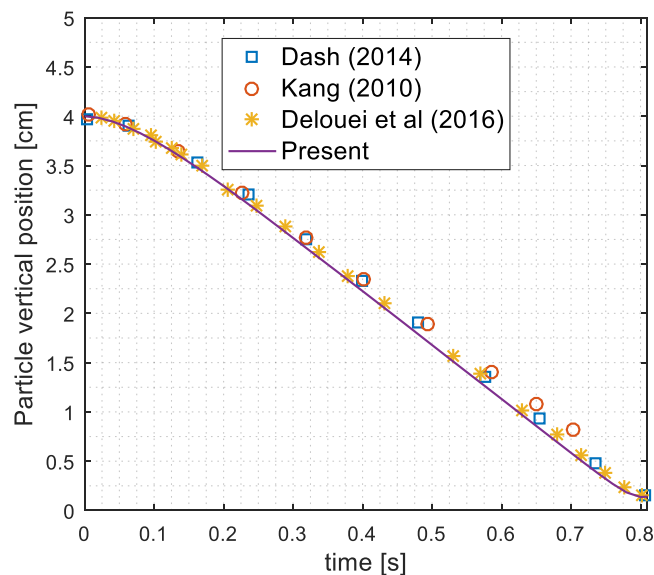
Figure 6.15 – Comparison of temporal evolution of particle vertical position with literature.
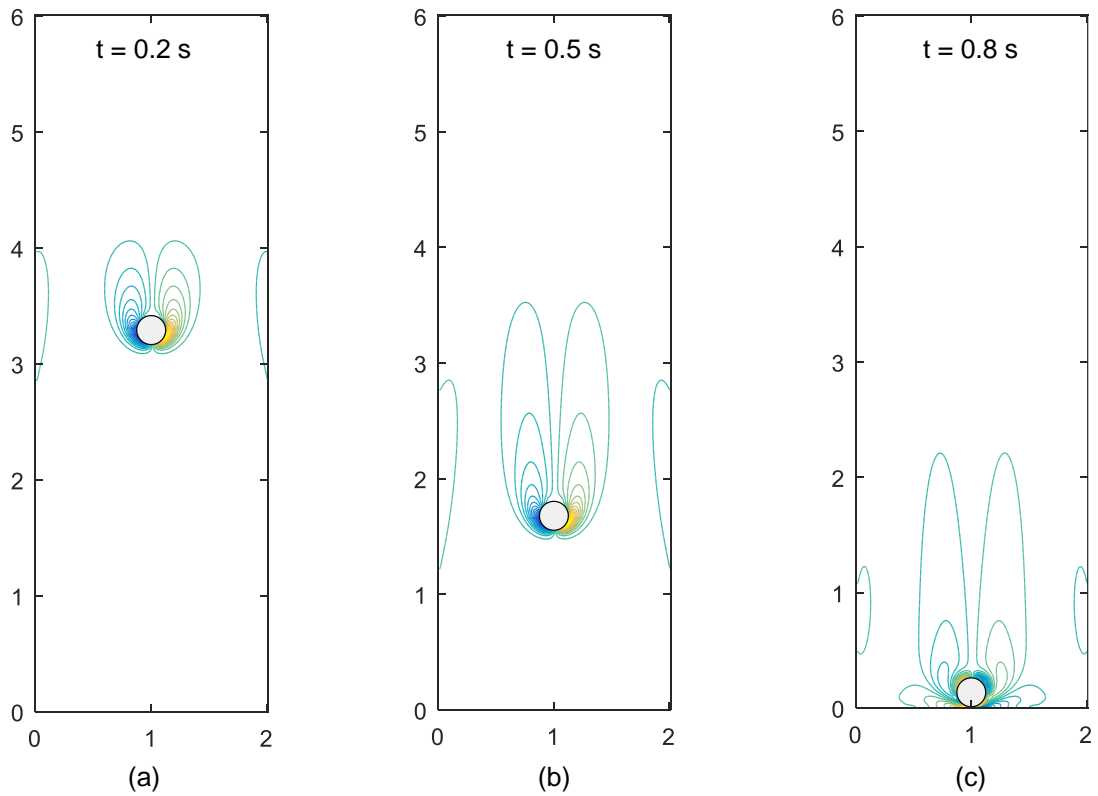
Figure 6.16 – Instantaneous vorticity contours at different settling times. (a) $t = 0.2\ s$, (b) $t = 0.5\ s$ and (c) $t = 0.8\ s$.
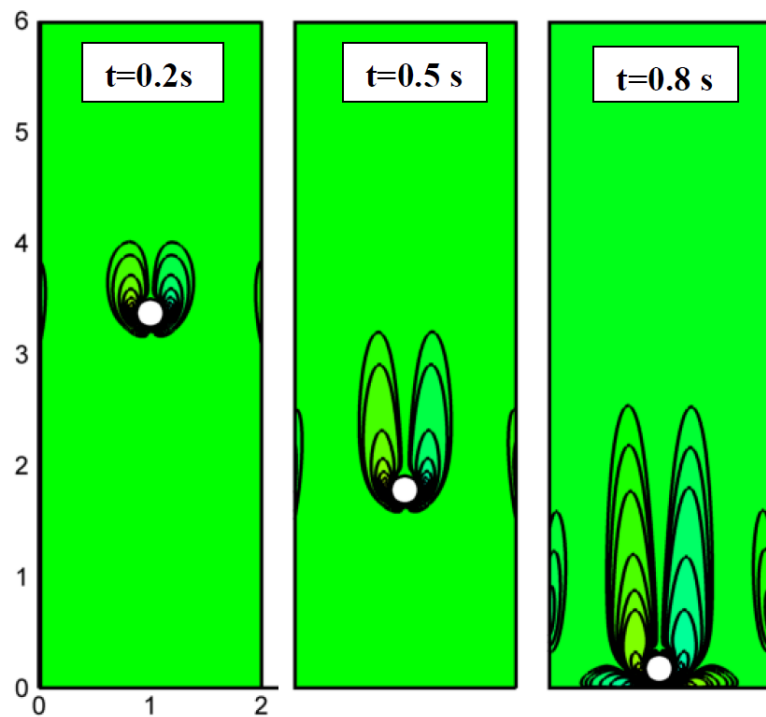
Figure 6.17 – Instantaneous vorticity contours obtained by Dash (2014).

6.5 Particle settling in Power-law fluid

The settling of a 2D particle in Power-law fluid is now investigated. Simulations for Newtonian, shear-thinning and shear-thickening non-Newtonian fluids are compared with results presented by Delouei et al. (2016). To do that, the same geometry used to verify the particle settling in Newtonian medium is applied. The simulations are performed varying the Power-law index n but keeping the same generalized Archimedes number (defined by Eq. 4.22). The particle and fluid properties described in the previously section lead to $Ar_{pl} = 602$ when $n = 1$. By modifying n and keeping Ar_{pl} constant, fluid consistency index m is changed.

In Fig. 6.18, the obtained results for particle settling velocity are compared with the literature for different Power-law index. Results are again in good agreement with the literature.
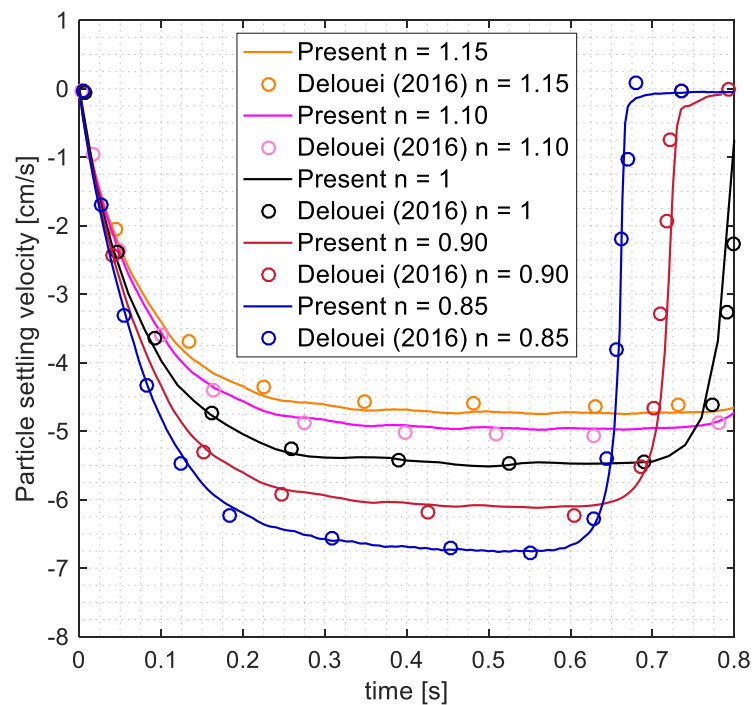
Figure 6.18 – Comparison of temporal evolution of particle settling velocity with literature for different values of n.

6.6 Closing remarks

In this chapter, specific problems were reproduced in order to verify the developed code. The lid driven cavity problem was the starting point for verification of the developed program. Results showed the ability of the program to solve incompressible Newtonian flows. By simulating the Power-law flow between parallel plates the performance of the LBM

adapted for solution of non-Newtonian fluids was verified. Furthermore, to ensure that the code implemented for the immersed boundary - lattice Boltzmann method could adequately solve particle problems with curved surfaces, the flow past over a circular cylinder and the dynamics of particle settling were investigated. Results are in good agreement with the literature for both, moving and stationary boundaries. Finally, simulations of particle sedimentation in Power-law fluids for different values of n were performed. The results obtained are equivalent to the results presented by (DELOUEI et al., 2016) which indicate that the implementation of the code for particle settling in Power-law fluid using the immersed boundary method was successful.

7 Results

This chapter presents the results for the dynamics of particle settling in Power-law fluids. Most of the drilling fluids are non-Newtonian with viscosity decreasing as shear rate increases. This is similar to the behavior of shear-thinning fluids. For instance, the non-Newtonian fluid behavior is characterized by the Power-law model. The fluid and particle properties investigated are presented in Tab. 7.1

Table 7.1 – Investigated parameters

Parameter	Symbol	Range
Power law index	n	0.6, 0.8, 1.0, 1.2, 1.4
Particle diameter [cm]	d	0.0625, 0.125, 0.25
Particle/fluid density	$\rho_r = \rho_p / \rho_f$	1.1, 1.25, 1.5

This chapter is divided in two main parts. At first, a parametric study is performed to verify the individual influences of particle size, Power-law index and particle/fluid density ratio. Also, wall effect is investigated for diferent values of n. Then, the obtained results are written in a generalized form for terminal drag coefficient, $C_{D,T}$, and terminal generalized Reynolds number, $Re_{pl,T}$, as a function of n and the generalized Archimedes number, Ar_{pl}.

7.1 Part 1: Parametric study

7.1.1 Domain height

Before proceeding with the parametric study, the height of the domain must be determined to ensure that terminal settling velocity is perceived before the particle reaches the bottom of the domain. Numerical simulations were performed for the case in which the highest settling velocity was expected: $n = 0.6$, $d = 0.25cm$ and $\rho_r = 1.25$. For this first approach, the Eulerian and temporal meshes were the same of the verification case of particle settling in a Newtonian media. That is, 25 lattice units across the particle diameter and $\tau = 0.65$. The domain height was then gradually increased until the particle terminal velocity did not undergo through any considerable changes. Results for this test are presented in Tab. 7.2. As can be seen, the maximal settling velocity increased with increasing H from $6\ cm$ to $8\ cm$, which means that the particle was not able to reach a terminal velocity when settling in a container with only $6\ cm$ high. However, the maximal settling velocity shows an insignificant increase when H goes from $10\ cm$ to $12\ cm$, which means that at $H = 10\ cm$ the terminal settling velocity was perceived.

Table 7.2 – Maximal particle settling velocity for different domain heights.

H	V	$V_{increase}$
6	-8.177	
8	-8.477	3.67%
10	-8.592	1.35%
12	-8.607	0.18%

After that, a grid dependence test was performed, for details see Appendix A. remaining simulations were performed in in a domain of $H = 10\ cm$, with a time step of $\Delta t = 10^{-4}\ s$ and for a lattice space of $h = 10^{-2}\ cm$.

7.1.2 Settling velocity and particle trajectory as a function of n

For this study d and ρ_r were fixed at 0.0125 cm and 1.25 respectively. The aspect ratio between particle and container walls were the same as in the test case of settling particle in Newtonian fluid, were $L/d = 8$.

Figure 7.1 shows the time evolution of the particle settling velocity and its position. As can be seen, the particle settling velocity considerably increases as the fluid behavior changes from shear-thickening to Newtonian and then to shear-thinning. This shows the impact of non-Newtonian behavior on motion of free fall particles. This can be explained by considering the variation of strain rate close to the immersed boundary (DELOUEI et al., 2016). Since the maximum rate of fluid deformation takes place near the particle, the viscosity of the moving fluid surrounding the particle increases with increasing Power-law index (see Eq. 2.5). This increment in the fluid viscosity leads to a more slow moving particle and consequently the particle takes a longer time to reach the bottom of the container.

The influence of n on the terminal settling velocity, V_T, on the terminal generalized Reynolds number $Re_{pl,T}$, given by Equation 4.19, and on the drag coefficient experienced by the particle at its terminal velocity, $C_{D,T}$, is shown in Tab. 7.3.

The percentage difference observed in the analyzed parameters is computed with Equation 7.1

$$Error = \left| \frac{\theta_n - \theta_{next}}{\theta_n} \right| \times 100 \tag{7.1}$$

where θ_n is the value of the parameter of interest for a given n and θ_{next} is the parameter value at the subsequent value of n. As can be seen in Tab. 7.3, the particle settling is more influenced by the fluid behavior for low values of n, which is perceived by a decrease of the percentage difference observed for the analyzed parameters as n increases.
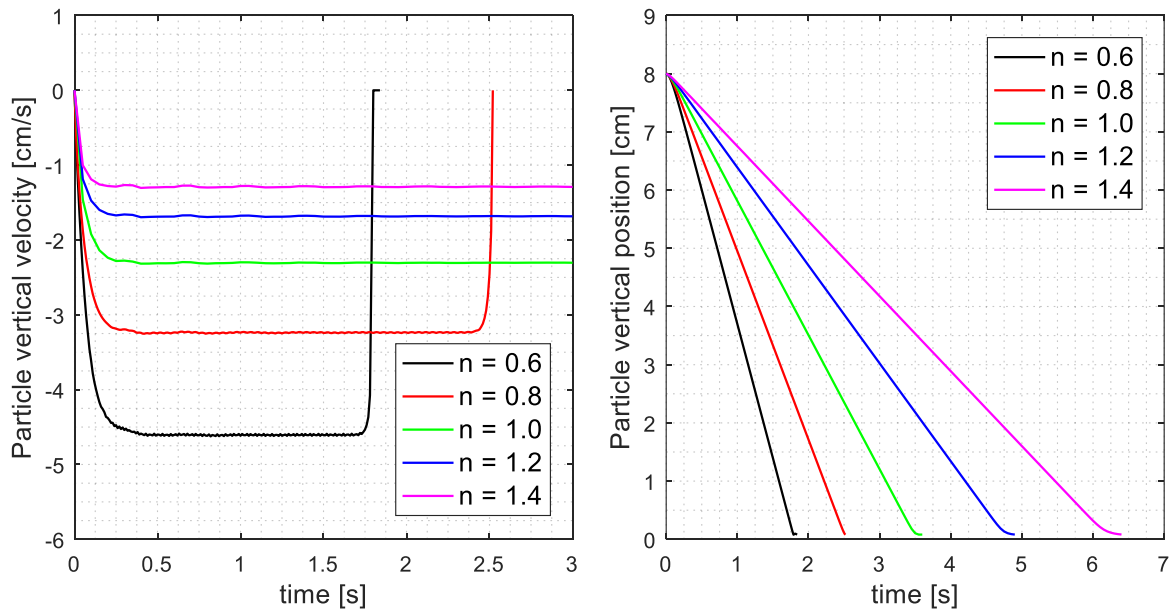
Figure 7.1 – Particle settling velocity and position for different power law index.

Table 7.3 – Influence of n on V_T, $Re_{pl,T}$ and $C_{D,T}$.

n	V_t	V_t decrease	$Re_{pl,T}$	$Re_{pl,T}$ decrease	$C_{D,T}$	$C_{D,T}$ increase
0.6	4.621		24.48		2.20	
0.8	3.248	30%	7.79	68%	4.58	109%
1	2.316	29%	2.90	63%	8.93	95%
1.2	1.693	27%	1.26	57%	16.80	88%
1.4	1.294	24%	0.63	49%	28.75	71%

7.1.3 Particle diameter influence, d

In order to verify the influence of the particle diameter on its terminal settling velocity and avoid the influence of wall container on its motion, the aspect ratio between particle diameter, d, and container walls distance, L, were kept constant ($L/d = 8$), as in the previous simulations. The particle/fluid density ratio (ρ_r) was kept at 1.25.

The simulation results for $Re_{pl,T}$ and $C_{D,T}$ as a function of particle diameter and n are summarized in Figure 7.2. It can be seen that regardless of the value for n the particle terminal Reynolds number increases with increasing d, as expected given the $Re_{pl,T}$ definition. The low velocities given at low Reynolds numbers leads to less drag friction experienced by the particle, which is confirmed by a decrease in $C_{D,T}$ as d increases, shown in Figure 7.2.b. As discussed in the previous section an increase on the shear-thinning behavior causes a significant increase on settling velocity and consequently on $Re_{pl,T}$. This tendency is kept regardless of the particle diameter.
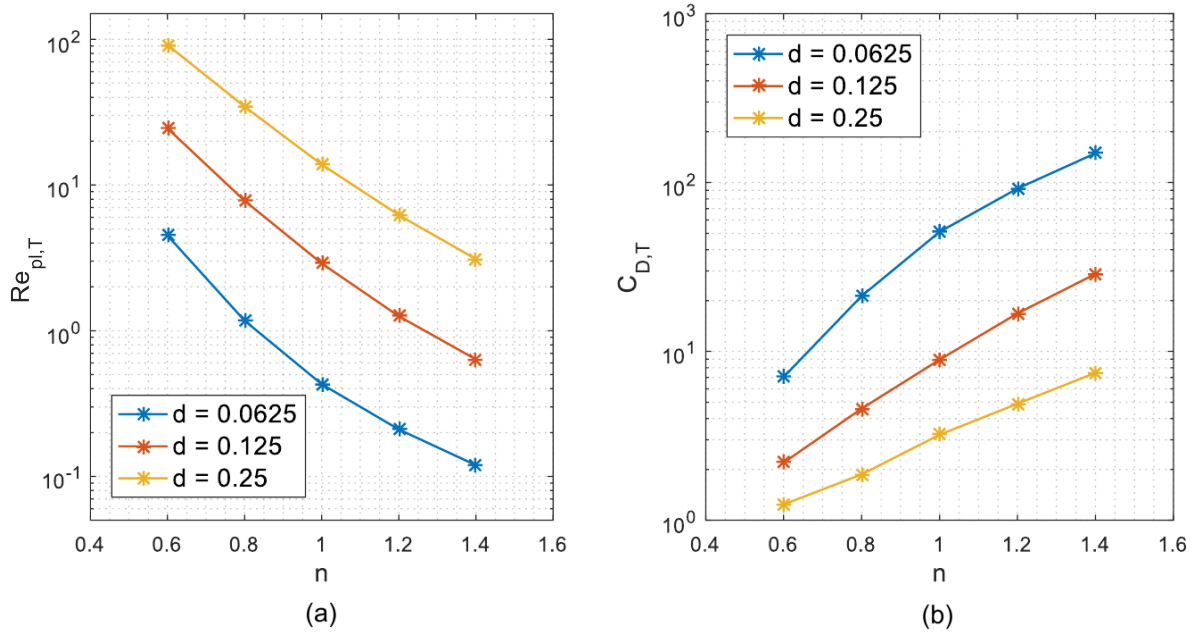
Figure 7.2 – Influence of particle diameter (a) on $Re_{pl,T}$ and (b) on $C_{D,T}$ as a function of n.

7.1.4 Particle/fluid density ratio influence

Settling behavior for different particle densities was examined using an intermediate value for particle diameter, $d = 0.125$ and keeping $L/d = 8$.

Figure 7.3 shows simulation results for $Re_{pl,T}$ and $C_{D,T}$ as a function of ρ_r and n. The curves for $Re_{pl,T}$ indicate that the terminal settling velocity is more affected by ρ_r at low values of n. As the fluid changes from shear-thinning to a shear-thickening behavior, ρ_r has less influence on terminal Reynolds. For $n = 1.4$, $Re_{pl,T}$ increases 98.91% as ρ_r goes from 1.1 to 1.25, while the increase observed for $n = 0.6$ is of 531.56%. The same tendency is observed for $C_{D,T}$. For $n = 1.4$, $C_{D,T}$ decreases 49.58% as ρ_r goes from 1.1 to 1.25, while the decrease observed for $n = 0.6$ is of 64.45%.

7.1.5 Wall effect

When a particle falls confined by finite boundaries, it is subject to a retardation effect due wall effects (UHLHERR; CHHABRA, 1995). In this section the boundary effect is investigated. For this, the particle diameter and particle/fluid density ratio were kept constant, $d = 0.125cm$ and $\rho_r = 1.25g/cm^3$. The Power-law index varied from $n = 0.6$ to $n = 1.4$ and the retardation effect was quantified by the velocity correction factor given by (UHLHERR; CHHABRA, 1995):

$$f_w = \frac{V_T}{V_{T\infty}} \tag{7.2}$$

where V_T is the terminal velocity obtained in a bounded domain while $V_{T\infty}$ is obtained in an unbounded domain. To determine how far from the particle the boundary must be
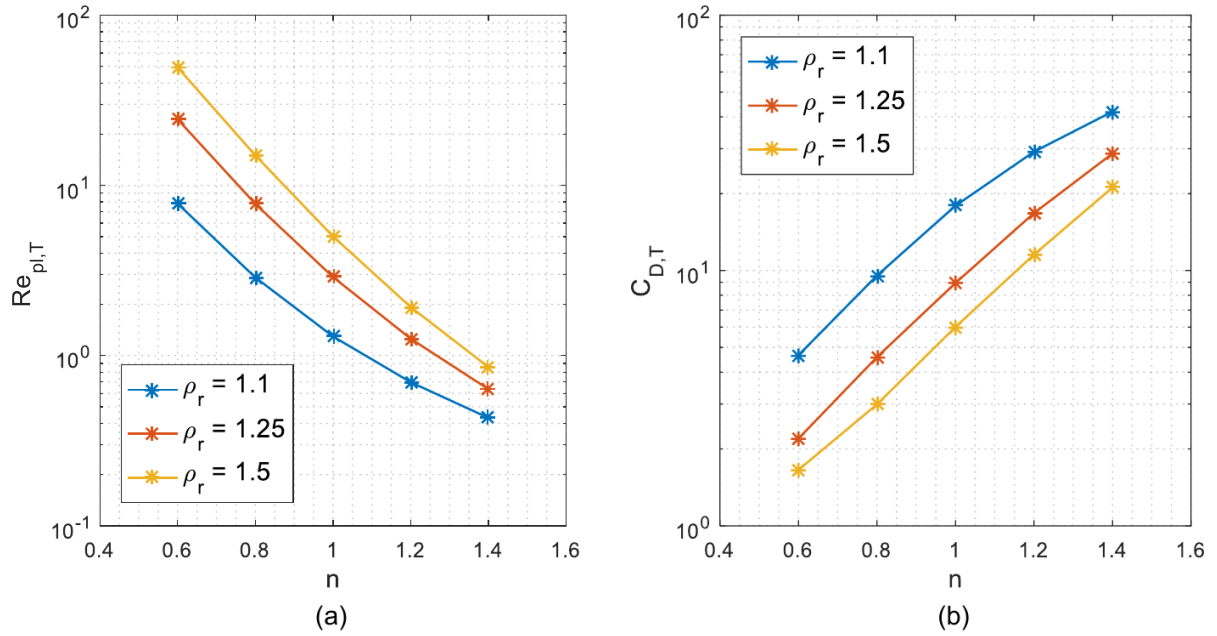
Figure 7.3 – Influence of particle/fluid density ratio (a) on $Re_{pl,T}$ and (b) on $C_{D,T}$ as a function of n.

placed in order to avoid wall effects, so that the domain is considered unbounded, the aspect ratio between particle and container width ($R = L/d$) were investigated. Its influence was observed for the most shear-thinning ($n = 0.6$), Newtonian ($n = 1$) and the most shear-thickening ($n = 1.4$) fluid behavior. The increase in terminal particle velocity (V_T) with increasing L/d is presented in Tab. 7.4.

Table 7.4 – Wall effect measured by the increase of V_T with increasing R.

			n			
		0.6		1		1.4
$R = L/d$	V_T	V_T increase	V_T	V_T increase	V_T	V_T increase
8	-4.621	-	-2.316	-	-1.294	-
16	-5.069	9.7 %	-2.853	23.2%	-1.930	49.2%
32	-5.230	3.2%	-3.080	8.0%	-2.260	17.1%
64	-5.290	1.1%	-3.178	3.2%	-2.380	5.3%
80	-5.312	0.4%	-3.190	0.4%	-2.404	1.0%

The domain was considered unbounded when the increase in V_T with increasing L/d was less or equal to 1%, which was achieved when L was 80 times larger than the particle diameter. The correction factor where then calculated using Eq. 7.2 and results are presented in Tab. 7.5. This results help to quantify the retardation effect of the confining walls on terminal velocity. Low correction factor f_w implies higher wall retardation effect.

For a better visualization of these results, the correction factors are presented in Tab.7.5

Table 7.5 – Velocity correction factor obtained for $d = 0.125\ cm$ and $\rho_r = 1.25\ g/cm^3$.

	n				
$R = L/d$	0.6	0.8	1.0	1.2	1.4
8	0.870	0.813	0.726	0.627	0.538
16	0.954	0.929	0.894	0.852	0.803
32	0.985	0.980	0.966	0.957	0.940
64	0.996	0.998	0.996	0.997	0.990
$R > 80$	1.000	1.000	1.000	1.000	1.000

for different values of R as a function of n, as shown in Figure 7.4. As can be seen, shear-thinning fluids ($n < 1$) are less affected by retardation effects due to confinement walls presence. This is perceived by an approximation of the curves at different values of R as they become closer while n decreases. On the other hand, for shear-thickening fluids ($n > 1$), the particle motion is more dependent on wall effects. This is also perceived through the vorticity contours, shown in Figure 7.5, at a same vertical position for different values of n at $L/d = 8$. At $n = 1.4$ the vorticity contours are clearly affected by the container walls and this effect diminishes with decreasing n. For $n = 0.6$ the terminal Reynolds is much higher than for $n = 1.4$. At higher $Re_{pl,T}$ the retardation effect due to particle confinement becomes less significant due to increase of inertial influence.
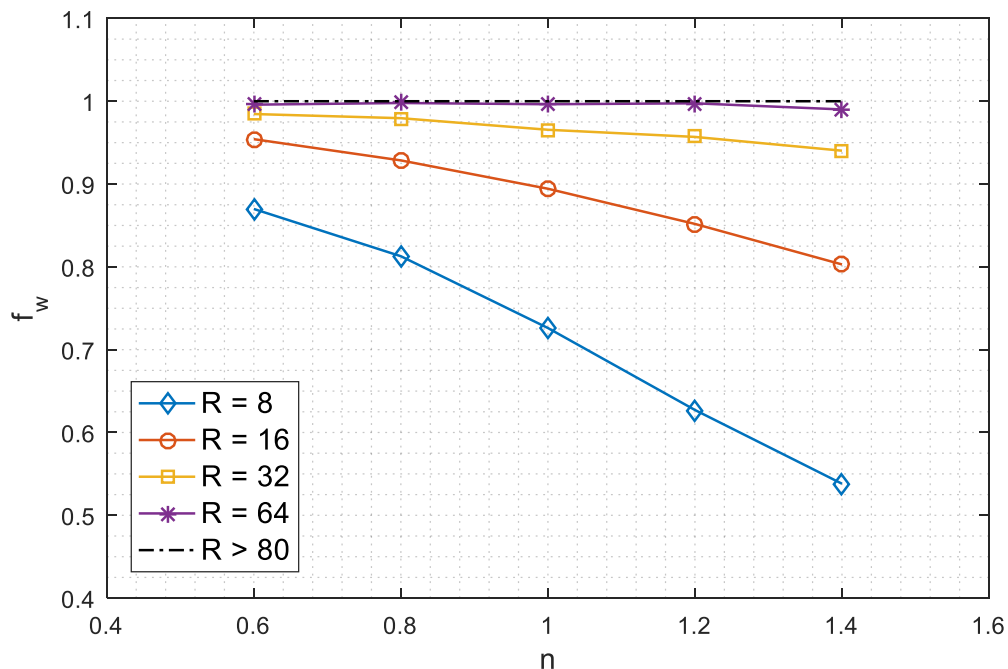
Figure 7.4 – Velocity correction factor, f_w, as a function of n for different aspect ratios.

This tendency of diminishing wall effects with decreasing n are similar to those reported in literature ((MISSIRLIS et al., 2001), (SONG; GUPTA; CHHABRA, 2009)). It is important to emphasize that this section focused on investigating the wall effect as a function of n and R
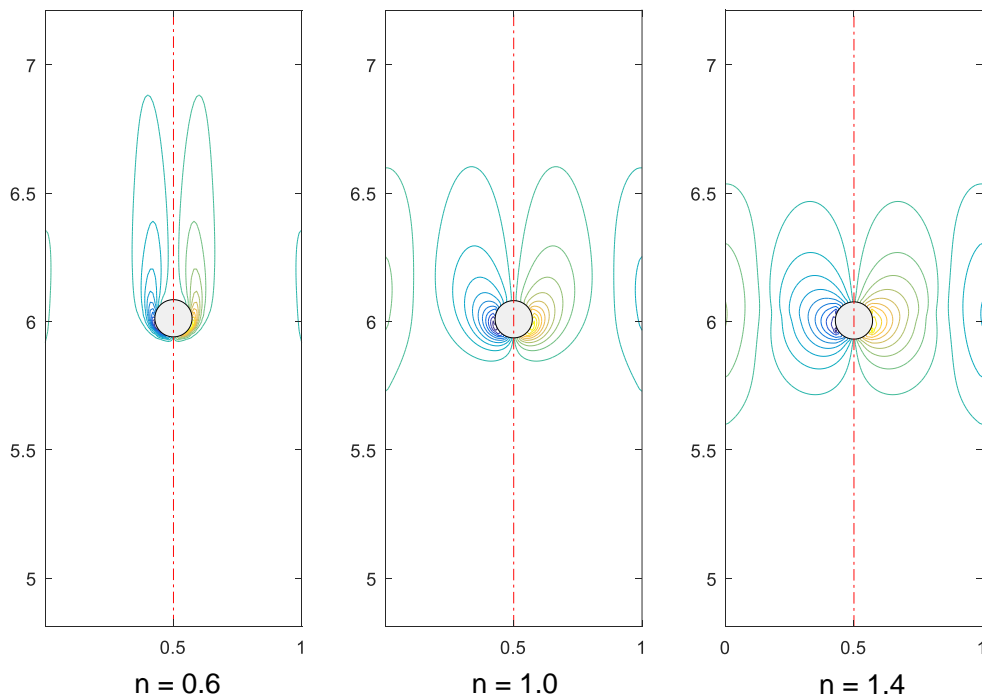
Figure 7.5 – Vorticity contours for different n values at $y = 6.0\ cm$.

only, and the correction factors presented in Tab.7.5 can not be applied to different values of d and ρ_r, since the wall factor is not a function of R and n alone, but also of $Re_{pl,T}$ as suggested in previous works found in the literature (UHLHERR; CHHABRA, 1995).

7.1.5.1 Simulated drag coefficient $\times$ standard drag curve for Newtonian fluid

In order to strengthen the validation of IB-LBM for moving boundaries, now that the necessary container width for particle sedimentation to take place in an unbounded domain is known, it was possible to redo simulations of particle settling in Newtonian fluids ($n = 1$) and compare results for $C_{D,T}$ as a function of $Re_{pl,T}$ with the standard drag curve for flow past over a cylinder.

Results for $C_{D,T}$ and $Re_{pl,T}$ were also obtained in an unbounded domain ($L/d = 80$) for $d = 0.00625\ cm$ and $0.125\ cm$. Figure 7.6 shows results for $C_{D,T}$ as a function of $Re_{pl,T}$ in an unbounded domain and for $R = 8$. Results are in good agreement with the standard drag curve which shows that IB-LBM is able to solve precisely the problem of particle sedimentation.

The curve obtained for $R = 8$ is shifted for both $Re_{pl,T}$ and $C_{D,T}$ values, this is expected because both dimensionless numbers are function of particle settling velocity and the retardation effect due wall confinement leads to decrease settling velocity and consequently to decrease $Re_{pl,T}$ and increase $C_{D,T}$.
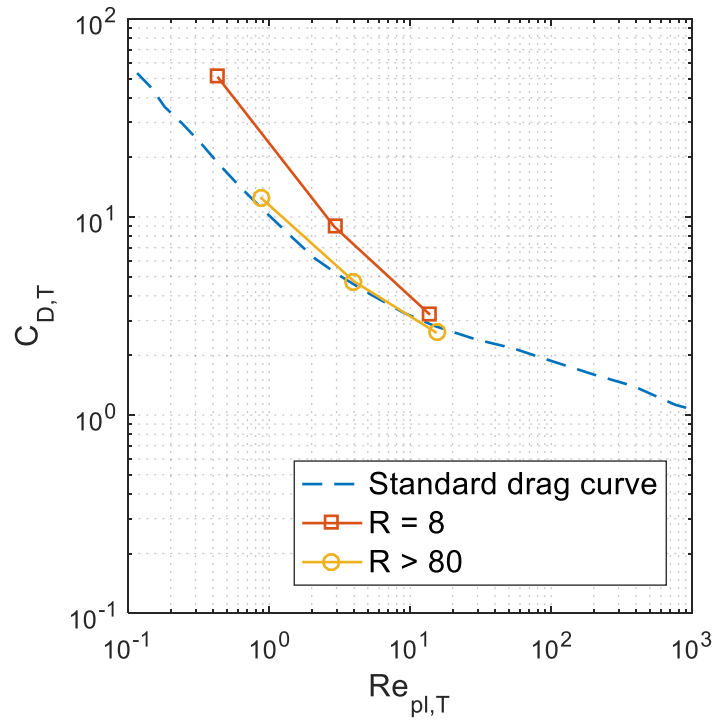
Figure 7.6 – $C_{D,T}$ as a function of $Re_{pl,T}$ for $R = 8$ and $R > 80$ compared with standard drag curve for 2D flow past over a cylinder (KUNDU; COHEN; DOWLING, 2008) for the Newtonian case.

7.1.6 Simulated $\times$ Calculated $C_{D,T}$

When the particle reaches its terminal settling velocity the drag force is balanced by buoyant and weight such as:

$$F_D = g(\rho_p - \rho_f)\cancel{V} \tag{7.3}$$

Further, the drag coefficient C_D is the non-dimensional drag force, given by (CHHABRA, 2006):

$$C_D = \frac{F_D}{1/2\rho_f V^2 d} \tag{7.4}$$

Combining Equations 7.3 and 7.4, C_D can be obtained from the force balance as a function of terminal settling velocity:

$$C_{D,T} = \frac{g(\rho_r - 1)\pi d}{2V_T^2} \tag{7.5}$$

Table 7.6 shows the differences between $C_{D,T}$ obtained for an unbounded media ($D/d = 80$) from simulations and from the one based on equation 7.4 for different values of n.

Table 7.6 – Comparison between simulated and calculated $C_{D,T}$

	n				
	0.6	0.8	1.0	1.2	1.4
$C_{D,T\infty}$ from Eq. 7.4	1.707	3.016	4.732	6.606	8.334
$C_{D,T\infty}$ simulated	1.767	3.052	4.743	6.582	8.307
Percentage deviation	3.43%	1.16%	0.23%	0.36%	0.32%

$C_{D,T}$ simulated differs from $C_{D,T}$ calculated from Equation 7.4 by small values. The differences increases as n decreases and the settling velocity gets higher. This reveals that further investigation is required to improve the numerical results for $C_{D,T}$ as $Re_{pl,T}$ increases. It has been shown that the present results are independent from spatial and temporal mesh so that the compressibility effects were also insignificant in the performed simulations ($Ma << 1$) (see Appendix A). Thus, for higher values of $Re_{pl,T}$ it is necessary to improve the accuracy of the curved boundary. In this work, the exchange of information between the Eulerian and Lagrangian meshes were carried out using a 2-point discrete delta interpolation function in which the Cartesian nature of the lattice structures may not be well hidden (KRÜGER, 2011). This may be the cause of the increase percentage deviation between the simulated and calculated $C_{D,T}$ with increasing V_T, since the forces acting on the immersed boundary are based on the interpolation function.

7.2 Part 2: Generalized results for $C_{D,T}$ and $Re_{pl,T}$ as a function of Ar_{pl} and n

As discussed in section 7.1.5.1, the drag coefficient and Reynolds number experienced by the particle at its terminal settling velocity are both dependent of V_T. For this reason the traditional plot of $C_D \times Re_{pl,T}$ may not be convenient for settling particles once its terminal settling velocity is previously unknown. To overcome this issue, results obtained for $C_{D,T}$ and $Re_{pl,T}$ can be represented as a function of a single dimensionless number, the generalized Archimedes number, Ar_{pl}, which is the dimensionless number given by Equation 4.22, which relates the gravitational forces acting on the particle with respect to the viscous forces. (FORNARI; PICANO; BRANDT, 2016). Further, the drag coefficient for a particle falling in a fluid is better represented as a function of the driven forces of the problem (buoyancy and weight) and not as a function of V_T or $Re_{pl,T}$. Therefore Ar_{pl} is a good choice to represent the results because it is independent of V_T and can be evaluated from the physical properties of particle and fluid (see section 4.5).

Figures 7.7 and 7.8 summarize all the results of $C_{D,T}$ and $Re_{pl,T}$ obtained in the previous section, for $R = 8$, as a function of Ar_{pl}. It can be seen that results are dependent only on Ar_{pl} and n. High values of Ar_{pl} indicates that gravitational force is more relevant to the

particle motion than the viscous forces.

Figure 7.7 shows that within the analysed range of Ar_{pl} all the curves tend to pass through a common point. For a given value of Ar_{pl} above this point an increase on n causes a decrease on $Re_{pl,T}$. On the other hand, for Ar_{pl} values below the common point, increasing n implies a increase of $Re_{pl,T}$. A similar tendency is observed for $C_{D,T}$ as a function of Ar_{pl} in Figure 7.8. There is also a common point for all the curves in which values of Ar_{pl} above it imply a reduction of the $C_{D,T}$ with the increase of n and for Ar_{pl} below it $C_{D,T}$ is increased by increasing n.
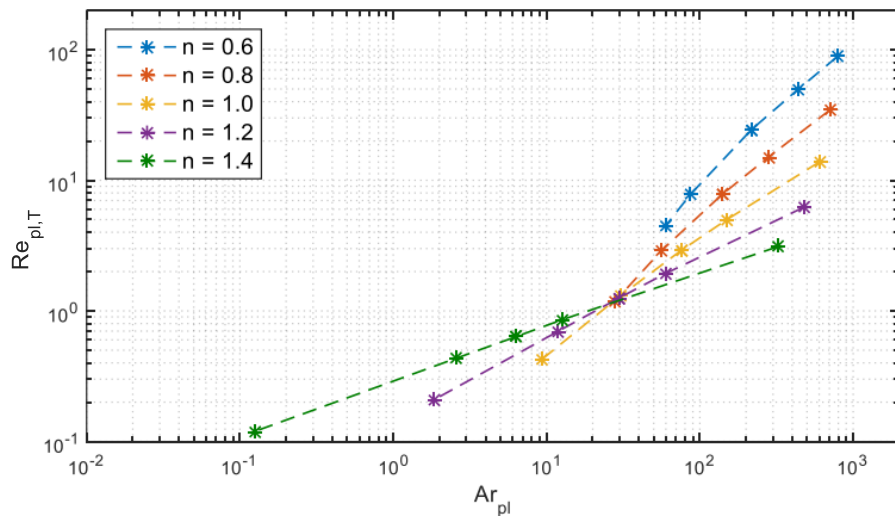
Figure 7.7 – Terminal settling Reynolds as a function of Ar_{pl} for different n.
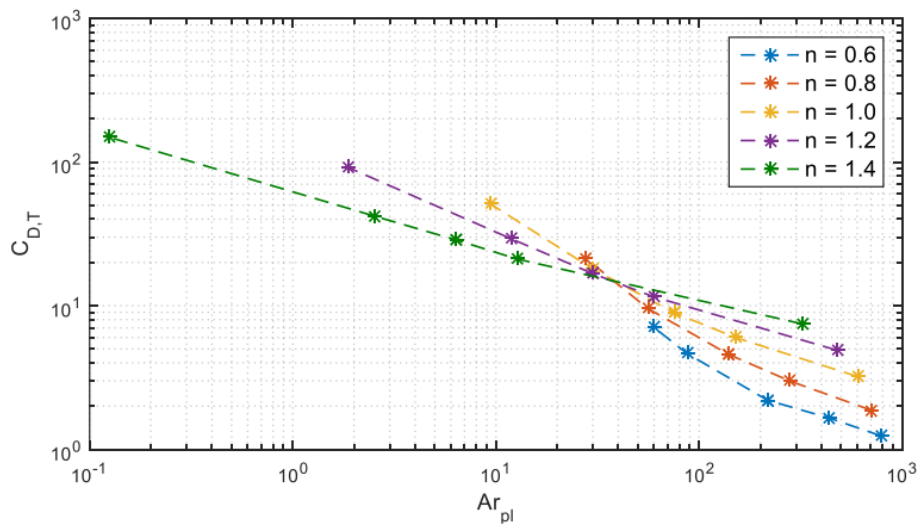
Figure 7.8 – Drag coefficient experienced by the particle at its terminal settling velocity as a function of Ar_{pl} for different n.

7.2.1 Unsteady flow at high Ar_{pl} and low n

As shown in Figure 7.7, $Re_{pl,T}$ increases with increasing Ar_{pl} and decreasing n. It is well known that when $Re_{pl,T}$ increases to some critical value, flow shifts to unsteady regime where release of vortex are observed, as discussed in section A.3. It was noticed that after reaching a maximum settling velocity the particle takes a finite time until the first vortex are released. Although the particle has reached the maximum velocity within the 10 cm container, it needs more sedimenting time for the vortex release to occur. To observe what happens when the particle settles in an unsteady regime, the container height was increase to $30\ cm$ and the settling of particles at High Ar_{pl} and low n was investigated.

It was observed in the previous simulations that the highest value of $Re_{pl,T}$ occurred for a particle diameter of $d = 0.25$, $\rho_r = 1.25$ and $n = 0.6$, which resulted in a Archimedes number of $Ar_{pl} = 787$. Figure 7.9 shows vorticity contours at different times after the particle release.

After unsteady flow takes place the particle starts deviating from the symmetry plane and follows an oblique zigzag pattern as can be seen in Figure 7.9.c and also by the evolution of particle transversal position in Figure 7.10.b. The particle vertical velocity is greatly affected as its transversal velocity increases due the vortex release, as shown in Figure 7.11.a.
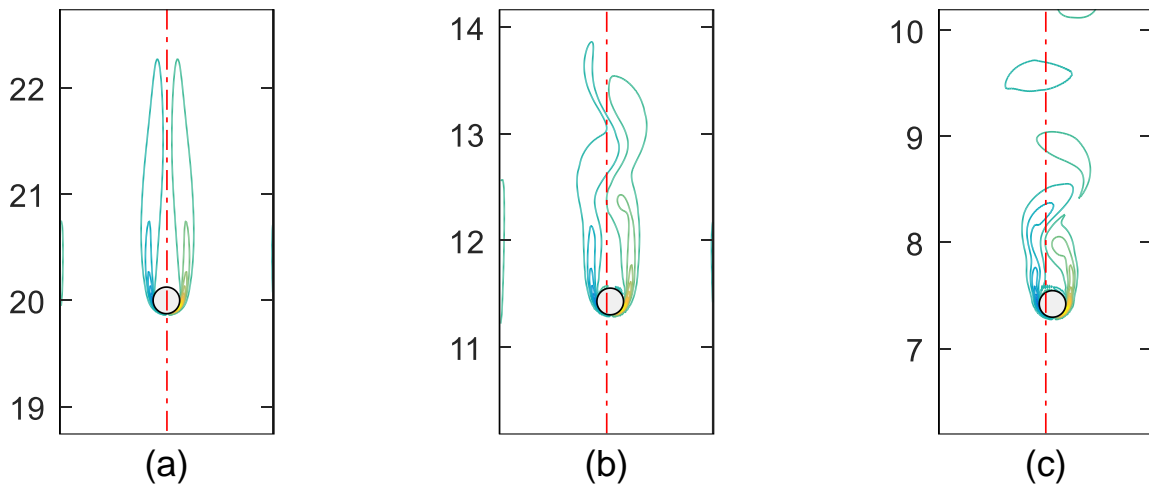
Figure 7.9 – Vorticity contours for $n = 0.6$ and $Ar_{pl} = 787$. (a) after $1.0\ s$, (b) $2.0\ s$ and (c) $2.5\ s$

7.3 Closing remarks

Simulations show that the particle settling dynamics is considerably influenced by the Power-law fluid behavior. For low Power-law index the viscous effects become less significant, and the settling velocity increases regardless of the particle size or ρ_r combination, which is perceived with an increase in $Re_{pl,T}$. In the parametric analysis the settling dynamics of different sized particles showed to be independent of n, that is, $Re_{pl,T}$ and $C_{D,T}$ change with

(a)

(b)
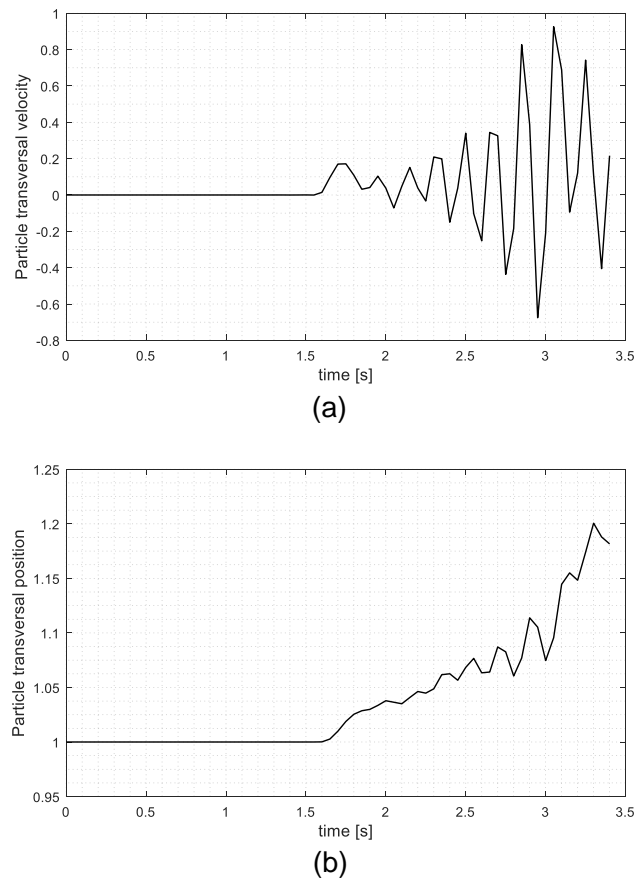
Figure 7.10 – (a) Particle transversal velocity and (b) Particle transversal position for $n = 0.6$ and $Ar_{pl} = 787$.

n in the same proportions regardless of the particle size. The influence of n for different particle/fluid density ratio shows that at low ρ_r, $Re_{pl,T}$ and $C_{D,T}$ are more affected by the Power-law index than at high ρ_r.

All the obtained results were then written as a function of the generalized Archimedes number (Ar_{pl}). It was noticed that the particle settling dynamics in Power-law fluids can be described by two parameters: Ar_{pl} and n. Thus, with prior knowledge of Ar_{pl}, which can be directly obtained from fluid and particle properties, it is possible to determine the maximum settling velocity of the particle for a given n using the $Ar_{pl} \times Re_{pl,T}$ graph (Fig.7.7) or the drag coefficient experienced by the particle using the $Ar_{pl} \times C_{D,T}$ graph (Fig.7.8). Despite the versatility of these graphs to represent and correlate results for particle sedimentation, only a few results correlated with Archimedes number are found in literature (Karamanev (1996); Khan and Richardson (1987)). For particle sedimentation in Power-law fluids, covering shear-thinning and shear-thickening behavior relation of $C_{D,T}$ and $Re_{pl,T}$ as function of Ar_{pl} were still lacking in literature.

Results presented for unsteady flow is an indication that a regime map can be constructed in terms of Ar_{pl} and n in a similar way to the existing maps for Newtonian fluids (see Fig.3.2).
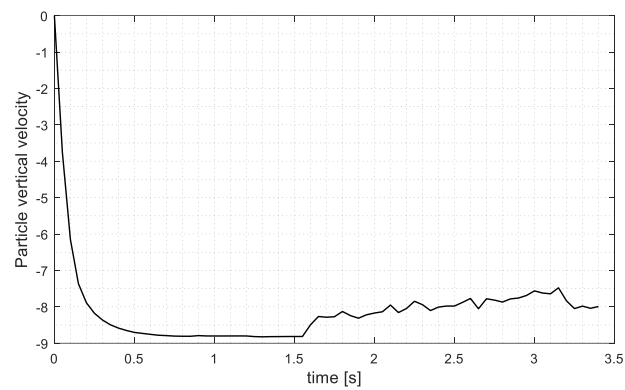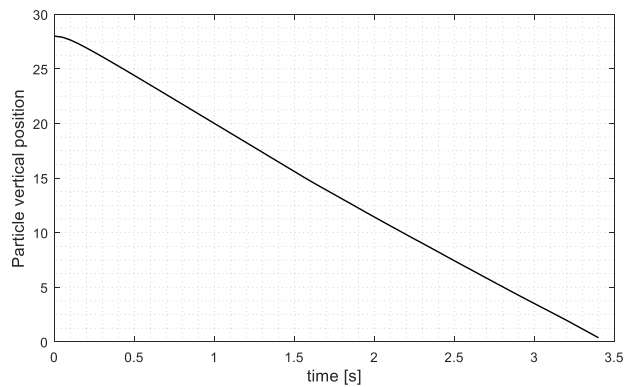
Figure 7.11 – (a) Particle vertical velocity and (b) Particle vertical position for $n = 0.6$ and $Ar_{pl} = 787$.

Analogous to what is observed for Newtonian regime map (DOYCHEV, 2015), it is possible to presume that the settling dynamics in a Power-law fluid changes from vertical to oblique and chaotic settlings with increasing Ar_{pl} and decreasing n. However, it is necessary to perform a much larger number of simulations to ensure this tendency and construct a map of regimes.

8 Conclusions and Recommendations

In the scenario of the oil and gas industry, cuttings sedimentation are critical during an operational stop, since it can lead to drill obstruction and even to well collapse. Therefore, it is always important to increase the knowledge of particle dynamics in drilling muds. Thus, the present work proposed the development of a computational code able to simulate particle sedimentation in Power-law fluid, which is able to describe the shear-thinning rheological behavior of drilling muds. To do so, a program was developed, based on the lattice Boltzmann method, using FORTRAN language. The particle fluid coupling was performed by the immersion boundary method and the non-Newtonian behavior of the fluid was incorporated by the viscosity adaptation method.

Through verification cases, the developed program ability to solve problems of settling particles in Newtonian and Power-law fluid was proved to be satisfactory. A parametric study was then performed, varying the Power-law index, n, the particle diameter, d, and particle/fluid density ratio ρ_r. In the parametric analysis the influence of n on the terminal generalized Reynolds number, $Re_{pl,T}$, and on the drag coefficient experienced by the particle at its terminal velocity, $C_{D,T}$, is the same regardless of the particle diameter. It also reveals that at low values of solid to fluid density ration, ρ_r, $Re_{pl,T}$ and $C_{D,T}$ are more affected by the Power-law index than at higher ρ_r.

With those simulations, was perceived that all the results could be written as a function of 2 parameters: the Archimedes number and the Power-law index. Those results prove to be important, since $C_{D,T}$ and Re_{Tpl} can be written as a function of the fluid and particle properties and these relations were still lacking in the literature.

An unsteady settling is observed as $Re_{pl,T}$ increases with increasing the generalized Archimedes number, Ar_{pl}, and decreasing n. Thus, depending on $Re_{pl,T}$ the particle settling may go through different regimes, whether vertical or oblique zigzag. One advantage of having a $Ar_{pl} \times Re_{pl,T}$ plot for Power-law fluids is that the fluid and particle properties can be chosen in accordance with the sedimentation regime with which is desired to work in an experimental apparatus.

8.1 Recommendations

The main objective of the present work was the development of a 2D program capable of solving particle sedimentation in Power-law fluids. This has been successfully achieved by now, however, in order to allow broader applications, improvements on the program algorithm still must be done.

In order to verify if the 2-point discrete delta interpolation function is the most adequate to deal with the exchange of information between the Eulerian and Lagrangian meshes, it is recommended to apply different interpolation functions, such as those described by Peskin (1977), and verify its influence on results, especially on $C_{D,T}$.

Also, for future works, it is indicated to perform investigation regarding effects of fluid rheology on the particle angular velocity and orientation, since the applied algorithm is able to capture this information. The particle-wall or particle-particle interaction were not addressed on the present work, although its investigation are important especially when more particles are present in the system, which is a situation closer to that found in industrial process where particle settling is important, so, it is recommended for future works.

Further, for the particle sedimentation results to have a more appropriate physical meaning, it is recommended to extend the program to 3D problems, so the particle dynamics can be validated with experimental sedimentation results available in the literature. It is also important to extend the problem to more complex rheology fluids such as viscoplastic and thyrotropic fluid behavior, since these rheological properties are also present in the drilling fluids and it is also of interest for other industrial applications. Also, a more extensive parametric investigation should be performed in order to construct a regime map.

At last, LBM is very suitable for the parallel computation, which has not been done in the present work, then being recommended for future works.

Bibliography

BEHREND, O. Solid-fluid boundaries in particle suspension simulations via the lattice Boltzmann method. *Physical Review E*, APS, v. 52, n. 1, p. 1164, 1995.

BENEDETTO, A.; UMILIACO, A. Evaluation of hydraulic permeability of open-graded asphalt mixes using a full numerical simulation. *Journal of Materials in Civil Engineering*, American Society of Civil Engineers, v. 26, n. 4, p. 599–606, 2013.

BHARTI, R. P.; CHHABRA, R.; ESWARAN, V. Two-dimensional steady poiseuille flow of power-law fluids across a circular cylinder in a plane confined channel: wall effects and drag coefficients. *Industrial & Engineering Chemistry Research*, ACS Publications, v. 46, n. 11, p. 3820–3840, 2007.

BHATNAGAR, P. L.; GROSS, E. P.; KROOK, M. A model for collision processes in gases. i. small amplitude processes in charged and neutral one-component systems. *Physical Review*, APS, v. 94, n. 3, p. 511, 1954.

BIRD, R.; ARMSTRONG, R.; HASSAGER, O.; CURTISS, C. *Dynamics of polymeric liquids*. [S.l.]: Wiley New York, 1977.

BRAZA, M.; CHASSAING, P.; MINH, H. H. Numerical study and physical analysis of the pressure and velocity fields in the near wake of a circular cylinder. *Journal of Fluid Mechanics*, Cambridge University Press, v. 165, p. 79–130, 1986.

CARREAU, P. J. Rheological equations from molecular network theories. *Transactions of the Society of Rheology*, SOR, v. 16, n. 1, p. 99–127, 1972.

CATE, A. T.; NIEUWSTAD, C.; DERKSEN, J.; AKKER, H. Van den. Particle imaging velocimetry experiments and lattice-Boltzmann simulations on a single sphere settling under gravity. *Physics of Fluids*, AIP, v. 14, n. 11, p. 4012–4025, 2002.

CHEN, S.; DOOLEN, G. D. Lattice Boltzmann method for fluid flows. *Annual Review of Fluid Mechanics*, Annual Reviews 4139 El Camino Way, PO Box 10139, Palo Alto, CA 94303-0139, USA, v. 30, n. 1, p. 329–364, 1998.

CHHABRA, R. P. *Bubbles, drops, and particles in non-Newtonian fluids*. [S.l.]: CRC press, 2006.

CHOPARD, B.; DROZ, M. *Cellular automata*. [S.l.]: Springer, 1998.

CLIFT, R.; GRACE, J. R.; WEBER, M. E. *Bubbles, drops, and particles*. [S.l.]: Courier Corporation, 2005.

COUTANCEAU, M.; BOUARD, R. Experimental determination of the main features of the viscous flow in the wake of a circular cylinder in uniform translation. part 1. steady flow. *Journal of Fluid Mechanics*, Cambridge Univ Press, v. 79, n. 02, p. 231–256, 1977.

CROWE, C. T.; SCHWARZKOPF, J. D.; SOMMERFELD, M.; TSUJI, Y. *Multiphase flows with droplets and particles*. [S.l.]: CRC press, 2011.

DASH, S. M. *Development of a flexible forcing immersed boundary-lattice Boltzmann method and its applications in thermal and particulate flows*. PhD Thesis — National University ofF Singapore, 2014.

DAUGAN, S.; TALINI, L.; HERZHAFT, B.; ALLAIN, C. Aggregation of particles settling in shear-thinning fluids. *The European Physical Journal E: Soft Matter and Biological Physics*, Springer, v. 9, n. 1, p. 55–62, 2002.

DELOUEI, A. A.; NAZARI, M.; KAYHANI, M.; KANG, S.; SUCCI, S. Non-newtonian particulate flow simulation: A direct-forcing immersed boundary–lattice Boltzmann approach. *Physica A: Statistical Mechanics and Its Applications*, Elsevier, v. 447, p. 1–20, 2016.

DERKSEN, J. Drag on random assemblies of spheres in shear-thinning and thixotropic liquids. *Physics of Fluids*, AIP, v. 21, n. 8, p. 083302, 2009.

DERKSEN, J. Assessing eulerian–lagrangian simulations of dense solid-liquid suspensions settling under gravity. *Computers & Fluids*, Elsevier, 2016.

DERKSEN, J.; PRASHANT. Simulations of complex flow of thixotropic liquids. *Journal of Non-Newtonian Fluid Mechanics*, Elsevier, v. 160, n. 2, p. 65–75, 2009.

DESHPANDE, A.; KRISHNAN, J.; KUMAR, S.; CHHABRA. *Rheology of complex fluids*. [S.l.]: Springer, 2010.

DOYCHEV, T. *The dynamics of finite-size settling particles*. [S.l.]: KIT Scientific Publishing, 2015.

ESHGHINEJADFARD, A.; ABDELSAMIE, A.; JANIGA, G.; THÉVENIN, D. Direct-forcing immersed boundary lattice Boltzmann simulation of particle/fluid interactions for spherical and non-spherical particles. *Particuology*, Elsevier, v. 25, p. 93–103, 2016.

EWOLDT, R. H.; MCKINLEY, G. H. Mapping thixo-elasto-visco-plastic behavior. *Rheologica Acta*, Springer, v. 56, n. 3, p. 195–210, 2017.

FENG, Z.-G.; MICHAELIDES, E. E. The immersed boundary-lattice Boltzmann method for solving fluid–particles interaction problems. *Journal of Computational Physics*, Elsevier, v. 195, n. 2, p. 602–628, 2004.

FERNANDES, R. *Relação entre o limite de viscoelasticidade linear e o escoamento de um fluido elastoviscoplástico.* Dissertation — UTFPR, 2016.

FORNARI, W.; PICANO, F.; BRANDT, L. Sedimentation of finite-size spheres in quiescent and turbulent environments. *Journal of Fluid Mechanics*, Cambridge University Press, v. 788, p. 640–669, 2016.

GOYAL, N.; DERKSEN, J. Direct simulations of spherical particles sedimenting in viscoelastic fluids. *Journal of Non-Newtonian Fluid Mechanics*, Elsevier, v. 183, p. 1–13, 2012.

GUO, Z.; SHU, C. *Lattice Boltzmann method and its applications in engineering*. [S.l.]: World Scientific, 2013.

GUO, Z.; ZHENG, C.; SHI, B. Discrete lattice effects on the forcing term in the lattice Boltzmann method. *Physical Review E*, APS, v. 65, n. 4, p. 046308, 2002.

HE, X.; CHEN, S.; DOOLEN, G. D. A novel thermal model for the lattice Boltzmann method in incompressible limit. *Journal of Computational Physics*, Elsevier, v. 146, n. 1, p. 282–300, 1998.

HOROWITZ, M.; WILLIAMSON, C. The effect of Reynolds number on the dynamics and wakes of freely rising and falling spheres. *Journal of Fluid Mechanics*, Cambridge University Press, v. 651, p. 251–294, 2010.

KANG, S. K. *Immersed boundary methods in the lattice Boltzmann equation for flow simulation*. PhD Thesis — Texas A&M University, 2010.

KARAMANEV, D. Equations for calculation of the terminal velocity and drag coefficient of solid spheres and gas bubbles. *Chemical Engineering Communications*, Taylor & Francis, v. 147, n. 1, p. 75–84, 1996.

KEUNINGS, R.; CROCHET, M. Numerical simulation of the flow of a viscoelastic fluid through an abrupt contraction. *Journal of Non-Newtonian Fluid Mechanics*, Elsevier, v. 14, p. 279–299, 1984.

KHAN, A.; RICHARDSON, J. The resistance to motion of a solid sphere in a fluid. *Chemical Engineering Communications*, Taylor & Francis, v. 62, n. 1-6, p. 135–150, 1987.

KRÜGER, T. Introduction to the immersed boundary method. In: *LBM Workshop, Edmonton*. [S.l.: s.n.], 2011.

KRÜGER, T.; KUSUMAATMAJA, H.; KUZMIN, A.; SHARDT, O.; SILVA, G.; VIGGEN, E. M. The lattice Boltzmann method. Springer, 2017.

KUNDU, P. K.; COHEN, I. M.; DOWLING, D. *Fluid Mechanics 4th*. [S.l.]: Elsevier, 2008.

LADD, A.; VERBERG, R. Lattice-Boltzmann simulations of particle-fluid suspensions. *Journal of Statistical Physics*, Springer, v. 104, n. 5-6, p. 1191–1251, 2001.

LADD, A. J.; FRENKEL, D. Dissipative hydrodynamic interactions via lattice-gas cellular automata. *Physics of fluids A: fluid dynamics*, AIP, v. 2, n. 11, p. 1921–1924, 1990.

LALLEMAND, P.; LUO, L.-S. Lattice Boltzmann method for moving boundaries. *Journal of Computational Physics*, Elsevier, v. 184, n. 2, p. 406–421, 2003.

LIU, H.; KANG, Q.; LEONARDI, C. R.; SCHMIESCHEK, S.; NARVÁEZ, A.; JONES, B. D.; WILLIAMS, J. R.; VALOCCHI, A. J.; HARTING, J. Multiphase lattice Boltzmann simulations for porous media applications. *Computational Geosciences*, Springer, v. 20, n. 4, p. 777–805, 2016.

LUO, L.-S. Theory of the lattice Boltzmann method: Lattice Boltzmann models for nonideal gases. *Physical Review E*, APS, v. 62, n. 4, p. 4982, 2000.

MARCHI, C. H.; SUERO, R.; ARAKI, L. K. The lid-driven square cavity flow: numerical solution with a 1024 x 1024 grid. *Journal of the Brazilian Society of Mechanical Sciences and Engineering*, SciELO Brasil, v. 31, n. 3, p. 186–198, 2009.

MEIRA, R. E. D. C. P. D. *Estudo do escoamento de fluidos de lei de potência e de Bingham em canal parcialmente poroso utilizando o método lattice Boltzmann*. Dissertation — UTFPR, 2016.

MELE, I. Lattice Boltzmann method. In: *Seminar, Faculty of mathematics and physics, Ljubljani Univ., Ljubljana*. [S.l.: s.n.], 2013. p. 2012–2013.

MISSIRLIS, K.; ASSIMACOPOULOS, D.; MITSOULIS, E.; CHHABRA, R. Wall effects for motion of spheres in power-law fluids. *Journal of Non-Newtonian Fluid Mechanics*, Elsevier, v. 96, n. 3, p. 459–471, 2001.

MOHAMAD, A. A. *Lattice Boltzmann method: fundamentals and engineering applications with computer codes*. [S.l.]: Springer Science & Business Media, 2011.

MORRISON, F. A. *Understanding rheology*. [S.l.]: Oxford University Press, USA, 2001.

MUJUMDAR, A.; BERIS, A. N.; METZNER, A. B. Transient phenomena in thixotropic systems. *Journal of Non-Newtonian Fluid Mechanics*, Elsevier, v. 102, n. 2, p. 157–178, 2002.

NGUYEN, J. *Drilling-oil and gas field development techniques*. [S.l.]: Editions Technip, 1996. 353 p.

PARK, J.; KWON, K.; CHOI, H. Numerical solutions of flow past a circular cylinder at reynolds numbers up to 160. *KSME international Journal*, Springer, v. 12, n. 6, p. 1200–1205, 1998.

PESKIN, C. S. Numerical analysis of blood flow in the heart. *Journal of Computational Physics*, Elsevier, v. 25, n. 3, p. 220–252, 1977.

REYNOLDS, P.; JONES, T. An experimental study of the settling velocities of single particles in non-newtonian fluids. *International Journal of Mineral Processing*, Elsevier, v. 25, n. 1-2, p. 47–77, 1989.

SEO, J. H.; MITTAL, R. A sharp-interface immersed boundary method with improved mass conservation and reduced spurious pressure oscillations. *Journal of Computational Physics*, Elsevier, v. 230, n. 19, p. 7347–7363, 2011.

SILVA, R.; GARCIA, F. A.; FAIA, P. M.; RASTEIRO, M. G. Settling suspensions flow modelling: A review. *KONA Powder and Particle Journal*, Hosokawa Powder Technology Foundation, v. 32, p. 41–56, 2015.

SONG, D.; GUPTA, R. K.; CHHABRA, R. P. Wall effects on a sphere falling in quiescent power law fluids in cylindrical tubes. *Industrial & Engineering Chemistry Research*, ACS Publications, v. 48, n. 12, p. 5845–5856, 2009.

STOKES, G. G. *On the effect of the internal friction of fluids on the motion of pendulums*. [S.l.]: Pitt Press, 1851.

SUCCI, S. *The lattice Boltzmann equation: for fluid dynamics and beyond*. [S.l.]: Oxford university press, 2001.

SUI, Y.; CHEW, Y.-T.; ROY, P.; LOW, H.-T. A hybrid immersed-boundary and multi-block lattice Boltzmann method for simulating fluid and moving-boundaries interactions. *International Journal for Numerical Methods in Fluids*, Wiley Online Library, v. 53, n. 11, p. 1727–1754, 2007.

UHLHERR, P.; CHHABRA, R. Wall effect for the fall of spheres in cylindrical tubes at high reynolds number. *The Canadian Journal of Chemical Engineering*, Wiley Online Library, v. 73, n. 6, p. 918–923, 1995.

WANG, C.-H.; HO, J.-R. A lattice Boltzmann approach for the non-newtonian effect in the blood flow. *Computers & Mathematics with Applications*, Elsevier, v. 62, n. 1, p. 75–86, 2011.

WHITNEY, M. J.; RODIN, G. J. Force–velocity relationships for rigid bodies translating through unbounded shear-thinning power-law fluids. *International Journal of Non-Linear Mechanics*, Elsevier, v. 36, n. 6, p. 947–953, 2001.

WU, J.; SHU, C. Implicit velocity correction-based immersed boundary-lattice Boltzmann method and its applications. *Journal of Computational Physics*, Elsevier, v. 228, n. 6, p. 1963–1979, 2009.

YASUDA, K.; ARMSTRONG, R.; COHEN, R. Shear flow properties of concentrated solutions of linear and star branched polystyrenes. *Rheologica Acta*, Springer, v. 20, n. 2, p. 163–178, 1981.

YU, Z.; FAN, L.-S. Lattice Boltzmann method for simulating particle–fluid interactions. *Particuology*, Elsevier, v. 8, n. 6, p. 539–543, 2010.

ZHENG, L.; ZHENG, S.; ZHAI, Q. Kinetic theory based force treatment in lattice Boltzmann equation. *arXiv preprint arXiv:1708.06477*, 2017.

ZOU, Q.; HE, X. On pressure and velocity boundary conditions for the lattice Boltzmann BGK model. *Physics of Fluids*, AIP, v. 9, n. 6, p. 1591–1598, 1997.

APPENDIX A − Mesh sensitivity tests

In this appendix, sensitivity tests for Δx and Δt are presented. The tests were performed to cases whose results show greater sensitivity to Δx and Δt variations. In general, the results of the simulations are more sensitivity to Δx and Δt for lower values of n and higher values of Reynolds (MEIRA, 2016).

A.1   Lid-driven cavity

The sensitivity mesh tests for the lid-driven cavity were performed considering: $\nu = 0.001$ m^2/s, $H = 0.2\ m$ and $Re = 1000$. Results are considered to be mesh independent when the differences observed on the minimum velocity measured in the velocity profile at the cavity center for both x and y directions are less than 0.1%. This difference was calculate according to:

$$Error = \left| \frac{\theta_{coarse} - \theta_{refined}}{\theta_{coarse}} \right| \times 100 \tag{A.1}$$

where θ_{coarse} is the value of the parameter of interest for the coarse mesh and $\theta_{refined}$ is the parameter value at the subsequent refined mesh.

To perform the mesh sensitivity test as described in section 5.9, first, a coarse mesh with only 50 nodes along x and y directions is applied. Then, the relation $\Delta x/\Delta t$ is increased by decreasing Δt which causes a reduction on relaxation time τ (see Eq. 5.53). Decreasing τ by refining the temporal mesh causes a simultaneous decrease on the compressible effects, as described in section 5.9. However, as $\tau \to 0.5$ the simulation becomes instable (KRÜGER et al., 2017). For the case of lid-driven cavity flow it was unable to perform simulations for τ under 0.547 as shown in Tab. A.1. For this reason τ was kept at 0.547.

After that, the spatial mesh was refined keeping τ fixed. As can be seen in Tab. A.1 increasing the number of points along x and y directions (N) from $N = 200$ to $N = 400$ the results observed for the minimum velocities at the velocity profiles at the cavity center line in x and y directions showed very small changes ($< 0.1\%$). Then, for the lid-driven cavity problem, the simulations were performed for $\tau = 0.547$ and $N = 200$. The Reynolds number of this problem was varied by changing the lid velocity.

A.2   Power-law flow between plates

The sensitivity mesh tests for Power-law flow between plates were performed considering $Re = 1$, $n = 0.25$. The apparent viscosity used was $m = 0.1\ m^2/s$. Results are considered

Table A.1 – Mesh sensitivity tests for lid-driven cavity flow problem.

$test$	N	$\Delta x/\Delta t$	τ	U_{min}	$Error[\%]$	V_{min}	$Error[\%]$
Δt	50	8	0.594	-0.4025	-	-0.5382	-
		16	0.547	-0.4015	0.265	-0.5365	0.321
		32*	0.523	-	-	-	-
Δx	50	16		-0.4015	-	-0.5365	-
	100	32		-0.3901	2.614	-0.5297	1.276
	200	64	0.547	-0.3890	0.495	-0.5276	0.382
	400	128		-0.3887	0.095	-0.5271	0.096

*Unable to perform simulation due numerical instability

to be mesh independent when the differences observed on the maximum velocity measured in the velocity profile at the channel outlet between a coarse mesh and a subsequence refined mesh are less than 1%.

Again, the first step was to conduct a sensibility test for Δt. A coarse mesh of $N = 40$ nodes was applied to the y direction. Then the initial τ, τ_0, was decrease until the stability limit. Although the difference observed for the maximum velocity measured in the velocity profile at the channel outlet is still large when τ_0 changes from 0.506 to 0.502 (1.68% of difference) as shown in Tab. A.2, for this present problem, the program was unable to perform simulations for τ_0 under 0.502. For this reason τ_0 was kept at 0.502.

Table A.2 – Temporal mesh sensitivity test for Power-law fluid flow between parallel plates

test	N	$\Delta x/\Delta t$	τ_0	U_{max}	$Error[\%]$
Δt	40	4	0.567	1.753	-
		8	0.520	1.437	18.01
		16	0.506	1.342	6.66
		32	0.502	1.319	1.68
		64*	0.500	-	-

*Unable to perform simulation due numerical instability

Attention was given while performing the spatial mesh sensitivity test for Power-law fluid flow. For this type of fluid the relationship between Δx and Δt is no longer linear as observed for Newtonian fluids, as discussed in section 5.9. That is, in order to keep τ_0 constant when the number of nodes doubles, and consequently Δx decreases by half, Δt can not be simply decreased by half, instead, it must be determined for a given value of n using Eq. 5.53. Thus, for a given Δx and a given value of τ_0 it is possible to determine Δt and consequently the relation $\Delta x/\Delta t$. Tab. A.3 shows results for the spatial sensitivity mesh test. When N increases from 160 to 320 the difference observed for the maximum velocity measured in

the velocity profile at the channel outlet is of 0.216%, which is less then 1%. For this reason, simulations for Power-law fluid flow between plates were performed with 160 lattices nodes along y direction.

The initial value of τ for a different value of n is determined based on the temporal mesh sensitivity test initially performed for $n = 0.25$. For $n = 0.25$ a value of $\Delta x / \Delta t = 32$ implies that $\tau_0 = 0.502$, however when n changes to 1.0, for $\Delta x / \Delta t = 32$ implies that $\tau_0 = 0.875$. The values of τ_0 for different values of n are related on Tab. A.4. Note that although τ_0 increases with increasing n, Δt decreases and consequently the Mach number, Ma, also does.

Table A.3 – Spatial mesh sensitivity test for Power-law fluid flow between parallel plates.

test	N	$\Delta x / \Delta t$	τ_0	U_{max}	$Error[\%]$
	40	32		1.319	-
Δx	80	35.33	0.502	1.226	7.04
	160	39.00		1.203	1.91
	320	43.07		1.200	0.22

Table A.4 – τ_0 for different values of n for Power-law fluid flow between parallel plates.

n	N	τ_0	$\Delta x / \Delta t$	Δx	Δt	Ma
0.25	160	0.5020	39.00	0.00625	1.60×10^{-4}	0.0045
0.6	160	0.5214	57.97	0.00625	1.08×10^{-4}	0.0031
1.0	160	0.8750	128.00	0.00625	4.88×10^{-5}	0.0014
1.4	160	7.0602	812.75	0.00625	7.69×10^{-6}	0.0002

A.3   Flow past over a cylinder

The sensitivity mesh tests for steady Newtonian fluid flow past over a cylinder were performed for $Re = 40$. The kinetic viscosity used was $\nu = 0.1 \ m^2/s$ and the distance between the plates was 40 times the cylinder diameter $H = 40 \times d$, following the work of Dash (2014) and Kang (2010).

To begin with the temporal mesh sensitivity test, the number of lattice nodes across the cylinder diameter was fixed at $N_d = 10$ which implies in 400 lattices notes along the x and y coordinates. The parameter chosen to be evaluated during the mesh sensitivity tests was the drag coefficient experienced by the particle, C_D. The ratio $\Delta x / \Delta t$ was gradually increased.

Results for Mesh sensitivity tests for Newtonian fluid flow past over a cylinder problem are shown in A.5. Although the difference observed for C_D still large when τ changes from 0.6 to 0.575 (1.388% of difference), the program was unable to perform simulations for values of τ under 0.575. For this reason τ was kept at 0.575.

After that, the spatial mesh sensitivity test was performed. Tab. A.5 shows that when the number of lattices in both x and y coordinates goes from 800 to 1600, the difference observed on C_D is of 0.741, which is less than 1%. For this reason, for steady flow past over a cylinder N was fixed at 800 which implies in 20 nodes across the cylinder diameter ($N_d = 20$).

Table A.5 – Mesh sensitivity tests for Newtonian fluid flow past over a cylinder problem.

$test$	N	$\Delta x/\Delta t$	τ	C_D	$Error[\%]$
		200	0.617	1.726	
		300	0.600	1.706	1.18
Δt	400	400	0.575	1.682	1.39
		500*	0.560	-	
	400	400		1.682	
Δx	800	800	0.575	1.594	5.26
	1600	1600		1.582	0.74

*Unable to perform simulation due numerical instability

For unsteady flow past over a cylinder, $Re = 100$ the simulations showed to be much more sensitivity to τ variations and a proper temporal mesh sensitivity test could not be done following Meira (2016). For $Re = 100$ the program was unable to perform simulation with τ under 0.62 and for this reason τ was fixed at 0.62. Results for time evolution of C_D and C_L for two different meshes, one with $N = 800$ and the other one with $N = 1600$ are compared. Figure A.1 shows the comparison for C_D. As can be seen, results for C_D change considerably when N goes from 800 to 1600. The same happens with C_L which results are presented on Fig. A.2. The results for $N = 1600$ are approaching the literature results, as shown in 6.3.2 and since simulations containing a large number of lattices take a long time to run (about 1 day for $N = 800$ and 5 days for $N = 1600$), a more refined mesh was not applied to this study since the trend of the results with increasing N was already observed and also, results for $N = 1600$ are already considerably close to results reported in literature.

A.4 Settling particle in Power-law fluid

The mesh sensitivity test for particle settling in Power-law fluid was performed for the case in which the highest settling velocity was expected. In this way, $d = 1.25\ cm$, $\rho_r = 1.25$ and $n = 0.6$. The temporal mesh sensitivity test was performed considering the number of lattice nodes across the cylinder diameter as $N_d = 15$, which implies in 120 nodes along x direction, since $d/L = 8$. The ratio $\Delta x/\Delta t$ was increase until the difference observed in maximum sedimentation velocity reached by the particle (terminal settling velocity), calculated using Eq. A.1, was less than 1%. This happened when $\Delta x/\Delta t$ increased from 100 to 200 and
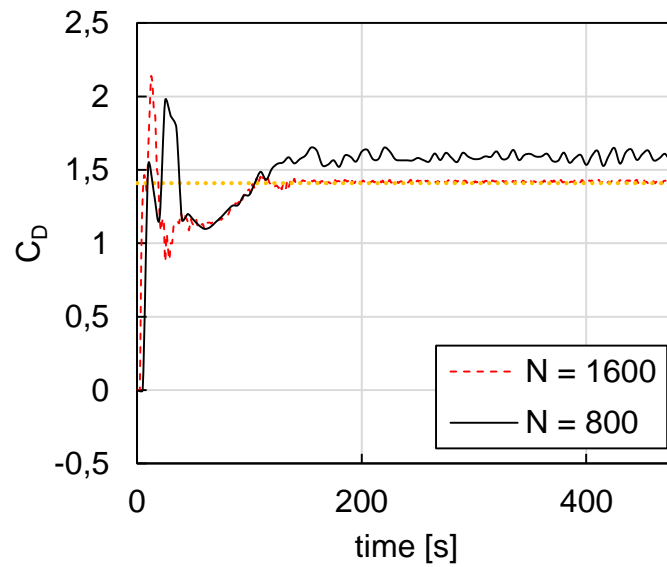
Figure A.1 – C_D time evolution for $N = 800$ and $N = 1600$.
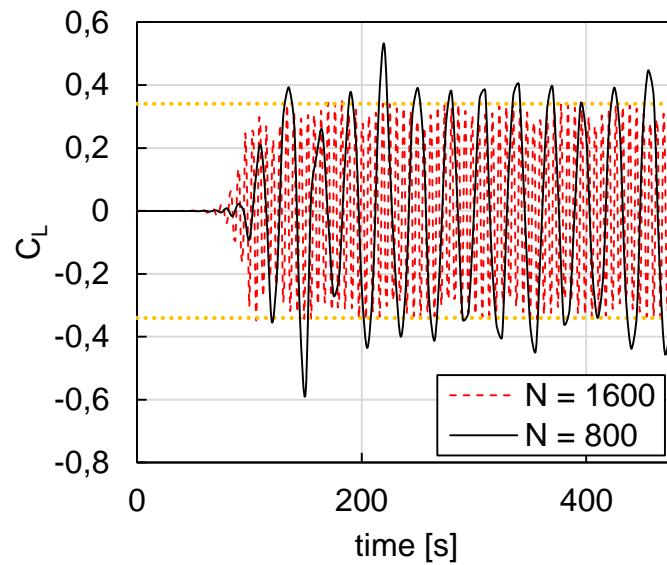
Figure A.2 – C_L time evolution for $N = 800$ and $N = 1600$.

consequently the compressible effects and temporal mesh dependency were considered negligible for $\tau_0 = 0.506$, as shown in Tab. A.6.

With τ_0 fixed, the number of nodes across the cylinder diameter was increased until dependency on spatial mesh becomes negligible, which occurred for $N_d = 25$, as shown in Tab. A.6.

The initial value of τ for a different value of n are shown in Tab. A.7 and were determined as described in section A.2.

Table A.6 – Mesh sensitivity test for particle settling in Power-law fluid.

$test$	N_d	N	$\Delta x/\Delta t$	τ_0	V_{MAX}	$Error[\%]$
			25	0.539	-7.328	-
Δt	15	120	50	0.515	-8.143	11.12
			100	0.506	-8.362	2.69
			200	0.502	-8.434	0.85
	15	120	100		-8.434	-
Δx	20	160	113.12	0.506	-8.596	1.92
	25	200	124.47		-8.655	0.69

Table A.7 – Values of τ_0 for different values of n for particle settling in Power-law fluid.

n	τ_0	$\Delta x/\Delta t$	Δx	Δt
0.6	0.506	113.12	0.01250	1.11E-04
0.8	0.532	121.14	0.01250	3.83E-04
1.0	0.680	133.33	0.01250	9.38E-05
1.2	1.525	153.96	0.01250	8.12E-05
1.4	6.342	195.67	0.01250	6.39E-05

APPENDIX B – Translation from physical to lattice units

The parameters in lattice units were obtained from the physical parameters by applying scale factors that were written in terms of Δx and Δt. The scale factors used for each parameter are listed in Tab.B.1. Note that for kinematic viscosity the scale factor takes into account the power law index. This is done so the generalized Reynolds number is keep the same in both physical and lattice units.

Table B.1 – Translation from physical to lattice units and the scale factor used for each parameter.

Parameter	Symbol	Physical units	Scale factor	Transformation to Lattice units
Length	H	$[m]$	Δx	$H_l = \dfrac{H}{\Delta x}$
Velocity	$\mathbf{u}$	$[m/s]$	$\Delta x/\Delta t$	$\mathbf{u_l} = \mathbf{u}\dfrac{\Delta t}{\Delta x}$
Angular velocity	ω	$[rad/s]$	$1/\Delta t$	$\omega_l = \omega\Delta t$
Acceleration	$\mathbf{a}$	$[m^2/s]$	$\Delta x^2/\Delta t$	$\mathbf{a_l} = \mathbf{a}\dfrac{\Delta t^2}{\Delta x}$
Angular acceleration	α	$[rad/s^2]$	$1/\Delta t^2$	$\alpha_l = \alpha\Delta t$
Density	ρ	$[kg/m^3]$	$\Delta M/\Delta x^3$	$\rho_l = \rho\dfrac{\Delta x^3}{\Delta M}$
Kinematic viscosity	ν	$[m^2/s]$	$\Delta x^2/\Delta t^{2-n}$	$\nu_l = \nu\dfrac{\Delta t^{2-n}}{\Delta x^2}$